DOI:10.15774/PPKE.ITK.2022.002

TEMPERATURE-COUPLED RHYTHM GENERATION AND AVERSIVE CUE DISCRIMINATION IN THE MOUSE THALAMUS

A THESIS SUBMITTED FOR THE DEGREE OF DOCTOR OF PHILOSOPHY

KINGA KOCSIS

PhD ADVISORS:

ISTVÁN ULBERT, DSc
FERENC MÁTYÁS, PhD

PÁZMÁNY PÉTER CATHOLIC UNIVERSITY
FACULTY OF INFORMATION TECHNOLOGY AND BIONICS
ROSKA TAMÁS DOCTORAL SCHOOL OF SCIENCES AND TECHNOLOGY

BUDAPEST, 2021.

DOI:10.15774/PPKE.ITK.2022.002

DOI:10.15774/PPKE.ITK.2022.002

Acknowledgements

I am grateful to all those who have supported me with various forms of mentorship and opportunities in my graduate research. First and foremost, I thank to all my current and former scientific advisors, Prof. Dr. István Ulbert, Dr. Ferenc Mátyás and Dr. Péter Barthó for providing me space and tools in neuroscience and the possibility to study such a diverse and intriguing structure as the thalamus.

I greatly thank Dr. Ferenc Mátyás that he put trust in my capabilities, he let me be part of a broader academic network, and that he taught me much about surgeries and neuronal network anatomy. I would like to express my appreciation to Dr. Péter Barthó and Dr. Márton Csernai for helping me improve my skills in electrophysiology and coding. I also thank further senior researchers, Dr. Boglárka Barsy, Dr. Sándor Borbély, PhD students Aletta Magyar, Ákos Babiczky and Veronika Balogh as well as lab assistants Anna Fehér, Eszter Együd, Judit Berczik, Katalin Varga, Lilla Truka, Réka Erdős and Tamás Herczeg, for helping me greatly in my work. I am thankful to my TDK students, Melinda Váncsodi, Félix Jártó and Roland Zsoldos who, besides their hard work and dedication, have independent and creative approaches to scientific work, which inspired me greatly and always cheered me up.

The teaching team and fellow students at the Marine Biological Laboratory in Woods Hole, MA, U.S., greatly broadened my perspectives in science and amplified the comparative and holistic view I intend to carry on in my future research. I met wonderful scientists such as Alena Lemazina who teaches me much about wild animal species, and Omar Koita who never ceases to amaze me with his careful thinking.

Besides lab work, I was drawn into many activities that substantially enriched my thinking and make me look at my subjects from multiple angles. I am grateful for the company of my creative friends and mentors: Bertalan Varga painter, Merse Varga percussionist and teacher, animation directors Nándor Bera, Borbála Eszter Tompa, documentary filmmakers Cecília Bandeira Tavares da Nóbrega and Ida Gedbjerg Sørensen, the community of the analog photography lab Lab4Art as well as of the improvised music association JazzaJ.

I am thankful to my former Biology classmates with whom I still share common interests in life sciences and exchange a lot of supportive information during this global crisis.

I am greatly indebted to my family, especially to my dear Mother, for always putting learning first, and for supporting me strongly in all of my endeavors.

Finally yet importantly, I am grateful to the animals whose lives were sacrificed for my research.

DOI:10.15774/PPKE.ITK.2022.002

TABLE OF CONTENTS

Preface 6

Abstract 7

Kivonat 8

Abbreviations 9

PART 1 Study of temperature-coupled dynamics of sleep spindles 10

1.1. Background and motivation of the study 10

1.1.1. Temperature dependence of neural rhythms 10

1.1.2. State dependence of brain temperature 12

1.2. Materials and Methods 14

1.2.1. **Ethical considerations** 14

1.2.2. **Acute *in vivo* electrophysiological and temperature recordings** 14

1.2.2.1. A technical note on urethane anesthesia 14

1.2.2.2. Neurophysiological recordings 15

1.2.2.3. Accuracy of brain temperature measurement 16

1.2.2.4. Local heating of brain tissue 16

1.2.3. **Histology** 17

1.2.4. **Data analysis** 17

1.2.4.1. Electrophysiological data processing 17

1.2.4.2. Temperature data processing 18

1.2.4.3. Statistical Analysis 18

1.3. Results 20

1.3.1. **Question Ia: How do alterations in core temperature affect sleep spindles?** 20

1.3.2. **Question Ib: How is the microarchitecture of brain temperature variations related to sleep spindles?** 25

1.4. Discussion 27

1.4.1. **Thesis Ia** 27

1.4.2. **Thesis Ib** 29

1.5. Relevant publications of the author 31

1.6. Outlook: potential for the study 32

DOI:10.15774/PPKE.ITK.2022.002

PART 2 Study of aversive cue discrimination in the thalamus 33

2.1. Background and motivation of the study 33

2.1.1. The direct thalamo-amygdala pathway 33

2.1.2. The 'non-canonical' collothalamic lateral thalamus 36

2.2. Materials and Methods 38

2.2.1. **Experimental subjects and ethical considerations** 38

2.2.2. **Stereotaxic surgeries** 38

2.2.2.1. General procedure 38

2.2.2.2. Injection of adeno-associated viral (AAV) vectors 39

2.2.2.3. Implantation of tetrodes and optic fibers 39

2.2.3. **Electrophysiology** 40

2.2.3.1. Acute *in vivo* electrophysiological recordings 40

2.2.3.2. Chronic *in vivo* electrophysiology in freely moving mice during threat learning 42

2.2.4. **Behavioral paradigms** 42

2.2.5. **Neural data processing** 43

2.2.6. **Immunohistochemistry** 46

2.2.6.1. Fluorescent microscopy 46

2.2.6.2. Electron microscopy 46

2.2.7. **Statistical analysis** 47

2.3. Results 48

2.3.1. **Question IIa: Do CR+ lateral thalamic neurons encode and discriminate the sensory cues necessary for associative aversive cue learning?** 49

2.3.2. **Question IIb: Can sensory activations in the amygdala related to aversive auditory learning be directly derived from CR+ lateral thalamic neurons?** 60

2.3.3. **Question IIc: What are the possible upstream sources of multimodal cue processing along the direct thalamo-amygdala route?** 64

2.4. Discussion 71

2.4.1. **Thesis IIa** 71

2.4.2. **Thesis IIb** 72

2.4.3. **Thesis IIc** 73

2.4.4. A note on the direct and indirect CR+ thalamo-amygdala routes 74

2.5. Relevant publications of the author 76

2.6. Outlook: future directions and potential for the study 78

2.6.1. CR+LT effect on intra-amygdala rhythmic activity 78

2.6.2. Interaction of CR+LT aversive cue processing with hormonal activity 78

2.6.3. CR+LT role in the subcortical processing of conspecific vocalizations 79

References 80

Tables 88

DOI:10.15774/PPKE.ITK.2022.002

Preface

The thalamus[1], principally composed of the glutamatergic thalamocortical (TC) projection neuron type, is a paired, subcortical, diencephalic brain structure in vertebrates. The hallmark of its structural and functional organization is the multitude of nuclei.

One classification principal for mammalian thalamic nuclei was developed by (Sherman & Guillery, 1998), and it is based on the origin of the principal excitatory driver input that determines receptive field properties. First-order thalamic nuclei are connected to peripheral sensory receptors by their driving innervation, such as the lemniscal inputs in the ventral posteromedial (**VPM**) and the medial geniculate (MGN) thalamic nuclei. In contrast, higher-order regions (e.g., posterior thalamic nuclear group, pulvinar) are principally driven by the cortex. Further inputs that alter the gain of thalamic sensory processing are considered modulators.

Another functional compartmentalization, the ‘core’ and ‘matrix’ duality, was introduced by (Jones, 1998). It largely corresponds to the distinction of first- and higher-order nuclei, respectively, but it rather highlights their different thalamocortical projections and calcium-binding protein immunoreactivity. Typical core areas are parvalbumin-positive (in many primates), and mainly target layer IV in a constrained cortical area and in a topographic order, as they keep high fidelity and precision in sensory relay. Matrix cells express calbindin and have diffuse cortical projections in layer I; their innervation lacks any topography. Matrix neurons can engage though many cortical and thalamic areas through thalamocortical backprojections, thus, contribute to sensory binding and the establishment of a coherent percept.

Capturing thalamic diversity in an updated framework, (Clascá *et al.*, 2012) divided nuclei into the following categories: core, matrix-focal, matrix-multiareal, and intralaminar, considering subcortical thalamic projections as well. Importantly, the multiareal and intralaminar type, such as neurons in the posterior intralaminar thalamic nucleus (**PIL**) send collaterals to the striatum and the amygdala.

My studies hereby focused on a primary thalamic mechanism, sleep oscillation generation in a core type thalamic nucleus, the VPM, and on a non-primary sensory function in the matrix-multiareal/intralaminar amygdala-projecting lateral thalamus, including the PIL.

[1] It refers to the dorsal thalamus throughout my studies.

DOI:10.15774/PPKE.ITK.2022.002

My doctoral research is dedicated to add to the growing body of research that features the thalamus beyond a passive messenger role. It is highlighted as a dynamic gateway where various afferents and physiological factors can alter adaptive thalamic communication with telencephalic structures, thus, ultimately learning, and behavioral plasticity itself.

Abstract

First, I focused on a hallmark synchronous neuronal activity in sleep, thalamocortical sleep spindle oscillations. I studied how sleep spindles are interrelated with changing body and local brain temperatures. To tackle this question, I employed a novel thermoelectrode designed for simultaneous temperature measurement and neural activity recording. I found that spindle frequency is positively, duration is negatively correlated with body and consequently with brain temperature. Local heating of the thalamus replicates the temperature dependence of spindle parameters in the heated area only, suggesting a local biophysical mechanism. Furthermore, on a shorter and smaller scale, I found joint spontaneous microfluctuations in brain temperature and spindle activity, which correspond to a REM-like and to an infraslow periodicity. This study highlights that brain temperature is massively intertwined with thalamic spindle rhythm generation on multiple time scales.

The scope of my second study was an evolutionarily conserved route between the thalamus and the amygdala. I showed that lateral thalamic (LT) cells expressing the calcium-binding protein calretinin (CR) are able to form and transfer associated aversive signals to a key subcortical area which develops and orchestrates learned threat induced behavior, the lateral region of the amygdala. As aversive experience-dependent cue integration drives response modulations at the level of single CR+ thalamic neuronal activity, these cells can also directly influence threat memory processes. This ability is supported by a unique non-primary midbrain innervation from the colliculi onto CR+LT neurons. In the amygdala, the robustness of aversive cue processing is further ensured by the CR+ thalamic innervation of interneurons, which potentially configure network activity. Altogether, the results of my second study confirm that in rapid threat processing, the amygdala relies on a multimodal preprocessing instead of integrating primary sensory information.

DOI:10.15774/PPKE.ITK.2022.002

Kivonat

Első tanulmányomban egy alvást fémjelző szinkron idegsejt-aktivitásra, a talamokortikális alvási orsó oszcillációra összpontosítottam. Vizsgáltam, hogy az alvási orsók hogyan kapcsolódnak a test és az agy hőmérsékletének változásaihoz. Ennek a kérdésnek a megválaszolásához egy új, ún. termoelektródát alkalmaztam, amely egyidejűleg szolgál hőmérsékletmérésre és az idegsejt-aktivitás rögzítésére. Megállapítottam, hogy az orsófrekvencia pozitívan, míg az orsóhossz negatívan korrelál a test és következésképp az agy hőmérsékletével. A talamusz helyi melegítése csak a fűtött területen reprodukálja az orsó paramétereinek hőmérsékletfüggését, ami lokális biofizikai mechanizmusra utal. Továbbá, rövidebb idejű és kisebb léptékben, az agyhőmérséklet és az orsóaktivitás kapcsolt és spontán mikrofluktuációit figyeltem meg, amelyek REM-szerű és infralassú periodicitásnak felelnek meg. Ez a tanulmány rávilágít arra, hogy az agyi hőmérséklet több időskálán függ össze szorosan a talamikus orsóritmus generálásával.

Másik kutatásom tárgya a talamusz és az amigdala közötti evolúciósan konzervált útvonal volt. Kimutattam, hogy a kalretinin (CR) kalciumkötő fehérjét kifejező oldalsó (laterális) talamikus idegsejtek (CR+LT) képesek társított averzív jeleket képezni és továbbítani a tanult elkerülő viselkedés létrejöttében és szerveződésében kulcsfontosságú agykéreg alatti területre, az amigdala laterális régiójába. Miként az averzív tapasztalattól függő jelintegráció válaszmodulációt vált ki egyedi CR+ talamikus neuronok szintjén, ezek a sejtek közvetlenül befolyásolhatják a félelmi memóriafolyamatokat is. Ezt a sajátságot az ikertestekből a CR+LT idegsejtekre érkező egyedülálló, nem elsődleges középagyi beidegzés is alátámasztja. Az amigdalában az averzív jelek feldolgozásának robusztusságát biztosítja továbbá a CR+ talamikus beidegzése az interneuronoknak, melyek potenciálisan konfigurálják a hálózati aktivitást. Összességében a második tanulmányom eredményei igazolják, hogy a veszélyre utaló jelek gyors feldolgozása során az amigdala multimodális előfeldolgozásra támaszkodik elsődleges szenzoros információk integrálása helyett.

DOI:10.15774/PPKE.ITK.2022.002

Abbreviations

AAV	adeno-associated virus
ACC	auto-correlogram
AMY	amygdala
AP	anteroposterior
AStr	amygdalostriatal transition area
Au1	primary auditory cortex
AuV	secondary auditory cortex, ventral part
CC	cross-correlogram
CeA	central amygdala
ChAT	choline acetyltransferase
ChR2	channelrhosopsin-2
CR	calretinin
CS	conditioned stimulus
En	entorhinal cortex
eYFP	enhanced Yellow Fluorescent Protein
FS	foot shock
HW	half-width
IC: DCIC/ECIC/CIC	inferior colliculus: dorsal cortex, external cortex and central nucleus
IN	interneuron
ITC	intercalated nuclei of the amygdala
LA	lateral amygdala
LFP	local field potential
LT	lateral thalamus
MGM	medial geniculate nucleus, medial part
MGN	medial geniculate nucleus
ML	mediolateral
MUA	multi-unit activity
NpHR	halorhodopsin
ON	onset response
OFF	offset response
PAG	periaqueductal gray
PC	principal component
PIL	posterior intralaminar thalamic nucleus
Pir	piriform cortex
PN	principal neuron
Pr5	principal sensory trigeminal nucleus
PSTH	peristimulus time histogram
RT	room temperature
SC: sSC/iSC/dSC	superior colliculus: superficial, intermediate and deep layers
SIC	supra-intercalated cluster of neurons (Barsy & Kocsis *et al.*, 2020)
SG	suprageniculate thalamic nucleus
SW	spike-width
TeA	temporal association cortex
TC	thalamocortical relay neuron
US	unconditioned stimulus
vGAT	vesicular GABA (gamma-aminobutyric acid) transporter
vGluT	vesicular glutamate transporter
WF	waveform

DOI:10.15774/PPKE.ITK.2022.002

PART 1 Study of temperature-coupled dynamics of sleep spindles

1.1. Background and motivation of the study

Sleep is essential for our everyday functioning including adaptive memory consolidation. Several biophysical factors influence sleep, temperature being amongst the most important ones. Whereas sleep propensity and quality are highly dependent on thermal conditions, and sleep regulation is tightly coupled to thermoregulation (Krauchi & Deboer, 2010), the temperature dependence of the underlying neuronal network activity of sleep is sporadically addressed in neurophysiology.

1.1.1. Temperature dependence of neural rhythms

It is well-known that temperature affects the rate of biological processes (van't Hoff, 1884; Arrhenius, 1889) with a temperature coefficient (*Q10*) between 2 and 3, which equals the factor by which the rate of the process changes as temperature increases by 10°C (James, 1953; Demirhan *et al.*, 2010). Despite constant redistribution of cerebral heat, neuronal activity is a function of temperature. Physiological and pathological temperature alterations of the brain can be derived from the changes of local metabolism, cerebral blood perfusion, and blood temperature (Hayward & Baker, 1969). Brain cells show a *Q10* of 2.3 (Michenfelder & Milde, 1991) or even higher in the physiological temperature range.

Temperature dependence of electrophysiological properties in the neuron is well defined. Passive membrane properties, resting potential, action potential generation, ionic transport, conduction velocity, synaptic transmission and neurotransmitter reuptake are all dependent on thermal conditions (B Katz, 1965; Brooks, 1983; Thompson *et al.*, 1985; Volgushev *et al.*, 2000; Tryba & Ramirez, 2004; Lee *et al.*, 2005). Cerebral metabolic rate and the oxygen affinity of hemoglobin are also affected by temperature change (Guyton & Hall, 2005). The sum of these effects may dramatically change neuronal network activity.

Temperature dependence of neural oscillations is also described by the *Q10* value, which is 2.3-2.7 (Deboer & Tobler, 1995). It is worthy to note that several poikilothermic animals, such as certain crustaceans and mollusks, employ compensatory mechanisms to make their neural oscillators robust to temperature changes (Partridge & Connor, 1978; Tang *et al.*, 2012). Whether a similar mechanism exists in the mammalian nervous system remains to be elucidated. Nevertheless, climate perturbations with rising nighttime temperatures can raise a serious challenge for many species including humans to maintain robustness in neural rhythm generation and sleep (Obradovich *et al.*, 2017).

DOI:10.15774/PPKE.ITK.2022.002

The tight relationship between core body temperature and sleep stages was verified by directly manipulating either of them. Changes in body temperature have the potential to entrain brain state fluctuations (Whitten *et al.*, 2009), and even baseline temperatures influence particular brain oscillations. A brain temperature change of 1 °C is sufficient to shift EEG frequencies above 10 Hz by 1 Hz (Deboer & Tobler, 1995). Lowering body temperature results in a decreasing EEG amplitude (Massopust *et al.*, 1965; Michenfelder & Milde, 1991) and a shift towards lower frequencies (Deboer & Tobler, 1995).

Temperature-dependent changes in brain oscillations that reflect the activity of synchronized neural populations, point towards deeper consequences of thermal change in network function.

The general consensus is that thalamocortical oscillations in sleep play a major role in learning and memory consolidation. Several studies reported increases in slow wave and spindle activity during sleep after learning tasks (Feld & Born, 2017). Also, transcranial direct-current stimulation (Marshall, 2004), or phase-locked auditory stimulation (Ngo *et al.*, 2013) of slow waves during sleep can enhance the consolidation of declarative memories.

Amongst thalamocortical oscillations, sleep spindles (7-15 Hz frequency, 1-3 s length) have been the subject of many studies on sleep quality, memory encoding and mental health. These transient oscillations are generated during the early stages of sleep, by the mutual rhythmic interaction of excitatory TC and inhibitory thalamic reticular (Rt) neurons, that in turn entrains cortical network activity (**Figure 1.1.1./a-b**). This 'ping-pong' mechanism stems from the long inhibitory postsynaptic potential (IPSP) exerted by bursting Rt activity on TC neurons (Steriade *et al.*, 1985), which activates low-voltage-gated calcium(Ca^{2+})-channels (I_T) and leads to a rebound TC burst. This evokes the next Rt burst cycle (Krosigk *et al.*, 1993) (**Figure 1.1.1./c**).

As learning involves both long-term potentiation (LTP) and long-term depression (LTD) of synapses (Siegelbaum & Kandel, 1991), packets of synchronized neural activity, such as cycles of sleep spindles make this oscillation an ideal candidate for building new memories. Moreover, it has been suggested by (Crunelli *et al.*, 2018) that the underlying low-threshold burst firing in TC and Rt neurons can potentially involve a rhythmic and global somatodendritic Ca^{2+} transient and signaling which in turn leads to non-Hebbian plasticity mechanisms in thalamic networks.

In fact, spindles play critical role in learning (Fogel *et al.*, 2007; Morin *et al.*, 2008), and sigma power (10-15 Hz) – corresponding to the spindle frequency range – marks offline states for memory processing in an infraslow (0.02 Hz) periodicity (Lecci *et al.*, 2017). Spindle duration and frequency are affected in a variety of pathological states, including schizophrenia (Manoach *et al.*, 2016), spindle duration and frequency correlate with intelligence (Bódizs *et al.*, 2014).

DOI:10.15774/PPKE.ITK.2022.002

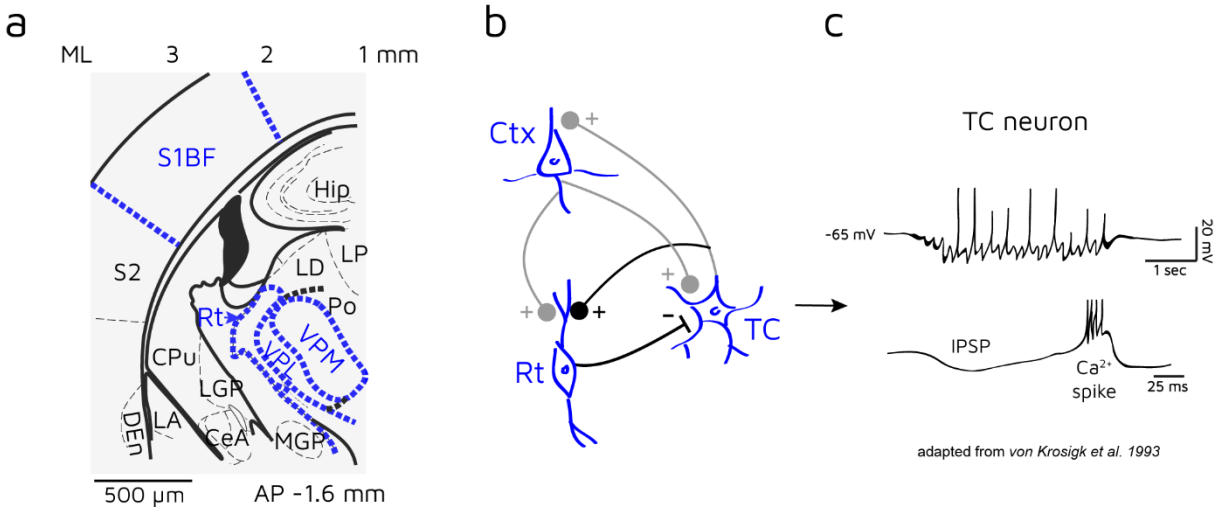

Figure 1.1.1. Neuronal network basis of sleep spindle oscillations.

a/ Elements of the mouse somatosensory thalamocortical system studied in this research. Excerpt adapted from (Paxinos & Franklin, 2003). S1BF: primary somatosensory cortex, barrel field; Rt: reticular thalamic nucleus (t.n.); VPM: ventral posteromedial t.n.; VPL: ventral posterolateral t.n. **b/** Scheme for connectivity in the thalamocortical network; Ctx: cortical neuron; TC: thalamocortical relay neuron; Rt: reticular thalamic nucleus cell. + sign indicates excitatory, - sign represents inhibitory synapses. Based on (Steriade *et al.*, 1993). **c/** Rhythmic intracellular activity of a TC neuron (upper trace) resulting from mutual TC-Rt interaction in spindle generation. A cycle of the spindle wave (bottom trace) showing the Rt-evoked IPSP and the following low-voltage-gated calcium-dependent TC burst. Traces are adapted from (Krosigk *et al.*, 1993).

At the same time, these transient oscillations are very susceptible to thermal changes of the mammalian body. It has been shown that the frequency of sleep spindle oscillations strongly co-varies with physiological body temperature changes reoccurring across the menstrual cycle (Driver *et al.*, 1996). Spindle activity also shows a circadian modulation with a peak density at habitual sleep onset, time-locked to the maximal decrease in core temperature (Dijk & Czeisler, 1995). Thus, it is essential to further study how spindle dynamics are affected by body and brain temperature variations.

1.1.2. State dependence of brain temperature

There are also sleep-related changes in body and brain temperature independent of the circadian rhythm. Studies in mammalian species have shown that there are multiple changes in body and brain temperature during a single sleep session. NREM (non-rapid eye movement) sleep is associated with decreased brain and body temperature, while during REM sleep, brain temperature increases (Kawamura & Sawyer, 1965; Baker & Hayward, 1967; Satoh, 1968; Kovalzon, 1973; Alföldi *et al.*, 1990; Lyamin *et al.*, 2018). Although the body's temperature regulation declines during REM (Parmeggiani, 1977), this paradoxical increase in brain temperature has been described in rabbit (Kawamura & Sawyer, 1965; Baker & Hayward,

1967), cat (Satoh, 1968), rat (Kovalzon, 1973; Obál *et al.*, 1985; Alföldi *et al.*, 1990), and suggested even in fur seal (Lyamin *et al.*, 2018). However, some monkey studies reported just the opposite phenomenon (Reite & Pegram, 1968; Hayward & Baker, 1969), involving peripheral vasodilatation instead of vasoconstriction. It is questionable whether this effect in REM is protective for brain function, or only reflects the increased metabolic activity due to increased unit firing.

Besides the above-mentioned short-term changes, core body temperature can vary across individuals (Sund-Levander *et al.*, 2002), with changes in ambient temperature (Alföldi *et al.*, 1990), in pathological metabolic conditions, such as hypo- or hyperthyroidism (Fregly *et al.*, 1961), through the oestrous cycle (Driver *et al.*, 1996), or as a result of medical or recreational drug use (Kiyatkin, 2010). Though brain temperature is recognized as a strictly regulated homeostatic parameter, it can change as much as 3 °C across different arousal states and during sensory stimulation as shown across many avian and mammalian species (Delgado & Hanai, 1966; McElligott & Melzack, 1967; Kovalzon, 1973; Kiyatkin *et al.*, 2002; Mitchell *et al.*, 2006; Trübel *et al.*, 2006), as well as in clinical human studies (Mellergård, 1995; Rossi, 2001).

Given the large natural variability in brain temperature across individuals and conditions, it is extremely important to shed light on its relationship with neural oscillations. From a clinical point of view, medications and external thermal conditions both alter brain temperature, which should therefore be considered as a factor in medical procedures. On the other hand, brain temperature should be taken into consideration in *in vivo* neurophysiological experiments, as well as for *in silico* network models, in order to mimic better natural state changes.

In this part of my studies, I sought to examine the relationship between sleep spindle oscillations and core temperature combining broadband extracellular electrophysiological as well as core body and brain temperature recordings in urethane-anesthetized mice.

- I investigated the changes in spindle oscillations while manipulating and measuring core as well as selectively brain temperature (**Aim Ia**);
- I studied how this rhythmic neuronal activity relates to the microarchitecture of baseline brain temperature variations (**Aim Ib**).

DOI:10.15774/PPKE.ITK.2022.002

1.2. Materials and Methods

1.2.1. **Ethical considerations**

Experiments were carried out in accordance with the Hungarian *Act XXVIII of 1998 on the protection and sparing of animals* and with the *Directive 2010/63/EU of the European Parliament and of the Council of 22 September 2010 on the protection of animals used for scientific purposes.* All experimental procedures and protocols were approved by the Regional and Institutional Committee of the Research Centre for Natural Sciences (license number PEI/001/2290-11/2015 for *in vivo* experiments). I performed experiments with the authorization of the Semmelweis University's Institutional Animal Care and Use Committee (Certificate No. 89./2014).

Significant efforts were made to minimize the number of animals used, and the stress level of the subject animals. Animals were group-housed in a humidity- and temperature-controlled (22 ± 2°C) facility. They were kept under a 12:12 h light-dark cycle (light phase on at 7:00 a.m.). Standard food-pellets and tap water were available for them *ad libitum*.

1.2.2. **Acute *in vivo* electrophysiological and temperature recordings**

Experiments were performed on 13 male C57BL/6 mice (Toxicoop) weighing between 18 and 30 g at the time of their surgery. The animals were sedated with isoflurane (Isofluran CP, CP-Pharma) and anesthetized with urethane (1.2 g/kg, IP; Sigma-Aldrich), then placed into a stereotaxic instrument (RWD Life Science). Rectal temperature was measured with a TH-5 Thermalert Monitoring Thermometer (Physitemp) and kept stable at 37° C during surgery. Craniotomies were made over the target brain areas, and electrodes were lowered into the brain at a speed below 0.2 mm/s. After electrode insertion, we waited for 30 minutes before starting recording.

1.2.2.1. A technical note on urethane anesthesia

Urethane anesthesia was chosen to abolish homeostatic thermoregulation, so the experimental animal's temperature could be deliberately manipulated. Urethane anesthesia is considered a good model for natural sleep (Clement *et al.*, 2008; Pagliardini *et al.*, 2013), as it reproduces most sleep rhythms with minor deviation. Accordingly, sleep spindles under urethane anesthesia are also very similar to those in natural sleep, except for their more limited spatial synchrony (Barthó *et al.*, 2014).

Whereas awake animals and large mammalian species have a positive (Hamilton, 1963; Hayward & Baker, 1969; Mitchell *et al.*, 2006; Hebert *et al.*, 2008), small animals have a negative brain-body temperature gradient under anesthesia (Serota & Gerard, 1938; McElligott & Melzack, 1967; LaManna *et al.*, 1989), most likely due to a higher brain-surface ratio, the cooling through evaporation at the craniotomy site, and the impaired thermoregulation caused by the anesthetic. It was shown (Csernai & Borbély & Kocsis *et al.*, 2019) that the mouse brain can generate spindle, theta, and slow oscillations at 2-3 °C below physiological brain temperature, therefore, urethane anesthesia was accepted as a suitable tool for the experiments.

When assessing the potential effect of body temperature on the depth of anesthesia, we considered that a potential spontaneous decrease of urethane effect over time could induce spurious correlations with temperature in extended heating or cooling sessions. To this end, recordings were divided into heating and cooling sessions, and analyzed separately within animal subjects. Partial correlations were calculated for three cortical local field potential (LFP) frequency bands (delta 1–4 Hz, beta 20–30 Hz and gamma 30–100 Hz) with temperature controlled for the effect of time using the MATLAB *partialcorr* function.

1.2.2.2. Neurophysiological recordings

Before each acute experiment, silicon probes were dipped in orange fluorescent DiI solution for further verification of the recording sites. NeuroNexus silicon probes were used to record broadband activity. Linear 16-channel (L16) silicon probes were inserted into the left primary somatosensory cortex (Bregma (Br.) AP 0, ML +3.5, in 18º at 1600 µm depth), and in the left ventral posteromedial nucleus (VPM) of the thalamus (Br. AP -1.6, ML +2.3, in 18º at 3700 µm depth). The custom-designed thermoelectrode (Fekete *et al.*, 2017), featuring four electrophysiological recording sites and a platinum temperature sensor, was also inserted into the left VPM (Br. AP -1.6, ML +1.6, in 0º at 3600 µm depth). In some experiments, the L16 probe was inserted into the right primary somatosensory cortex or into the right VPM. In this case, there was no recording from the left cortical area. Coordinates were based on the stereotaxic atlas of (Paxinos & Franklin, 2003).

An additional screw electrode was implanted over the cerebellum and served as a reference. Using unipolar V_1 electrocardiogram (ECG) lead, heart rate and electrocardiogram were simultaneously recorded with the LFP. Recordings were made with 16-channel Intan RHD2132 amplifiers, connected to an RHD2000 evaluation board (Intan Technologies Llc.). Brain temperature was measured upon calibration and measurement of the resistance of the platinum filament in the thermoelectrode (Fekete et al., 2017) with a Keithley 6221 precision

current generator and a Keithley 2000MM multimeter (Keithley Instruments Inc). All signals were sampled at 20 kHz, except for brain temperature, which was sampled at 5 Hz. Rectal and brain temperature signals were simultaneously recorded with all other signals by using the analog inputs of the Intan RHD2000 system.

1.2.2.3. Accuracy of brain temperature measurement

The accuracy of absolute temperature measurement in thermoprobe recordings was below 0.14 °C (Fekete *et al.*, 2017). The sensitivity of the device to relative changes in temperature, also required to measure LFP microfluctuations, however, is orders of magnitude higher. At 33 °C, the resistance (R_0) and temperature coefficient (α) of the integrated platinum temperature filament is 335.81±18.22 Ω and 1721±99 ppm/K, respectively, so approximately 0.002 Ω change in resistance corresponds to a temperature change of 0.01 °C. The measurement resolution of the Keithley 2000 MM unit is 0.001 Ω in a range of 1 kΩ. Based on these details, it is accurate to evaluate as small temperature variations as 0.01 °C.

In the case of the Semitec thermistor, there is a non-linear relationship between resistance and temperature, which is governed by the thermistor equation:

$$T = \frac{B}{ln\left(\frac{R_{thermistor}}{R_0 \times e^{\frac{-B}{T_0}}}\right)}$$

where *B* material constant of the thermistor is 3454, and its rated zero-power resistance (R_0) is 14015 Ω at 37 °C. If the temperature changes from e.g., 37 °C to 38 °C, it corresponds to a decrease in resistance by approximately 500 Ω. To simplify this case, considering the relationship linear in this range, 0.01 K change induces 5 Ω decrease, which can be accurately and easily measured by the setup.

1.2.2.4. Local heating of brain tissue

The platinum filament in the thermoelectrode can be used to heat up adjacent brain tissue by increasing the current in the 4-wire resistance measurement setup (see technical and histological details in (Fekete *et al.*, 2017)). We employed cycles of 2 minutes of measurement current (1 mA) and 2 minutes of heating current (4-8 mA). In each cycle, an exponential was fitted on the measured temperature values starting from 400 ms after the offset of the heating current. The temperature during heating was estimated by the intersection of the exponential and the offset time of the heating pulse. (**Figure 1.3.1.3./c**).

Distance dependence of heating was calculated by locally heating the brain tissue with the thermoprobe at 4, 6, and 8 mA currents for 50 s, while measuring the elicited temperature change with a Semitec thermistor inserted at 0.5, 1, and 3 mm distances, consecutively. Only the temperature value by the end of the heating was considered (**Figure 1.3.1.3./b.**).

1.2.3. **Histology**

Following recordings, mice were transcardially perfused under deep urethane anesthesia with 0.9 % saline, followed by fixative containing 4 % paraformaldehyde and 0.1 M phosphate buffer (PB). After perfusion, brains were sliced to 50 µm thick coronal sections with a vibratome (Leica). After multiple PB washes, sections were mounted temporarily in PB and imaged for the reconstruction of DiI-stained electrode tracks using epifluorescent microscopy (Leica). After further PB washes and freeze-thawing above liquid nitrogen in 0.1 M PB containing 30% sucrose, slices were also counterstained for glial fibrillary acidic protein (GFAP). This served to visualize the lesion made by the thermoprobe insertion or any potential necrosis caused by tissue heating (see **Table 2.** for a detailed protocol). 3,3'-diaminobenzidine tetrahydrochloride (DAB) was used as a chromogen in the immunoperoxidase reaction. After washing in Tris buffer and PB, sections were mounted, dehydrated in xylene for 2x10 minutes for light microscopy, and coverslipped with DePex (Serva Electrophoresis GmbH).

We found no necrosis in any of the animals (see also (Fekete *et al.*, 2017)).

1.2.4. **Data analysis**

1.2.4.1. Electrophysiological data processing

Raw local field potential (LFP) data were band-pass filtered between 0.4-7 kHz, and multi-unit activity (MUA) was detected with an absolute threshold. Units were combined from multiple channels, downsampled to 1 kHz, and smoothed with a 10 ms moving average filter. Sigma power was determined by filtering the preprocessed MUA between 6-18 Hz. In the case of the analysis of infraslow oscillations, sigma power from selected recording sites was used. Heart rate was smoothed with a 10 s moving average window. Sigma band and MUA were normalized to their means.

Spindles were detected semi-automatically from the multi-unit activity. Downsampled (1 kHz) MUA was smoothed with an 11 ms long rectangular filter, and further filtered between 8 and 20 Hz. The automatic detection threshold was set to 1 SD, with a minimum spindle length of 300 ms. Simple thresholding sometimes spuriously detects desynchronized activity, and these events were manually removed. Also, since this analysis is sensitive to missed cycles,

spindles with a break in rhythmicity (gap >150 ms) were omitted. The frequency of spindles was calculated from the average interval determined between automatically detected cycle peaks (**Figure 1.3.1.1/b**). Temperature value measured at the start of the respective spindle was considered for analysis. Spindle prevalence was calculated in 2-minute time bins.

To give the common measure for the temperature dependence of spindle frequency, Q_{10} was calculated based on the temperature coefficient equation:

$$Q_{10} = \left(\frac{R2}{R1}\right)^{10℃/(T_2 - T_1)}$$

where

- Q_{10} is the factor by which spindle frequency increases when the temperature is raised by 10 °C
- R_2 is spindle frequency (in Hz) at temperature T_2, where $T_2 > T_1$.
- R_1 is spindle frequency (in Hz) at temperature T_1.
- T_2 is the temperature (in °C) at which spindle rate R_2 is measured, where $T_2 > T_1$.
- T_1 is the temperature (in °C) at which spindle rate R_1 is measured.

1.2.4.2. Temperature data processing

Rectal temperature data were downsampled to 1 kHz and smoothed with a 100 ms window. In the case of brain temperature, all the samples that were synchronized to the other recorded signals were used. When analyzing infraslow oscillations, all respective signals were smoothed with a 10 s window and then downsampled to 10 Hz, while brain temperature was interpolated to 10 Hz. Large fluctuations were marked manually based on visual features of brain temperature increase motifs. Small fluctuation epochs were selected from the epochs between the large elevations. Small fluctuation cycle peaks and troughs were detected automatically (MATLAB *findpeaks* function), and the detected peaks were manually validated in each epoch.

1.2.4.3. Statistical Analysis

Correlations were calculated using the Pearson's coefficient (MATLAB *corrcoef* function). Pooled correlation coefficients were transformed to normal distribution by Fisher z-transformation prior to testing.

Spindle parameters during locally heated and control periods were compared with Student's two-sample *t*-tests instead of paired *t*-tests, since the number of spindles in the respective periods were different. In the case of pooled data (**Figure 1.3.1.4./b**), only those comparisons were included where the number of spindles in any heating/control period was above 10. Since

three comparisons were omitted based on this criterion, the Mann–Whitney–Wilcoxon test was used instead of the corresponding paired tests.

Otherwise, parametric statistical tests were used based on the normality of observed distributions, tested with Kolmogorov-Smirnov test at 0.05 significance level.

In all statistical tests with no significant results, power of the tests was above 0.75 with the sample sizes used in the study, based on minimal effect size of 0.2 in case of correlation comparisons and 1 Hz for spindle frequency difference.

All analysis was done with custom-written MATLAB (MathWorks) codes created by Dr. Péter Barthó, Dr. Márton Csernai, Dr. Sándor Borbély (Research Centre for Natural Sciences (RCNS), Budapest, Hungary) and by myself.

DOI:10.15774/PPKE.ITK.2022.002

1.3. Results

1.3.1. **Question Ia:** How do alterations in core temperature affect sleep spindles?

The first aim was to investigate the temperature dependence of spindle oscillations with no or minimal interference from global thermoregulation. To this end, we employed urethane anesthesia, which is known to impair thermoregulatory processes (Malkinson *et al.*, 1988), yet it closely mimics natural sleep (Clement *et al.*, 2008). This way, core body temperature can be manipulated by external heating within quasi-physiological boundaries, enabling the examination of how temperature changes as large as 4-5 °C alter these sleep oscillations.

Local field (LFP) and multi-unit activity (MUA) were recorded from the thalamus and cortex of anesthetized mice (n=8), while the animals' core body temperature was varied between 34 and 39 °C. To simultaneously measure brain temperature and ongoing neural activity, we used the thermoelectrode developed in a collaboration with our lab (Fekete *et al.*, 2017). This probe has regular recording sites for unit activity, as well as a temperature sensitive meander, capable of measuring the temperature of the surrounding tissue with an absolute precision of <0.2 °C (relative precision <0.002 °C). The thermoelectrode was placed in the primary somatosensory thalamus (VPM/VPL), while 16-channel linear silicon probes were also placed in the contralateral cortex / thalamus (**Figure 1.3.1.1./a**).

Sleep spindles were detected form both thalamic and cortical MUA (**Figure 1.3.1.1./b-c**). Besides LFP, MUA and brain temperature, core temperature and electrocardiogram were simultaneously recorded; heart rate variation was calculated from the detected R-waves of the ECG signal (**Figure 1.3.1.1./c**).

After surgery and the implantation of the sensors, by controlling the heating pad placed under the mouse, I let the core temperature of the animal cool down to 34/35 °C. Next, in 30-minute segments, I increased the temperature of the heating pad such that core temperature increased by ~0.5 °C in each recording segment, until core temperature reached 39 °C. In half of the animals, the order of heating and cooling was interchanged. This assured the collection of a large number of spindles in a steady state temperature of different degrees, at the same time the exclusion of the effect of temperature dynamics and directionality. **Figure 1.3.1.1./d** shows a recording epoch of core body, brain temperature as well as the detected thalamic and cortical sleep spindles from warming and cooling protocols. Brain temperature closely follows changes in core temperature across all animals (**Figure 1.3.1.2./a**), brain temperature being lower by 2-3 °C, as expected in small animals under anesthesia (LaManna *et al.*, 1989).

DOI:10.15774/PPKE.ITK.2022.002

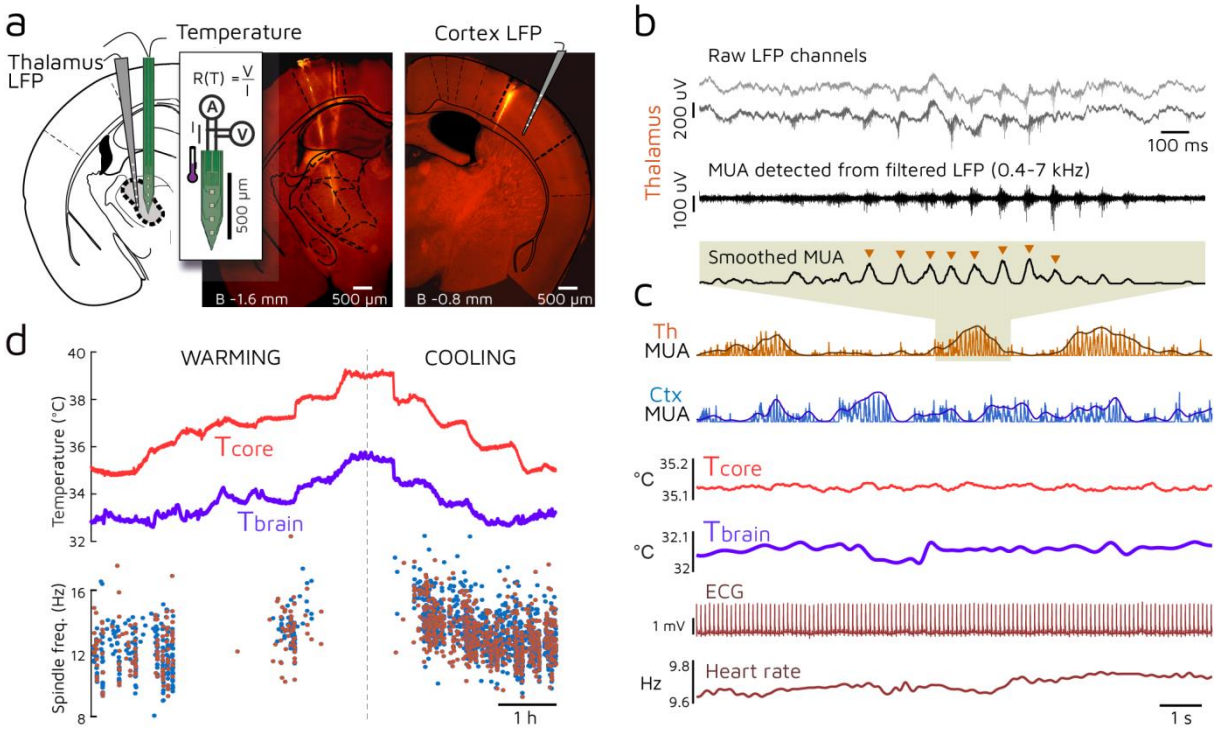

Figure 1.3.1.1. Recorded signals for characterizing the temperature dependence of thalamocortical sleep spindle oscillations.

a/ Recording of LFP, MUA and temperature from the VPM thalamic nucleus (n=8 mice) with a linear 16-channel probe, and with our custom-designed thermoelectrode (left DiI tracks). Temperature was measured by four-wire resistance measurement of the platinum filament in the thermoelectrode calibrated to 1mA current (inset). Control LFP recordings (right) with the linear 16-channel probe from the contralateral primary somatosensory cortex (shown) or VPM. **b/** Raw LFP channels (gray traces) were band-pass filtered (black trace), then, detected units were combined from multiple channels and smoothed with a moving average filter (smoothed MUA). The frequency of spindles was calculated from the interpeak interval (brown triangles) and averaged across cycles. **c/** A sample recording chunk showing from top to bottom: thalamic raw and smoothed MUA (shaded enlarged in **b**), cortical raw and smoothed MUA, core and brain temperature, electrocardiogram (ECG), and heart rate calculated from the ECG. **d/** Example of core body and brain temperature under warming and cooling protocols. Spindle frequency is modulated by both core and brain temperature both in the thalamus and cortex.

Published in (Csernai & Borbély & Kocsis et al., 2019) Figure 1./A-D.

Spindle frequency and duration were consistently and inversely modulated by both core and brain temperature in the majority of animals, both in the thalamus and cortex. This was confirmed by calculating the correlation between brain temperature and spindle frequency (**Figure 1.3.1.2./b** for the animal in **Figure 1.3.1.1./d**). The pooled data of correlation coefficients were taken from all animals (**Figure 1.3.1.2./d**) where the number of detected spindles exceeded 100 (thalamus: n=6, cortex: n=7 mice). Spindle frequency is significantly increased by brain temperature (mean R: 0.37±0.18 for thalamic, 0.34±0.3 for cortical spindles, respectively, p = 0.0038, and 0.009, *t*-test after Fisher z-transformation), while spindle duration is significantly reduced (mean R: -0.12±0.1, p = 0.0014 in the thalamus, R: -0.14±0.06, p = 0.0019 in the cortex). These values were still statistically significant after

DOI:10.15774/PPKE.ITK.2022.002

Bonferroni correction. On the other hand, the number of cycles of spindles and spindle prevalence showed no significant dependence on brain temperature.

The modulation of spindle frequency can be expressed as the Q_{10} value, which indicates the rate of change when temperature increases by 10 °C. We measured a median value of 2.44 for the thalamic spindles in our pooled data (**Figure 1.3.1.2./e**). This fits in the range given for temperature dependence of neural oscillations, 2.3-2.7 (Deboer & Tobler, 1995), suggesting that this rate may be a general phenomenon in the central nervous system. Since in our protocol brain temperature changes followed body temperature, the examined parameters also correlated with core body temperature (**Figure 1.3.1.2./c**). In conclusion, spindle frequency increases with brain and core body temperature, accompanied by a decrease in spindle duration, leaving the average number of spindle cycles unchanged.

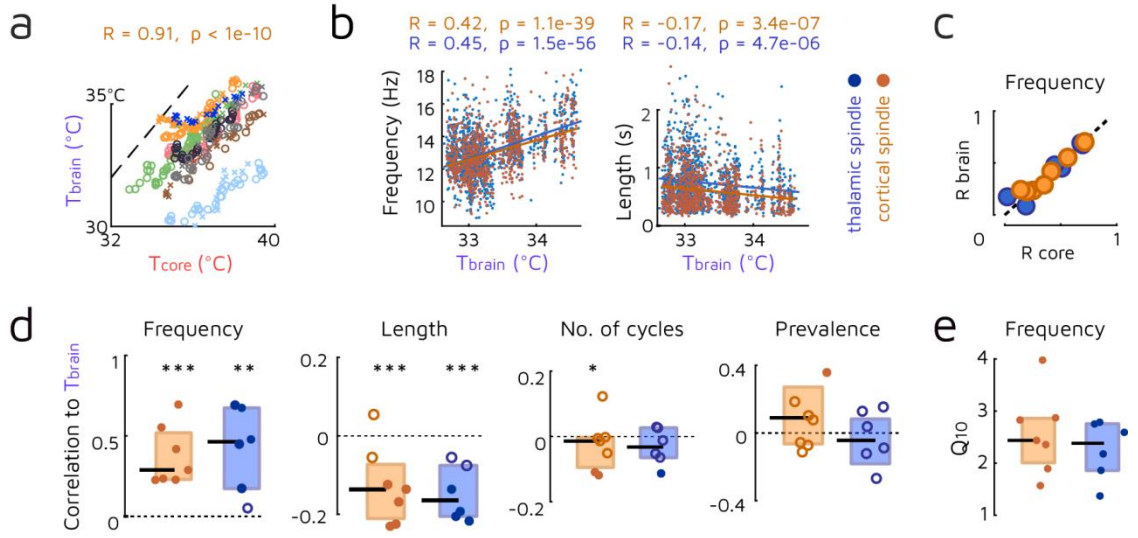

Figure 1.3.1.2. Sleep spindle frequency and length correlate with brain and core body temperature.

a/ Both under warming and cooling protocols, core body temperature correlates with brain temperature across multiple animals (n=8 mice). **b/** Both thalamic and cortical spindle frequency (left) correlate with brain temperature in the example experiment shown in **Figure 1.3.1.1./d**. Length of spindles has an inverse correlation with brain temperature (right). **c/** Modulation of spindle frequency is consistent across core and brain temperature (dotted line is unity). **d/** Pooled correlation coefficients show that temperature dependence of spindle frequency is a significant effect across animals. Spindle duration is negatively modulated, while the number of spindle cycles and spindle prevalence do not depend on brain temperature. *t-test,* *** p<0.005, ** p<0.01, * p<0.05). **e/** Median Q_{10} value of spindle frequency perfectly fits the biological range of 2-3.

Published in (Csernai & Borbély & Kocsis et al., 2019) Figure 1./E-I.

To assess whether the changing body temperature influenced the depth of anesthesia, (Csernai & Borbély & Kocsis *et al.*, 2019) also calculated the partial correlation of three cortical LFP frequency bands (delta, beta and gamma), with temperature controlled for the effect of time. Pooled partial correlation values were not significantly different from zero.

DOI:10.15774/PPKE.ITK.2022.002

Temperature dependence of sleep spindles can arise from biophysical mechanisms of the TC - Rt loop, via the direct or indirect temperature sensitivity of global modulatory systems, or a combination of both. This can be tested by local heating of the spindle-generating circuitry, while the rest of the brain, especially the contralateral thalamus remains at the resting temperature. The sensor filament of our thermoelectrode is capable of heating the surrounding tissue (**Figure 1.3.1.3./a**). Passing currents at or above 4 mA instead of the small 1 mA measuring current, the thermoelectrode increased tissue temperature in a gradual fashion up to 3 °C, and this heating effect remained relatively local (**Figure 1.3.1.3./b**). Also, the direct current passing the probe did not stimulate the unit activity electrically (Fekete *et al.*, 2017).

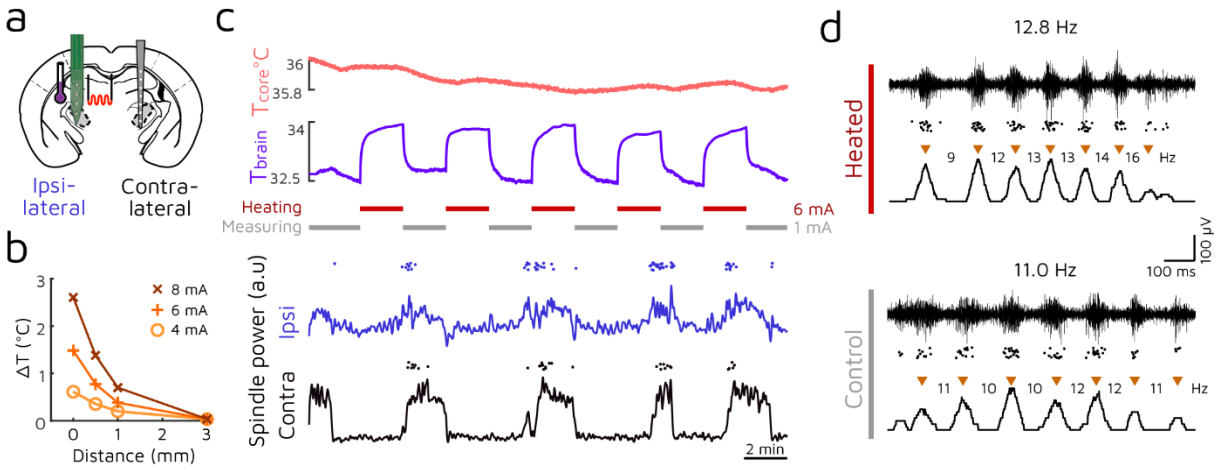

Figure 1.3.1.3. Local brain tissue heating with the thermoprobe.

a/ In one hemisphere, the VPM/VPL thalamus was locally heated with the thermoelectrode, while neural activity was recorded both locally and in the contralateral thalamus (n=7 mice). Temperature of the ipsilateral surrounding tissue was also monitored with a thermistor. **b/** Tissue temperature increases due to heating of the thermoelectrode filament with different currents. Note that tissue temperature decays sharply with distance from the thermoelectrode. **c/** The ipsilateral thalamus was heated in 2 min on / 2 min off cycles (top). Spindling epochs occurred irrespective of the heating cycle in both hemispheres (bottom, line: spindle power; dots: individual spindles). **d/** Representative examples of thalamic spindles during and without heating (black trace: high-pass filtered recording, dots: detected multi-unit, triangles: detected spindle cycles above the smoothed MUA). Note that unit activity and spindle structure are undisturbed.

Published in (Csernai & Borbély & Kocsis et al., 2019) Figure 2./A-D.

In these experiments, the thermoelectrode was inserted in the left VPM, from where temperature as well as LFP and MUA were recorded (n=7). The animals' core temperature was kept constant at 36 ± 0.2 °C. Heating currents applied in the brain were 4, 6 or 8 mA. In addition, we placed a linear electrode in the contralateral VPM for control recording (**Figure 1.3.1.3./a**). The heating current was applied in a cyclic protocol (2-minute heating / 2-minute measuring, **Figure 1.3.1.3./c**). The heating cycles did not disrupt the periodic recurrence of spindling epochs, as they appeared simultaneously with those on the contralateral hemisphere

DOI:10.15774/PPKE.ITK.2022.002

(**Figure 1.3.1.3./c** bottom), and they did not disturb the structure of spindles either (**Figure 1.3.1.3./d**).

As seen in **Figure 1.3.1.4./a**, application of three types of heating currents (4, 6 and 8 mA) produced a progressive increase in local spindle frequency as compared to the control periods. The phenomenon persists on a pooled data of 4 animals (**Figure 1.3.1.4./b**), from a small, but significant increase of spindle frequency at 4 mA to 20% increase at 8 mA. There was no significant increase at the contralateral thalamus, though a slight decrease in spindle frequency was often observable, not reaching significance level in the pooled data. Duration of the spindles also decreased significantly in the case of 8 mA heating by 25.7+/-3.8 % (p=0.019). These results imply that temperature dependence of spindle frequency is largely due to local biophysical mechanisms.

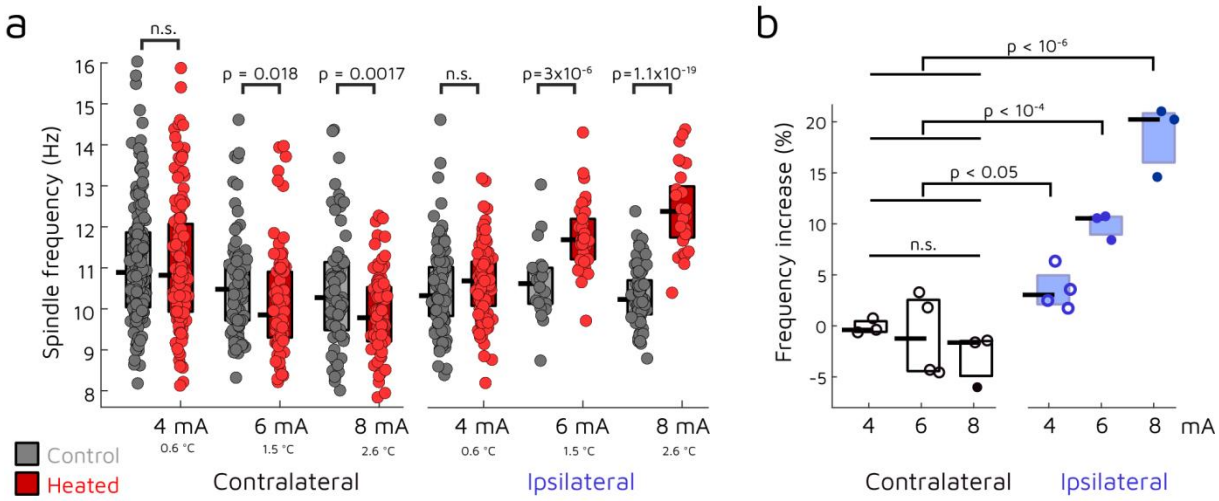

Figure 1.3.1.4: Temperature influences sleep spindles by a local mechanism.

a/ Representative data from an animal show that local heating induces significant increase in spindle frequency in the case of 6 and 8 mA heating currents, but no increase on the contralateral side. **b/** Pooled results of 4 animals show a gradual effect in thalamic spindle frequencies with an increasing heating current (open circles: non-significant effect, filled circles: significant effect with *two-sample t-tests* at p<0.01 as on **a**; pooled significance: *Mann-Whitney-Wilcoxon test*).

Published in (Csernai & Borbély & Kocsis et al., 2019) Figure 2./E-F.

To further elucidate the possible mechanisms of the temperature dependence of sleep spindles, (Csernai & Borbély & Kocsis *et al.*, 2019) created a thalamic network model consisting of single compartment TC and Rt cells. The model also revealed a marked correlation between spindle frequency and temperature adding further evidence for the biophysical nature of this effect.

DOI:10.15774/PPKE.ITK.2022.002

1.3.2. **Question Ib: How is the microarchitecture of brain temperature variations related to sleep spindles?**

So far, I have shown the temperature dependence of thalamocortical oscillations during external manipulation. Here, I would like to highlight the microarchitecture of baseline brain temperature variations, and their interrelation with sleep spindles.

With detailed inspection of the temperature traces under urethane anesthesia, I revealed that besides the gross changes induced by heating and cooling, brain temperature also shows periodic fluctuations on a scale smaller by one-two orders of magnitude. These fluctuations are superimposed on, and appear irrespectively of the absolute brain temperature (see also in (Fekete *et al.*, 2017).

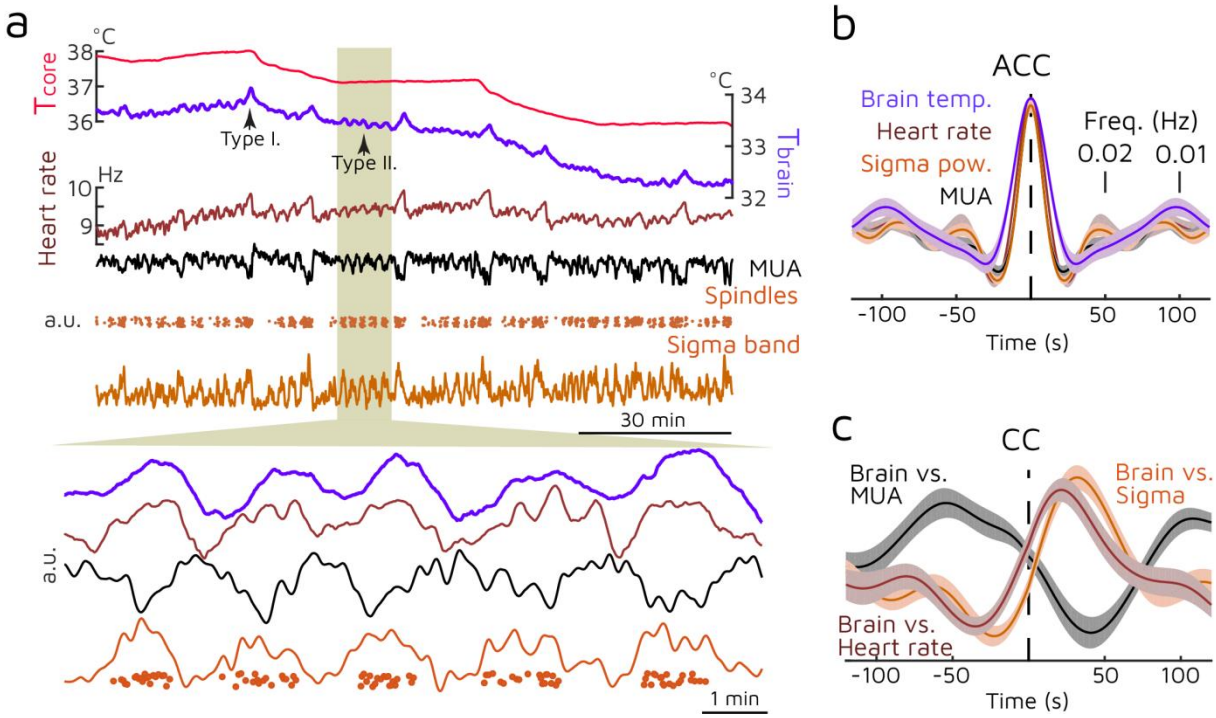

Figure 1.3.2. Microfluctuations in brain temperature accompany spindling epochs under urethane anesthesia.

a/ Example recording where microfluctuations of brain temperature, heart rate and spindle power appear to be in synchrony. On a finer time scale (zoom-in), sigma power, heart rate and brain temperature can be seen to oscillate together with an apparent temporal order between them. **b/** Averaged autocorrelograms of pooled urethane data show that these microfluctuations are in the infraslow frequency range (~0.02 Hz). **c/** Pooled cross-correlations (brain temperature vs. other) show that spindling and heart rate forego brain temperature fluctuation, while general thalamic MUA lags behind. Values on **b** and **c** are normalized.

Published in (Csernai & Borbély & Kocsis et al., 2019) Figure 4./A-D.

Based on their amplitude and frequency, two types of fluctuations could be differentiated (n=3; see **Table 1.** for details). 'Type I.' temperature fluctuations are larger (0.22 +/- 0.014 °C

DOI:10.15774/PPKE.ITK.2022.002

from baseline to peak) and reoccur on a ~10-minute time scale). ’Type II.’ temperature fluctuations are smaller (0.019 +/- 0.0008 °C from trough to peak), occur with a 0.022 Hz frequency, and they are interposed between the cycles of Type I. fluctuations (**Figure 1.3.2./a**).

Both types of fluctuations were associated with individual spindle events, an increase in MUA-derived sigma power, and an elevation of heart rate (**Figure 1.3.2./a** zoom-in). The periodicity of Type II. fluctuations (**Figure 1.3.2./b**) corresponds to the frequency of the infraslow oscillation (Lecci *et al.*, 2017), and there is a clear temporal order in them (**Figure 1.3.2./c**). Most importantly, thalamic spindling foregoes brain temperature spikes. Heart rate accompanies spindle activity, which is in contrast to their inverse relation observed in natural sleep (Lecci *et al.*, 2017; Csernai & Borbély & Kocsis *et al.*, 2019).

Furthermore, (Csernai & Borbély & Kocsis *et al.*, 2019) confirmed that Type I. fluctuations accompany REM sleep in chronically implanted mice, corresponding to the phenomenon described by (Kawamura & Sawyer, 1965); preceding spindling activity at both forms of temperature fluctuations was also shown in natural sleep.

DOI:10.15774/PPKE.ITK.2022.002

1.4. Discussion

1.4.1. **Thesis Ia**

With combined extracellular electrophysiological, core body and brain temperature recordings, I showed in urethane-anesthetized mice that sleep spindle frequency increases, length decreases with core and consequently with brain temperature. Local tissue warming reproduces the effects only on the heated spot, suggesting a local biophysical mechanism.

Related journal publication: Csernai, M.*, Borbély, S.*, Kocsis, K.*, Burka, D., Fekete, Z., Balogh, V., Káli, S., Emri, Z., and Barthó, P. (2019). Dynamics of sleep oscillations is coupled to brain temperature on multiple scales. *Journal of Physiology 597(15)*, pp. 4069–4086.

I participated in the conception, design and methodological foundation of the experiments, the acquisition, analysis and interpretation of the acute electrophysiological and temperature data. I took part in the drafting and revision of the related section of the manuscript.

Though temperature dependence of EEG rhythms has been described before, to my knowledge, this is the first *in vivo* study to integrate LFP and MUA recordings with brain temperature measurements on a single device, as well as use local heating to explain the underlying mechanism (**1.3.1.**).

(Hoagland, 1936) described higher frequency alpha-rhythms in patients undergoing hyperpyretic treatment, a reduction in barbiturate-spindle frequency was found during cooling in cats (Andersen *et al.*, 1967), and similar results were found in infants during surgical hypothermia – together with an increase in spindle duration (Schmitt *et al.*, 2002). Also, (De Vera *et al.*, 1994) examined EEG activity in *Gallotia galloti* (Western Canaries lizard), and found that the frequency of spindle-like activity increases with body temperature, though these oscillations produce a continuum from 2-30 Hz, marking them as a different rhythm from mammalian spindles. A robust decrease in all EEG frequencies, especially theta has been found in hibernating Djungarian hamsters (Deboer & Tobler, 1995; Deboer, 1998). My results are generally in line with these results, as the frequency of spindle oscillations showed a positive correlation with core body and brain temperature.

The frequency range of spindles is suited for inducing LTP in cortical circuits (Rosanova & Ulrich, 2005), so any change in the frequency of this oscillation is likely to affect synaptic potentiation. Indeed, a 2° C drop in body temperature has been shown to markedly reduce information recall (Coleshaw *et al.*, 1983).

Another aspect of thalamocortical oscillations can be the binding hypothesis (Nikolić *et al.*, 2013), stating that oscillations create a temporal window for selected groups of neurons so

they can fire in synchrony to form a representation. Although it was originally proposed for gamma oscillations in awake subjects, spindles may operate similarly in a different scenario, in which case, spindle frequency also has a crucial role. An alternative would be that the information carried by spindles is determined by the different cohorts of neurons involved in each cycle. Here, the increase in spindle frequency was accompanied with a smaller decrease in spindle duration, leaving the number of cycles per spindle unchanged by temperature. This would mean that the observed changes actually reflect the robustness of information encoding in spindles with regard to brain temperature.

Local heating of the thalamus alters spindles ipsi- but not contralaterally, thus, temperature-dependent modulation of sleep spindle frequency most likely originates from biophysical properties of local circuits, instead of the temperature sensitivity of global modulatory mechanisms.

The main thermoregulatory center in the brain is the preoptic area (POA) of the hypothalamus. POA receives input from peripheral thermoreceptors, but also contains intrinsically heat-sensitive neurons that are hypothesized to monitor changes in brain temperature. The same region contains neurons that project to several modulatory centers (Peterfi *et al.*, 2009) involved in sleep maintenance. Also, POA warm-sensing neurons are known to be active during sleep (Alam *et al.*, 1996). Therefore, it is reasonable to suggest that body temperature could influence sleep rhythms via the posterior hypothalamus. In fact, there is a possibility that local heating in the thalamus also warms the hypothalamic POA to a certain degree.

Notably, there is an adverse effect on the contralateral side that might arise from increased hypothalamic temperature sensation or an altered blood perfusion on the contralateral side, but it is a magnitude smaller and non-significant compared to the effect of local tissue heating.

My data show that body along with brain temperature changes has an important but underrated role in sleep quality. Age, sex and physiological condition of the subjects can all have an influence on body temperature changes and general thermoregulatory capacities. Pharmaceutics and other medical or experimental interventions can alter brain temperature, leading to spindle frequency changes as high as 2-3 Hz, which is also needed to be taken into consideration for the planning, execution and analysis of both animal research and medical procedures.

DOI:10.15774/PPKE.ITK.2022.002

1.4.2. **Thesis Ib**

I showed in urethane-anesthetized mice that baseline microfluctuations in brain temperature are associated with sleep spindle oscillations. Besides the larger, REM-like periodic elevation of brain temperature, smaller temperature variations correspond to the infraslow oscillation (~0.02 Hz).

Related journal publication: (Csernai & Borbély & Kocsis *et al.*, 2019)

I performed the first analyses and gathered the preliminary evidence for the baseline microfluctuations in brain temperature, which are marked by the co-modulation of brain temperature and sleep spindles. I took part in the methodological foundation of the analysis, as well as the interpretation of the acute electrophysiological and temperature data. I took part in the drafting and revision of the related section of the manuscript.

Besides brain temperature influencing neural oscillations, spontaneous changes of brain states may alter brain temperature, too. Brain temperature elevations, on the order of 10^{-1} to 10^{-2} °C, correlating with EEG synchronization have been previously reported in rats (Kovalzon, 1973), and also in the unihemispheric sleep of dolphins and a harbor porpoise (Kovalzon & Mukhametov, 1983). I found that spindling epochs are associated with elevated brain temperature on these time scales (**1.3.2.**).

Larger elevations (order of 10^{-1} °C) can correspond to REM activity, observed in certain mammals (Hayward & Baker, 1969), but the cause of this phenomenon has not been directly proven. Nevertheless, mammals in thermally challenging aquatic environments, such as cetaceans (Lyamin *et al.*, 2008) as well as semiaquatic Northern fur seals (Lyamin *et al.*, 2018) predominantly show unilateral slow-wave sleep and a negligible REM activity. This supports the hypothesis according to which REM serves a transient recovery from a reduced metabolism and brain temperature brought about by bihemispheric NREM sleep, thus, it may serve energy conservation in terrestrial species.

On a smaller scale (order of 10^{-2} °C), brain temperature fluctuates in synchrony with the infraslow oscillation (0.02 Hz), including sigma power, individual spindle events as well as heart rate. This finding has been reviewed by (Fernandez & Lüthi, 2020), highlighting the clustering of sleep spindles on the 0.02 Hz infraslow time scale, which follows the alternation of fragile and continuous NREM periods. The infraslow oscillation has been observed in rodents, carnivores and humans (Steriade *et al.*, 1993; Lőrincz *et al.*, 2009; Lecci *et al.*, 2017), modulating LFP sigma band as well as heart rate (Lecci *et al.*, 2017), pupil size (Blasiak *et al.*, 2013), and fMRI BOLD signal (Mantini *et al.*, 2007). Its expression in TC population activity can originate from local astrocytes (Lőrincz *et al.*, 2009), a subpopulation of which has been shown to generate pacemaker calcium oscillations at ~0.019 Hz (Parri & Crunelli, 2001).

DOI:10.15774/PPKE.ITK.2022.002

What can be the cause of the temperature microfluctuations? Physiological and pathological temperature changes of the brain can be directly derived from the changes of local metabolism, cerebral blood perfusion, and blood temperature (Hayward & Baker, 1969; Wang *et al.*, 2014). In our case, temperature elevations were correlated with increased multi-unit activity, which, together with local astrocyte signaling, may raise temperature directly, or via enhancing the local blood flow.

Overall, these oscillatory phenomena point to a tight temporal coupling of metabolic and hemodynamic changes with neuronal network mechanisms, which are co-modulated on multiple time scales.

1.5. Relevant publications of the author

1.5.1. Peer-reviewed articles

Publication supporting the theses

- Csernai, M.*, Borbély, S.*, Kocsis, K.*, Burka, D., Fekete, Z., Balogh, V., Káli, S., Emri, Z., Barthó, P. (2019): Dynamics of sleep oscillations is coupled to brain temperature on multiple scales. *Journal of Physiology, 597(15),* pp. 4069-4086. https://doi.org/10.1113/JP277664

*shared first authorship

Other relevant publications

- Fekete, Z., Csernai, M., Kocsis, K., Horváth, Á. C., Pongrácz, A., Barthó, P. (2017): Simultaneous in vivo recording of local brain temperature and electrophysiological signals with a novel neural probe. *Journal of Neural Engineering, 14(3)*. 034001 https://doi.org/10.1088/1741-2552/aa60b1

- Horváth, Á. C., Kocsis, K., Csernai, M., Barthó, P., Fekete, Z. (2016): A Novel Neural Probe for Simultaneous Electrical Recording and Local Thermal Control in Sleep Spindle Oscillation Studies. *Procedia Engineering, 168*, pp.109-112. https://doi.org/10.1016/j.proeng.2016.11.159

1.5.2. Conference presentations

1.5.2.1. First-author presentations

- Kocsis, K., Csernai, M., Horváth, Á., Fekete, Z., Barthó, P. (2016): Body temperature modulates sleep spindle frequency. Poster, IBRO Workshop, Budapest, Hungary.
- Kocsis, K., Csernai, M., Horváth, Á., Fekete, Z., Barthó, P. (2016): Body temperature modulates sleep spindle frequency. Poster, HuNDoC, Budapest, Hungary.
- Kocsis, K. (2015): Effects of body temperature on the occurrence and parameters of sleep spindles. Talk and conference paper*, PhD Proceedings, Annual Issues of the Doctoral School, Faculty of Information technology and Bionics, 10*: pp. 65-68.
- Kocsis, K., Csernai, M., Barthó, P. (2015): Spindle frequency is modulated by body temperature. Poster, 15th Biannual Meeting of the Hungarian Neuroscience Society, Budapest, Hungary.

1.5.2.2. Co-author presentations

- Csernai, M., Kocsis, K., Burka, D., Borbély, S., Fekete, Z., Balogh, V., Káli, S., Emri, Z., Barthó, P. (2018): Sleep spindle frequency is modulated by temperature in vivo and in silico. Poster, FENS Forum, Berlin, Germany.
- Csernai, M., Kocsis, K., Burka, D., Borbély, S., Fekete, Z., Balogh, V., Káli, S., Emri, Z., Barthó, P. (2017): Temperature modulates sleep spindle frequency in vivo and in silico. Poster, Annual Meeting of the Society for Neuroscience (Neuroscience 2017), Washington DC, U.S.
- Fekete, Z., Kocsis, K., Horváth, Á., Barthó, P. (2016): A novel neural probe for simultaneous electrical recording and local thermal measurements in sleep spindle oscillation studies. Poster, Biosensors 2016, Göteborg, Sweden.

The infrastructural basis of this research was funded by the Hungarian Brain Research Program (2017-1.2.1-NKP-2017-00002 to Dr. Péter Barthó).

DOI:10.15774/PPKE.ITK.2022.002

1.6. Outlook: potential for the study

Robustness in neuronal rhythm generation and sleep can be highly dependent on external and internal thermal conditions. This is an adaptive challenge for many wild species exposed to a changing climate, but also for humans whose behavioral thermoregulation is impaired, such as the disabled and the elder (Collins *et al.*, 1981) as well as those suffering from neurological illnesses.

As peak density of spindles was measured during the maximal decrease in core temperature (Dijk & Czeisler, 1995), I also observed increased spindle activity in the decaying phase of core and brain temperature modulation (see **Figure 1.3.1.1./d**), with the oscillations being sparser during the periods of rising temperature. This observation also suggests that higher body temperatures (e.g., fever) can disrupt neural oscillations.

There is an epidemic of sleep disturbances, which are often diagnosed as comorbidity in many diseases and psychiatric disorders. Studying the interdependence of core/peripheral body temperature, neuronal network activity and blood perfusion can further our understanding on many debilitating conditions and on their possible treatments. Interventions which target the intensity, area, duration and timing of body and brain temperature fluctuations can be crucial in improving sleep quality in a large population (Van Someren, 2000, 2004; Raymann *et al.*, 2008).

DOI:10.15774/PPKE.ITK.2022.002

PART 2 Study of aversive cue discrimination in the thalamus

<< The theory which naturally presents itself is that *the peculiar quality of emotion is added to simple sensation when the thalamic processes are roused.* >> (Cannon, 1929)

2.1. Background and motivation of the study

There are many burning questions regarding how affective interpretation of environmental stimuli is established. One of them is how subcortical (or precortical) neural processing detects and channels aversive signals in order to achieve efficient and imminent discrimination under threat, ultimately promoting survival.

In natural habitats, predation pressure shapes sensory processing and arousal regulation in prey animals. It creates a dynamic *landscape of fear*[2], which results in different patterns of antipredator behavioral states (e.g., vigilance, foraging). Besides the advantage of an increased alertness or readiness, adaptive behavior relies on a form of sensory processing which channels aversive signals into a robust neuronal pathway that requires relatively few synapses.

Subcortical evaluation of external cues often precedes the extensive and fine processing of their physical properties, helping to elaborate adaptive behavior. Besides providing a filtering function for ethologically relevant cues, subcortical areas are also exposed to top-down modulation that leads to perceptual/cognitive biases in information processing (McFadyen *et al.*, 2020).

2.1.1. The direct thalamo-amygdala pathway

Even with telencephalic expansion, vertebrate brains strongly rely on affective processing without perceptual awareness (Tamietto & De Gelder, 2010) to orchestrate fast defensive responses. Charles Darwin proposed the adaptive origin and value of emotions (Darwin, 1872), which, across species, promote beneficial behavioral responses with conserved features, such as defensive actions. Besides fight or flight, first described by (Cannon, 1929), animal studies have shown a so-called *defense cascade*, a continuum of innate defensive behaviors (freezing, flight or fight, tonic immobility, and quiescent immobility), depending on threat imminence and graveness (Fanselow & Lester, 1988).

The monosynaptic, subcortical connections between the thalamus and the amygdala, two evolutionarily conserved brain structures, have been proposed as key routes in fast (and non-

[2] Ecological term; the spatial variation in prey perception of predation risk (Gaynor *et al.*, 2019).

DOI:10.15774/PPKE.ITK.2022.002

conscious) evaluation and behavioral responses, especially in innate visually evoked aversive behavior (Morris *et al.*, 1999; Almeida *et al.*, 2015; Wei *et al.*, 2015).

A fast and effective response to threats requires indeed a neural bypass from elaborated cortical processes. The pivotal role of direct thalamo-amygdala routes was also revealed in learned aversive responses given to auditory stimuli. Auditory fear conditioning is a historical, Pavlovian (classical) behavioral paradigm used to establish robust aversive learning. It drives lab rodents to associate a previously neutral cue (conditioned stimulus, CS; e.g., a sine wave) to an aversive (unconditioned) stimulus (US; e.g., electric foot shock) (LeDoux, 1994; Blair *et al.*, 2001; Pape & Pare, 2010). According to a vast literature, this multisensory integration and memory formation can be tracked by synaptic changes in the lateral amygdala (LA) (Nabavi *et al.*, 2014). Consequently, the future presentation of the CS reliably elicits defensive responses, such as freezing or escaping. Nevertheless, the question arises about the nature of this plasticity regarding the inputs arriving to amygdala territory.

Based on anatomical evidence showing no primary sensory connections at the amygdala**,** the study of the conveyed thalamic modalities, their cellular origin as well as their effector mechanism in the amygdala, has become well motivated.

Data from *in vivo* recordings suggest a short-latency (<20 ms) (Quirk *et al.*, 1995) transmission of CS information to the amygdala, which requires fast, probably subcortical inputs to the LA, bypassing the multisynaptic sensory cortical routes. The thalamus, which is known to innervate cortical regions, has its distinct connection to the amygdala, too (**Figure 2.1.1./a**).

Studies in the 80s revealed a shortcut to the amygdala, formed by diverse and distinct cell populations in the posterior region of the medial geniculate body (MGN), the primary thalamic station of auditory processing (**Figure 2.1.1./b**). These lateral thalamic regions, including the posterior intralaminar (PIL) and suprageniculate (SG) thalamic nuclei as well as the medial and dorsal part of the medial geniculate nucleus (MGM and MGD, respectively) form monosynaptic connections with the LA (LeDoux *et al.*, 1990). In particular, the MGM is traditionally accepted as the major source of auditory CS (LeDoux *et al.*, 1984; Quirk *et al.*, 1995).

The source of US information in the LA that can temporally match the CS signal is rather debated. Neurons in the parabrachial nucleus (PB) (Han *et al.*, 2015) and periaqueductal grey (PAG) (Johansen *et al.*, 2010; Kim *et al.*, 2013) are activated by US and have been shown to affect fear learning. However, these nuclei cannot provide the LA with a short-latency (10-20 ms) US signal, that is necessary for signal association (Quirk *et al.*, 1995), due to the lack of monosynaptic connections.

DOI:10.15774/PPKE.ITK.2022.002

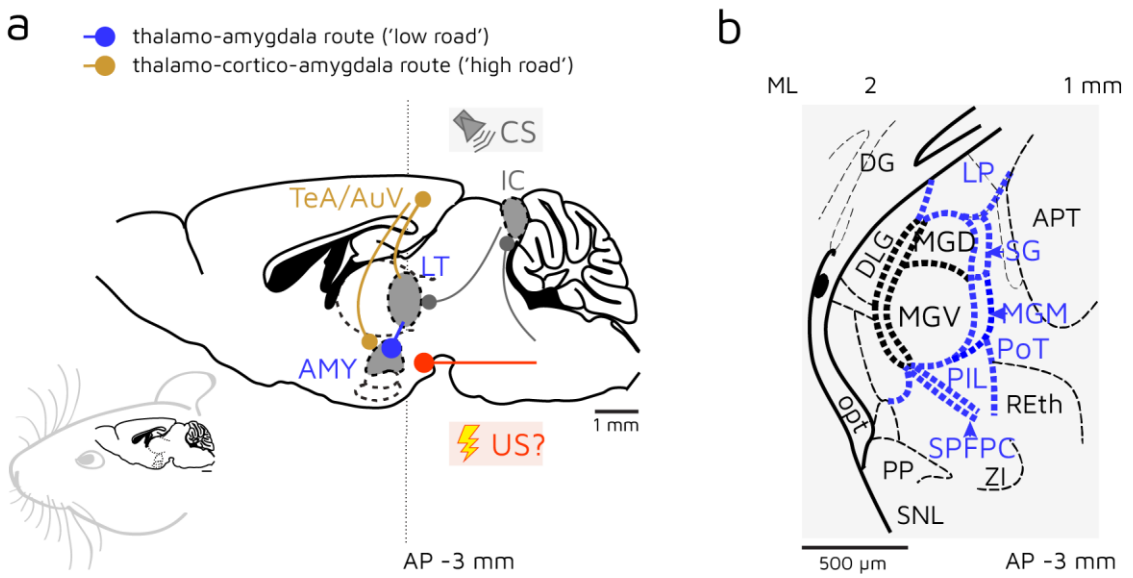

Figure 2.1.1. The duality of thalamo-amygdala pathways, and the lateral thalamic regions shown to project to the amygdala.

a*/* Scheme for the direct (blue) and indirect (brown) routes between the mouse lateral thalamus (LT) and amygdala (AMY), specified for auditory stimuli (conditioned stimulus, CS), which are preprocessed by the auditory midbrain (inferior colliculus, IC). The route of nociceptive information (unconditioned stimulus, US; red) to the amygdala is still under debate. **b***/* Subnuclei in the auditory thalamic region, which have been shown to project to the amygdala (e.g., (LeDoux *et al.*, 1990; Wei *et al.*, 2015). These non-canonical 'belt' regions surrounding the primary auditory thalamus, the medial geniculate body, are delineated with dashed blue lines. LP: lateral posterior thalamic nucleus (t. n.); SG: suprageniculate t.n.; MGM: medial geniculate nucleus, medial part; PoT: posterior thalamic nuclear group, triangular part; PIL: posterior intralaminar t.n.; REth: retroethmoid n.; SPFPC: subparafascicular t.n., parvicellular part; PP: peripeduncular n.; SNL: substantia nigra, lateral part; ZI: zona incerta; opt: optic tract; DG: dentate gyrus; DLG: dorsal lateral geniculate nucleus. Excerpt taken from (Paxinos & Franklin, 2003).

Amygdala-targeting dorsomedial thalamic nuclei including the paraventricular thalamus have been shown to mediate fear memory establishment as well as retrieval (Do-Monte *et al.*, 2015; Penzo *et al.*, 2015) by encoding arousal (Mátyás *et al.*, 2018) and stimulus saliency (Zhu *et al.*, 2018). Yet this medial thalamic population mostly targets the basal and central amygdala (Mátyás *et al.*, 2018), thus, it is unlikely to transfer signal for multisensory association. Alternatively, the LA may receive innately aversive (US) information directly from some of the above-mentioned lateral thalamic regions (Shi & Davis, 1999; Lanuza *et al.*, 2008) which can potentially convey CS as well.

It has still remained speculative how sensory inputs reach the LA and trigger cue association despite the fact that extensive but sporadic pieces of literature (see review by (Weinberger, 2011)) described the possibility of an associative auditory-nociceptive CS-US convergence and response facilitation in the lateral thalamus. The revealed locations were the MGM or PIL, also named PIN, in guinea pigs (Cruikshank *et al.*, 1992; Edeline & Weinberger, 1992), in cats

(Ryugo & Weinberger, 1978), in rats (Bordi & LeDoux, 1994*a*), in rabbits (McEchron *et al.*, 1995), and in mice (Han *et al.*, 2008) as well.

However, lesioning of these thalamic areas yielded contradictory findings regarding the outcome of auditory threat conditioning (LeDoux *et al.*, 1984; Romanski & LeDoux, 1992; Campeau & Davis, 1995; Lanuza *et al.*, 2004; Halverson & Freeman, 2006). Moreover, the diversity of thalamic nuclei, an ever-changing anatomical delineation and inconsistent terminology across species and studies as well as the focus on sole and purely sensory modalities in the thalamus derailed the tendencies that highlighted the integrative and operative thalamic role in learned threat-evoked behaviors.

2.1.2. The ‘non-canonical’ collothalamic lateral thalamus

What has also been dismissed in the amygdala literature is a distinction of amygdala-projecting lateral thalamic neurons from sensory pathways by their overall connectivity. These neurons compose a so-called extrageniculate sensory pathway receiving multiple sensory information and projecting to higher-order cortical areas (Linke & Schwegler, 2000) besides their fear memory related subcortical targets, the lateral amygdala (LA) and the amygdalostriatal transition area (AStr) (LeDoux *et al.*, 1987).

Cladistic analysis by (Butler, 1994) divided the dorsal thalamus into lemnothalamic and collothalamic divisions. The latter refers to nuclei that receive indirect sensory pathways, which synapse in the midbrain, such as the auditory and tectofugal pathway, in contrary to a direct (lemniscal) innervation. Collothalamic regions were shown to be homologous in all jawed vertebrate radiations as discrete nuclei. According to (Aboitiz *et al.*, 2002), the reptilian anterior dorsal ventricular ridge (AVDR) – the input structure of the pallial amygdala-homolog PDVR (posterior dorsal ventricular ridge) – and the mammalian laterobasal amygdala both receive collothalamic inputs.

This heritage in the mammalian brain has a reminiscent role in threat-related behaviors that need the fastest possible route to execute adaptive motor function for survival. Accordingly, excitatory and inhibitory collicular computation and convergence (Smith *et al.*, 2007), bypassing primary sensory processing, can ensure emergent and distinct receptive fields as well as a relay of integrated cues for downstream lateral thalamic targets.

There is another line of evidence in literature, which suggests that amygdala-projecting thalamic populations are not part of the primary sensory processing. Based on their driving inputs, they do not fit into the driver/modulator framework (Sherman & Guillery, 1998), as they are innervated by superior collicular (SC) terminals (Smith *et al.*, 2007), which are not classical drivers. Though they are relatively large, glutamatergic and target proximal dendrites, they tend

DOI:10.15774/PPKE.ITK.2022.002

to converge on thalamic neurons, do not elicit either frequency-dependent facilitation or depression, and have a distinct set of presynaptic proteins (Bickford, 2015). In brief, tectorecipient thalamic nuclei cannot be defined as either first- or higher-order.

Primary and non-primary regions in the auditory thalamic area can also be distinguished by their complementary calcium-binding protein content, by parvalbumin (PV) vs. calbindin (CB) / calretinin (CR), respectively (Lu *et al.*, 2009). According to (Schwaller *et al.*, 2002), these proteins are functionally distinct modulators of intracellular calcium transients and regulators of calcium pools for synaptic plasticity.

(Smith *et al.*, 2006) also revealed in rats that members of the 'paralaminar group', MGM, SG and PIN as well as the peripeduncular (PP) nucleus show unique features compared to regular thalamocortical neurons. Beside neuroanatomical differences, many of them exhibit a reduced or no low-threshold Ca^{2+}-mediated burst at all. (Bartlett, 2013) hypothesized that the lack of bursts might 'exempt' these neurons from sleep rhythms and keep them responsive to behaviorally relevant sounds.

Based on the aforementioned observations, the need arises for the functional dissection of the thalamic cohort that projects to the amygdala setting the basis for robust and preconscious affective processing in threatening experiences. **In this part of my studies, combining broadband extracellular electrophysiological, anatomical, and behavioral methods, I was driven to provide new insight into the lateral thalamic role in aversive learning.**

- I studied the responsivity of cells in the non-canonical auditory thalamic region to neutral as well as to single and associated aversive (threat-derived) cues in urethane-anesthetized and freely behaving mice (**Aim IIa**);
- I intended to elucidate whether lateral thalamic neurons can directly convey single and associated aversive cues to the lateral region of the amygdala (**Aim IIb**);
- I investigated the possible collicular underpinnings for the time-course of activation and cue-responsivity of the direct lateral thalamo-amygdala route (**Aim IIc**).

DOI:10.15774/PPKE.ITK.2022.002

2.2. Materials and Methods

2.2.1. **Experimental subjects and ethical considerations**

Adult (>3 months old) Calb2-Cre, vGAT-Cre and vGluT2-Cre (donated by Prof. Dr. Z. Josh Huang, Prof. Dr. László Acsády and Sébastien Arthaud, respectively) mice of both sexes were chosen for the study. All animals were group-housed in a humidity- and temperature-controlled (22 ± 2°C) environment. They were entrained to a 12:12 h light-dark cycle (light phase from 7:00) with food and water available *ad libitum*. Experiments were conducted during the light phase. From 10-15 days before behavioral experiments, animals were individually housed and habituated to handling.

Significant efforts were made to minimize the number and the stress level of the subject animals. Mice were administered paracetamol (Panadol, 0.3 mg/ml, GSK) in their drinking water for 3-4 days after surgery in order to alleviate postoperative pain. Experiments were carried out in accordance with the Hungarian *Act XXVIII of 1998* and with the *Directive 2010/63/EU.* All procedures were approved by the Regional and Institutional Committee of the Research Centre for Natural Sciences (license number PEI/001/2290-11/2015). I was authorized to performed experiments by the Semmelweis University's Institutional Animal Care and Use Committee (Certificate No. 89./2014).

At the end of all experiments, anesthetized mice were transcardially perfused with saline, then, with ~150 ml of fixative solution (4% PFA dissolved in 0.1 M phosphate buffer (PB)). 50 µm coronal sections were cut from their fixated brains (Leica vibratome).

2.2.2. **Stereotaxic surgeries**

2.2.2.1. General procedure

Mice were temporarily sedated with isoflurane inhalation (Isofluran CP, CP-Pharma) before ketamine-xylazine administration (CP-Ketamin 10% and CP-Xylazin 2% in 5:1, 3x dilution in physiological saline (PS), IP; Produlab Pharma) in the case of AAV injections or tetrode implantations, and urethane injection (20% in distilled water, 1.2 g/kg, IP) in the case of acute recordings. Immobile animals were then placed into a stereotaxic apparatus (Kopf Instruments or RWD Life Science); their eyes were meanwhile protected from dehydration with eye gel (Oculotect, Novartis or Corneregel, Bausch & Lomb). Before and after skin excision, the surgical area was treated with local anesthetic (10% Lidocain, EGIS). Craniotomies were made over the target brain areas, glass pipettes (for virus injection) or electrodes were manually lowered into the brain at a speed below 0.05 mm/s. After electrode insertion, I waited for about 60 minutes before starting recording in order to let the target brain tissue recover. Body

temperature of mice was kept stable at 38° C with a heating pad (TMP-5b Physiological-Biological Temperature Controller, Supertech Instruments).

2.2.2.2. Injection of adeno-associated viral (AAV) vectors

AAV5-EF1a-DIO-**hChR2**(H134R)-**eYFP**-WPRE-hGH,AAV5-EF1a-DIO-**eYFP**-WPRE-hGH, AAV9-EF1a-DIO-**eNpHR3.0-eYFP**-WPRE-hGH constructs (50-50 nl; Penn Vector Core or UNC; titer: $5x10^{12}$-$1x10^{13}$ genome copies(GC)/ml) were injected unilaterally at a rate of 1-2 nl/s into the PIL/SG (AP/L/DV: -3.1/±1.9/3.2-2.8 mm), SC (-4/0.9/0.5-1 mm), IC (-5.1/1.5/0.5-0.8 mm) and the LA/AStr (-1.8/3.5/3.8 mm) using a Nanoliter 2010 Injector (World Precision Instruments). >3 weeks were left for Cre-dependent virus transduction and animal recovery.

2.2.2.3. Implantation of tetrodes and optic fibers

Calb2-Cre mice (n=33) were unilaterally injected with AAV-DIO-ChR2-eYFP into the amygdala or the thalamus. 4-6 weeks after AAV injection, four custom fabricated tungsten tetrodes (12.5 µm wire diameter, California Fine Wire) were chronically implanted into the lateral thalamus (LT) and also into the amygdala in additional cases. They were inserted along with a multimode optic fiber (105 µm core diameter, NA = 0.22; Thorlabs), all tunneled in a polyimide tube (203 µm internal diameter, Neuralynx, **Figure 2.2.2./a**).

The tetrode wires were attached to an electrode interface board (EIB-16 and EIB-36 Narrow, Neuralynx) using gold electrode pins (Neuralynx). The ground and reference wires were soldered to the EIB. The tetrodes were cut to final length in an acute angle (200-400 µm left between the optic fiber and tetrode tips) with fine tungsten carbide scissors (Fine Science Tools). This maneuver helped to cause less tissue damage, and to avoid recording from overlapping sets of neurons with different tetrodes. Target impedances measured at 1 kHz (nanoZ, Plexon) in PS were between 300-700 kΩ (**Figure 2.2.2./b**).

Ground and reference screw electrodes were driven into the occipital and parietal bones, respectively. An extra screw in the frontal bone served the stability of the implant. The tetrode wires were disinfected with absolute alcohol before a slow (<0.05 mm/s) insertion into the target areas (thalamus: Br. AP -3.1, ML +1.85, in 0º at 3250 µm maximum depth, or Br. AP -3.7, ML +1.85, in 10º at 3300-3350 µm maximum depth, and amygdala: Br. AP -1.6, ML +3.55-3.75, in 0º at 3950-4050 µm maximum depth).

Finally, all pieces were secured onto the skull with multiple layers of dental acrylic (Paladur, Kulzer) and shielded with a copper web (**Figure 2.2.2./c**). Mice were left to recover for at least 7 days and then habituated to handling for several days.

DOI:10.15774/PPKE.ITK.2022.002

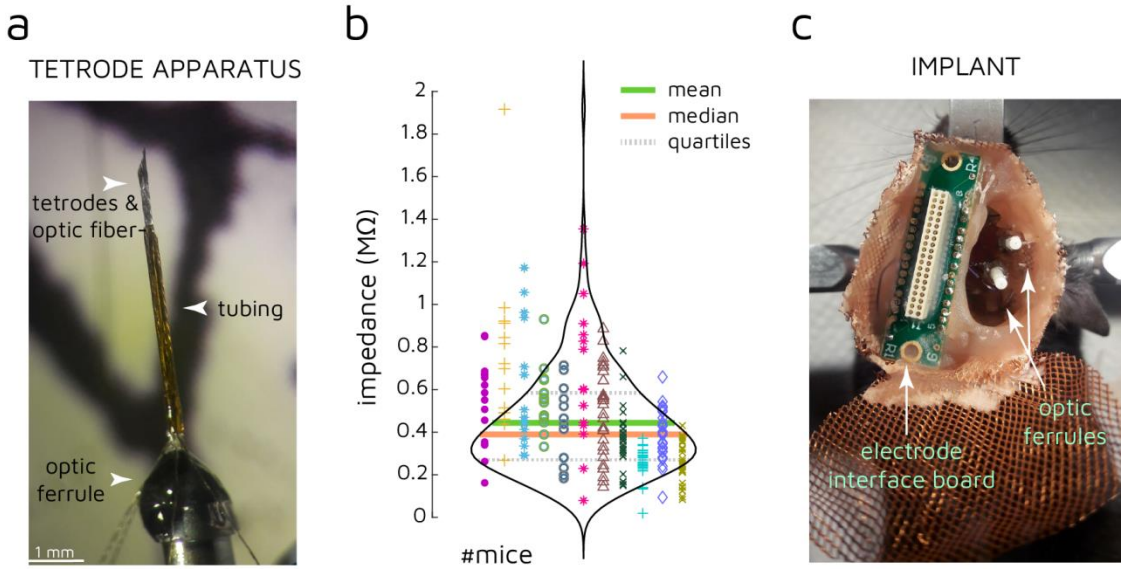

Figure 2.2.2. Tetrode implantation for experiments with freely moving mice.

a/ A tetrode apparatus with four custom fabricated tungsten tetrode electrodes glued into a polyimide tube together with an optic fiber. **b/** Tetrode channel impedances for each animal with neural data shown in section **2.3.1.** Note that the majority of tetrode channel impedances were in the target 0.3-0.7 MΩ range. Bad or missing (torn wire) contacts are discarded. **c/** After tetrode insertion, the interface board together with the wires, screws and the copper web shield were fixed onto the skull with dental acrylic.

2.2.3. **Electrophysiology**

2.2.3.1. Acute *in vivo* electrophysiological recordings

Neural data acquisition was performed in urethane-anesthetized, virus (AAV-DIO-ChR2-eYFP or AAV-DIO-NpHR3.0-eYFP) injected Calb2-Cre and vGlut2-Cre mice in order to study auditory and nociceptive cue processing along the direct thalamo-amygdala route. All recordings were done ipsilaterally to the sites of viral injection. Thalamic (n=16 mice) activity was monitored with 32-channel Buzsáki32 silicon probes, amygdala (n=25 mice) recordings were done with 32-, 64-, or 256-channel probes (Buzsáki32, Buzsáki64 with 200 µm and Buzsáki256 with 300 µm inter-shank spacing, respectively; NeuroNexus Technologies). All probes were stained with alcoholic DiI solution for further track reconstruction. Wideband neural data (0.1-7500 Hz) were amplified (gain: 192 or 400 V/V), and digitized at 20 kHz (RHD2132 or RHD2164, Intan Technologies or Amplipex in 256-channel recordings). A screw driven into the occipital bone served as reference electrode.

Orthodromic and antidromic optogenetic activations with multimode optic fibers (105 µm core diameter) were done in order to identify the elements of the direct calretinin-positive (CR+) thalamo-amygdala pathway as well as mark the vGluT2+ colliculo-thalamo-amygdala route. In the case of antidromic photoactivation, axon terminals of CR+ lateral thalamic (CR+LT)

neurons were activated in the amygdala, causing the backfiring of amygdala-projecting thalamic cells. The amygdala contains no CR+ cells that project back to the LT (unpublished observation of our research group), so thalamic responses were due to direct antidromic activation. Optogenetic activation consisted of 473 nm blue light pulses (5 ms at 0.5-1 Hz or 10-50-100-200 ms with 1-10 s intervals; 10-15 mW, Laserglow Technologies) that only served for the identification of virally transduced neurons.

In the case of acoustic stimulations, the animal's head was fixed with a head plate in the stereotaxic frame, allowing sound delivery into the ear contralateral to the recording site. Auditory and foot shock-evoked responses were tested in the thalamus and the amygdala subnuclei as well. The auditory signal was a 7.5 kHz pure tone (1 s or 30 s, 75-85 dB) with a Tukey (tapered cosine) window for 10-10 ms long rise time and fall time. Foot shock was achieved by bipolar electric stimulation (50/100 ms or 1 s, 1 mA) of a paw, which resulted in pain reflex. The two types of cues were also paired in order to form a multimodal signal. Unimodal auditory and foot shock as well as associated stimuli were repeated 10, 10 or 15, 10 times in case of thalamic and 50, 10 or 15, 20 times, respectively, in amygdala recordings, keeping 2-5-minute interblock intervals. Interstimulus intervals (ISI) were 30-60 s. Longer sensory cues were delivered in a pseudorandom order.

Halorhodopsin-mediated (Mahn *et al.*, 2016) CR+ axonal inhibition was done with 532 nm green laser stimuli (5 s, 15-20 mW, Laserglow Technologies), beginning 2 s before and ending 2 s after cue delivery, in order to silence CR+LT signal transmission in the amygdala during sensory stimulation. Blocks of sensory stimulations overlapping with CR+LT axonal inhibition were alternating with stimulations without silencing.

In the case of B256 recordings with a single cue type, low-intensity optogenetic activations (5 ms, 1 mW) were repeated at 0.1 Hz for 3x10 minutes with 5-minute interblock intervals; 6x10 foot shock stimuli (100 ms, 1 mA) were delivered with 30 s interstimulus intervals and a few minutes interblock intervals. These recordings were done in the Oscillatory Neuronal Networks Research Group at the University of Szeged (group leader: Dr. Antal Berényi).

The lasers and the speaker as well as the current generator (Medicor or BioStim Bipolar Stimulus Isolator BSE-4x, Supertech Instruments or STG4008-1.6mA, Multi Channel Systems in the case of 256-channel recordings) were triggered by analog signals delivered with a National Instruments acquisition board (USB-6353). Analog trigger pulses were also delivered to the evaluation board and registered in parallel with neural data for synchronization purposes. All stimulation protocols were executed with my custom-written MATLAB (Mathworks) codes.

Mice with incorrect virus expression or foot shock artefacts which corrupted spike data were excluded from the analysis (n=3).

2.2.3.2. Chronic *in vivo* electrophysiology in freely moving mice during threat learning

During the behavioral protocol, the interface board was connected to the Intan RHD2000 recording system via an RHD2132 preamplifier (Intan Technologies; gain: 192V/V, sampling frequency: 20 kHz, frequency range: 0.1-7500 Hz). The optogenetic laser was driven by a National Instruments board (NI USB-6343) controlled by MATLAB. Analog trigger pulses were registered in parallel with the neural data.

Optogenetic taggings were performed in the home cage, before and/or after mice were placed in the behavioral apparatus. Photoactivation was skipped immediately after conditioning and before retrieval in order to avoid any interference with aversive memory processes. Optogenetic activation of CR+LT cells was done with 5 or 10 ms long, low-intensity laser pulses at 0.5 or 1 Hz (473 nm laser intensity was set to <1 mW for orthodromic and 5-6 mW for antidromic stimulations). In additional recordings (n=5 mice), the intensity of ortho- and antidromic photoactivation (10 and 50 ms with 1-10 s intervals) was kept below 5 mW. The lower laser intensity was chosen because of a higher response probability in awake mice as well as because of the closeness of the optic fiber to the recording electrodes and the recorded brain tissue itself. Higher laser intensities could obstruct the unequivocal clustering of single units recorded in freely moving conditions, or even potentially elicit long-term synaptic changes in the amygdala (Nabavi *et al.*, 2014).

Mice with inadequate virus expression, tetrode position or a failure in discriminative aversive learning were excluded from the analysis (n=18).

2.2.4. **Behavioral paradigms**

Chronically implanted mice were tested in a conditioning box (MKI Plexi). Auditory stimulations and 1 s long foot shocks (Ionflow Bipolar or BioStim Bipolar Stimulus Isolator BSE-4x, Supertech Instruments) were triggered by analog signals delivered with a NI USB-6343. All stimulation protocols were executed with my custom-built MATLAB codes.

In the discriminative aversive learning paradigm, auditory stimuli (75 dB) were composed of 30 s long continuous or 1 Hz pulse trains of 7.5 kHz sine wave (CS+) and Gaussian white noise (CS-). Mice underwent two habituation days (10xCS- delivered in context A with black dotted white walls), one conditioning (4 unpaired CS+ presentations followed by 10xCS+ terminated with a foot shock – US, 1 s, 1 mA – in context B with plain white walls) and one retrieval day (5xCS- followed by 5xCS+ in context A).

In a further set of experiments without cue discrimination, a day of habituation (with no sound playback in context A) was followed by one conditioning day (3, 10, 30 s continuous 7.5

kHz pure tones with foot shock at the end were delivered five times in context B). Stimuli (3x5xCS in context A) were then played back on three consecutive retrieval / extinction days.

The behavior of mice was captured on video at 30 frames per second (fps). Aversive mouse behavior was manually annotated and quantified by the time percentage of freezing with the H77 recorder software (Mikics *et al.*, 2005) (courtesy of Prof. Dr. József Haller, Institute of Experimental Medicine, Budapest, Hungary), or in the additional cases, with a custom-written locomotion analysis pipeline in Bonsai (Lopes *et al.*, 2015), created by Félix Jártó (RCNS). In the latter case, the immobility duration threshold for freezing was set to 1 s. Discrimination index (DI) was calculated from time percentages of freezing using the following equation:

$$DI = \frac{(freezing_{CS+} - freezing_{CS-})}{(freezing_{CS+} + freezing_{CS-})}$$

2.2.5. **Neural data processing**

Following noise filtering with average subtraction, raw electrophysiological recordings were filtered (>500 Hz) for spike detection. Spike detection and principal component analysis based automatic clustering were performed using SpikeDetekt and KlustaKwik, respectively (Rossant *et al.*, 2016). Cell grouping was refined manually with KlustaViewa. A group of spikes was considered to be generated by a single neuron if they formed a discrete, well-isolated cluster and had an autocorrelogram with a refractory period (average bin values of the first 2 ms did not reach the autocorrelogram's asymptote line, which represents the mean firing rate).

In the case of tetrode recordings, I excluded cells in case they shared a symmetric cross-correlogram and a similar spike waveform with units from different tetrodes in order to avoid enumerating the same cell more than once. Neuronal data from subsequent days were sorted together.

I carried out all further data analysis with custom-built MATLAB codes created by myself, incorporating functions built by Melinda Váncsodi, Félix Jártó and Dr. Péter Barthó (RCNS). All the presented spike data are derived from single units (clustered cells).

In the case of amygdala neurons, putative principal cells (PN; glutamatergic LA neurons and GABAergic medium spiny neurons in the AStr) and interneurons (IN) were distinguished by their mean action potential waveform (measured ±3 ms from the detected spike time). Based on previous neocortical data (Barthó *et al.*, 2004) and the bimodal distribution of amygdala spike-width, putative interneurons were selected by a trough-to-peak spike width (SW) equal to or less than 0.6 ms. With the additional criteria of half-amplitude spike width (HW) equal to or less than 0.3 ms, the category of broad-spiking neurons below a spike-width of 0.8 ms was refined (**Figure 2.2.5./a-b**). Clustering shown in (Barthó *et al.*, 2004) resulted in

DOI:10.15774/PPKE.ITK.2022.002

similar parameters. Spike-widths above 1.2 ms could also be measurement artefacts caused by superimposed spikes or evoked LFP responses, though they were categorized with principal neurons.

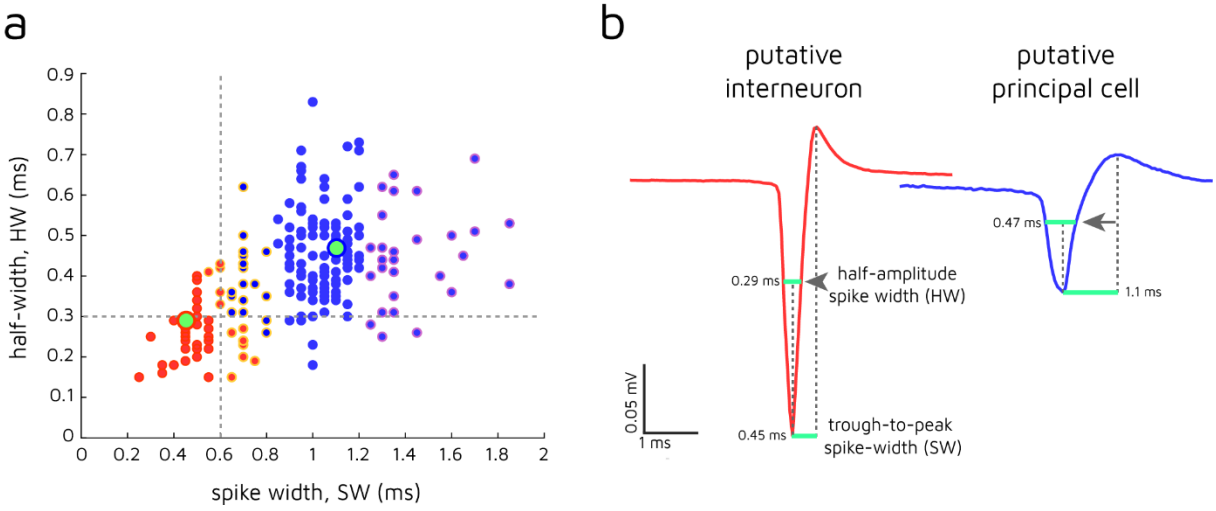

Figure 2.2.5. Categorization of amygdala neurons based on their spike waveform.

a/ The two grouping parameters were the trough-to-peak spike width (SW) and the half-amplitude spike width (HW), also depicted in **b**. k-means clustering of the mean action potential waveforms of sorted units (recorded with a B32 probe in the CR+LT axonal inhibition experiments, see later in **2.3.2.**) from the LA and AStr. The groups of narrow- (red dots) and broad-spiking (blue dots) units were in concordance with the pre-established criteria for putative interneurons with SW below 0.6 ms (vertical dashed gray line). Another cluster is transitional (orange circle), and it was regrouped according to the HW (horizontal dashed gray line). Spike-widths above 1.2 ms in the fourth group (violet circle) were categorized with principal neurons. Example units in **b** are highlighted with green dots. **b/** Two example units categorized as a putative interneuron and a principal cell based on their measured spike waveform parameters: the spike width (SW), calculated between the negative peak and the peak of the afterhyperpolarization, and the half-width (HW), which is the spike's width at half of its maximal amplitude.

Mean spontaneous firing rates were calculated from a 1- to 3-minute baseline period before any stimulation occurred.

Short-latency (≤10 ms) light-evoked spiking was considered reliable to indicate direct and monosynaptic somatic or axonal activation (Arenkiel *et al.*, 2007), thus, allowed the identification of the CR+LT and CR+LT-recipient amygdala cells. For disynaptic responses to collicular axonal stimulation, amygdala responses within the poststimulus 20 ms were considered significant. In the case of 5-10 ms light stimuli, activated neurons were determined upon a criterion of a z-scored, 1 ms binned spike rate above 3.3 (p>0.001) in the first 10 ms after light onset.

Auditory and foot shock response latencies were estimated from the first bin value which exceeded 3 in the z-scored peristimulus time histogram (PSTH), given in 2.5 or 5 ms units. Latency distributions showed (see also later in **Figure 2.3.1.2./b**, **2.3.1.3./d** and **2.3.2.1./d**) that

the majority of LT and amygdala cells responded to sensory stimuli within 50 ms (see also (Quirk *et al.*, 1995)), which served as a basis for the choice of the analysis windows.

Significant evoked responses to auditory and foot shock stimuli were defined for each sorted cell as follows. A Poisson-distribution based confidence interval (p<0.05) was set for a 1 s long baseline before stimulations. If the mean of early (<50 ms) and late (<500 ms) poststimulus spike count distribution exceeded this interval, and the signal-to-noise ratio (SNR) was more than ~0.5 in the case of short-latency responses, cells were considered responsive. SNR was calculated from the reciprocal of the coefficient of variation, the ratio of mean to standard deviation (μ/σ) of the 5 ms binned PSTH in the respective interval. As a relatively small number of pain-inducing stimuli were delivered, quantifying the dispersion of poststimulus firing helped to avoid enumerating false evoked responses detected upon a sparse activity. In the case of longer (50-200 ms) optogenetic stimulations, the latter method was used for the first 10 and 20 ms after light delivery.

Enhancement in early (<50 ms) and late (<500 ms) multimodal responses was defined as the increase in the average tone + foot shock-evoked firing rate expressed in percentage of the summed unimodal evoked firing rates. Cases where no unimodal response was present, but multisensory stimulation evoked significant changes in the firing rate, were also considered enhanced/augmented activities. Firing rate modulation in tetrode unit data was calculated from the difference between the average firing rate (in Hz) over the total sound duration and the 10 s baseline period. Time bins with the foot shock were not included.

Representative population firing rate vectors were calculated from 5 ms binned ([-1 1.5] s peristimulus) spiking activity of a neuronal population from neighboring probe shanks placed in the same thalamic or amygdala region, where the number of sorted units exceeded 15. The activity of the population in a particular time bin was represented as a point in a multidimensional space where each dimension corresponds to the firing rate of a particular unit considered. Principal component analysis (PCA) of the population vector included the baseline period. Projections were computed from the top three eigenvectors of the vector's covariance matrix.

Peak latency calculation of cue-evoked local-field potential (LFP) responses in 256-channel recordings was done on baseline corrected and averaged broadband (raw) signals within the first 50 ms after stimulation. For current source density (CSD) analysis, the inverse estimation method (Pettersen *et al.*, 2006) was applied on a baseline corrected and averaged broadband trace in a [-10 50] ms time window around stimuli. To this end, I used the source codes of a MATLAB interface developed by (Łęski *et al.*, 2011) for two-dimensional probe configurations. I calculated the CSD in 1 ms intervals. Spline spatial interpolation and 'doubled' (D) boundary interpolation were done on the selected grid segment. I chose a small value (h=0.05 mm) for

the estimated extent of neural activity perpendicular to the probe grid in order to minimize spatial noise; I assumed that the CSD across the small nuclei and numerous internuclear boundaries in the amygdala can be heterogeneous even in this short distance.

2.2.6. **Immunohistochemistry**

2.2.6.1. Fluorescent microscopy

In order to amplify virally expressed fluorophore signals (eYFP), fluorescent immunohistochemistry was performed.

After sectioning, free-floating brain slices were intensively washed 5 times with 0.1 M PB. All antibodies were diluted in 0.1 M PB. For high-quality fluorescent labeling, sections were treated with a blocking solution containing 10% normal donkey serum (NDS, Abcam) and 0.5 % Triton-X (Sigma-Aldrich) in 0.1 M PB, for 30 minutes at room temperature (RT). In the case of DiI-stained brains, in order to avoid the diminishing of the stain, slices were instead incubated in 30% sucrose for 2 hours at RT, then freeze-thawed four times over liquid nitrogen. Then, sections were incubated in primary antibody solution at RT overnight or for 2-3 days at 4°C.

Following primary antibody incubation, sections were exposed to secondary fluorescent antibodies for 2 hours at RT. When necessary, staining was enhanced after primary and before secondary antibody incubation with biotinylated antibodies (see detailed procedures in **Table 2.**). All fluorescent slices were mounted in Vectashield (Vector Laboratories). Stained sections were studied with confocal microscopy (Zeiss).

2.2.6.2. Electron microscopy

After incubation in 30% sucrose and freeze-thawing, combined immunogold-immunoperoxidase double immunostaining was performed to visualize the synaptic contacts formed by the collicular inputs on CR+LT neurons (n=3-3 mice). Areas of interest were re-embedded and sectioned to ultrathin (60 nm) serial sections for electron microscopy, which were collected on Formvar-coated single slot grids (see detailed procedures in **Table 2.**).

DAB-labeled excitatory axon terminals originating from the SC and IC were identified by asymmetric synapses formed on immunogold-labeled CR+ postsynaptic elements.

DOI:10.15774/PPKE.ITK.2022.002

2.2.7. **Statistical analysis**

The number of analyzed cells is shown with N, while n represents the number of animals. Data from independent experiments were pooled when possible. Statistical significance was assessed using two-tailed *t*-test or Mann–Whitney–Wilcoxon-test, based on the normality level and sample size of the dataset, as well as ANOVA. Normality was tested with the Kolmogorov-Smirnov test. χ^2 tests were applied to compare the ratios of responsive LT and amygdala cells. Statistical analysis was performed using MATLAB or STATISTICA 13 (StatSoft) (see **Table 3.** for details). Significance levels are indicated as follows: #0.05<p<0.1; *p<0.05; **p<0.01; ***p<0.001; ****p<0.0001; n.s., not significant.

DOI:10.15774/PPKE.ITK.2022.002

2.3. Results

Our group cell-specifically classified the LA-projecting thalamic neurons with retrograde labelling technique (cholera toxin B subunit (CTB) injection, (Barsy & Kocsis *et al.*, 2020)): they are principally located in the vicinity of the primary auditory thalamus (MGN), in the PIL and the SG (**Figure 2.3./a**). A few retrogradely labeled cells were also found in the transition zone (MGM) linking the dorsal and ventral clusters.

Calretinin-positive (CR+) neurons are particularly abundant (~80%) in these lateral thalamic regions, and the majority (~94%) of LA-projecting cells express this protein (**Figure 2.3./b**). This infers that the thalamo-LA pathway largely roots from the CR+ PIL region, also referred to in the literature as PIN, PIT, PoT, and SPFp (Campeau & Davis, 1995; Quirk *et al.*, 1997; Gauriau & Bernard, 2004; Han *et al.*, 2008; Weinberger, 2011; Lipshetz *et al.*, 2018), as well as from the CR+ SG population. Hereafter, I collectively refer to them as CR+ lateral thalamic (CR+LT) ensemble, since their collicular input (see later in **Figure 2.3.3.1.**) and cortical/amygdala output innervation are proven to be similar (Barsy & Kocsis *et al.*, 2020).

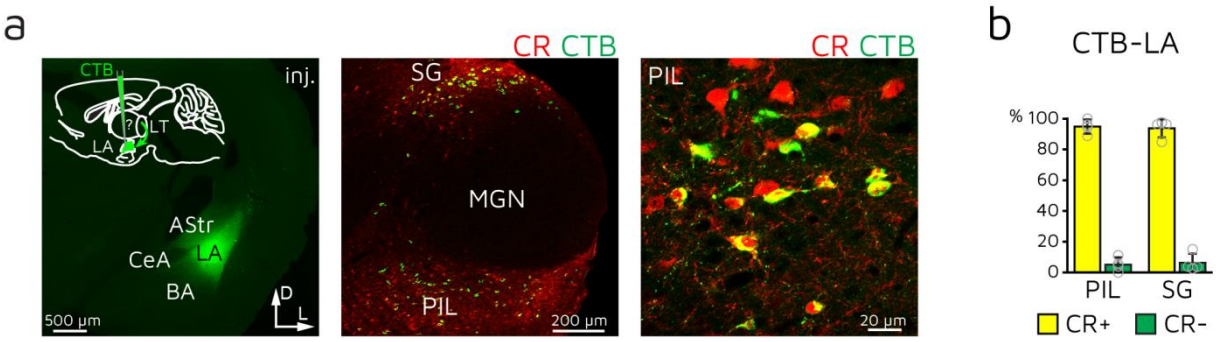

Figure 2.3. The vast majority of LA-projecting lateral thalamic cells express calretinin.

a/ Retrograde tracer CTB (green) injection site in the LA. *Inset*, experimental design. Arrows indicate the dorsal (D) and the lateral (L) orientation of the coronal brain section. Labelled LA-projecting cells (CTB-LA) are predominantly present in the calretinin-labeled (CR, red) PIL and SG. **b/** Majority of CTB-LA cells are CR+ both in the PIL and the SG (n=4 mice).

Published in (Barsy & Kocsis et al., 2020) Figure 1./a-d.

This term was chosen for a pragmatic reason. The amygdaloid complex receives most of its thalamic afferents from two CR+ thalamic cell groups. One of them is located medially, including the paraventricular, intermediodorsal, centromedial and intralaminar nuclei which preferentially project to the basolateral and centrolateral amygdala, and rather contribute to arousal-mediated processes (Mátyás *et al.*, 2018). The other one is built-up by the above-described clusters of neurons, laterally and caudally to the medial CR+ group.

I hereby probed the strength of calretinin as a marker to functionally dissect the direct lateral thalamo-amygdala route in threat-related (aversive) sensory processes.

DOI:10.15774/PPKE.ITK.2022.002

2.3.1. **Question IIa: Do CR+ lateral thalamic neurons encode and discriminate the sensory cues necessary for associative aversive cue learning?**

I performed extracellular electrophysiological recordings in anesthetized mice in order to reveal whether CR+LT can encode and possibly integrate neutral and innately aversive sensory cues and target the amygdala with salient cues within a short (<20 ms) time window.

To this end, I injected Channelrhodopsin-2 (ChR2) expressing adeno-associated viral construct (AAV-DIO-ChR2-eYFP) into the thalamus or the amygdala of Calb2(CR)-Cre mice (n=10) (**Figure 2.3.1.1./a**), which allowed me to study the cue-responses of orthodromically tagged and antidromically activated amygdala-projecting (CR+LT→AMY) CR+LT cells (**Figure 2.3.1.1./b-d**). Population data were divided into a ventral (PIL, from 3000-3200 µm) and dorsal (SG, from 2500-2700 µm) group. The PIL cohort includes units from the MGM.

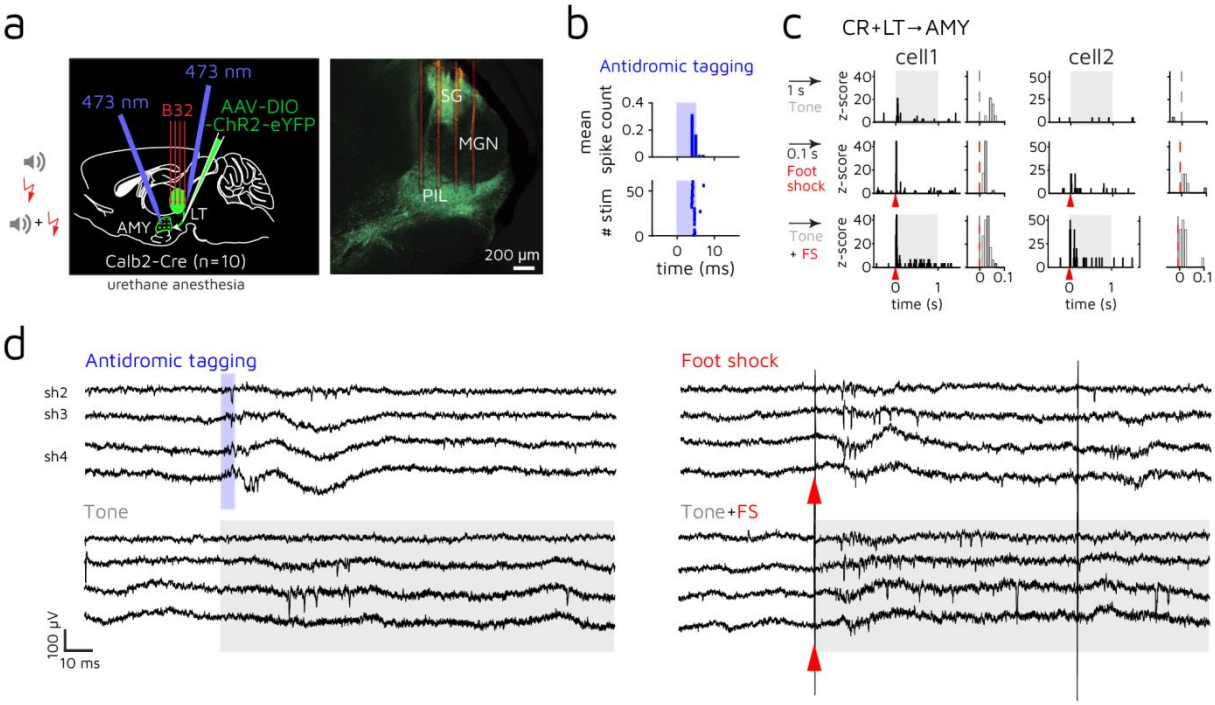

Figure 2.3.1.1. Study of lateral thalamic (LT) processing of neutral and aversive cues in urethane-anesthetized mice.

a/ Left: scheme for acute *in vivo* electrophysiological recordings from LT cells (n=10 mice) with delivery of tone, foot shock and joint tone + foot shock signals as well as of ortho- and antidromic optogenetic stimuli for identification purposes. Right: a coronal section with AAV-DIO-ChR2-eYFP-transduced CR+ cells (green) and the trace of the four-shank Buzsáki32 probe (B32, red). **b/** Antidromic optogenetic tagging (blue shade) of a CR+LT→AMY cell. Bin size of the PSTH is 1 ms. **c/** A CR+LT→AMY unit (cell 1) showing short-latency tone (gray shade), foot shock (FS; red arrowhead) and enhanced paired tone + foot shock activation. Another CR+LT→AMY unit (cell 2) with enhanced tone + foot shock activation without single tone response. Right: zoom-in of the traces on the left. Bin size is 10 ms. **d/** Broadband extracellular traces from the PIL showing short-latency activation to antidromic optogenetic tagging, tone, foot shock (note brief electric artefacts), and paired tone + shock stimulation.

Panels a-c published in (Barsy & Kocsis et al., 2020) Figure 2./a-c.

LT neurons showed both early (<50 ms) and late (50-500 ms) activations to tone (7.5 kHz pure tone), electric foot shock (FS) and/or tone + foot shock signals, indicating direct subcortical as well as broader network involving sensory effects, respectively (**Figure 2.3.1.2./a**). Most short-latency sensory responses started in the 10-30 ms poststimulus time window (**Figure 2.3.1.2./b,** see also median latencies in **Table 3.**).

Foot shock (FS) and foot shock-paired tone stimuli activated more LT cells than tone alone, consistently with fiber photometry data in (Taylor *et al.*, 2021) acquired during aversive conditioning. Short-latency (<50 ms) nociceptive cue (FS) responses were primarily characteristic to the CR+ PIL populations, which is in concordance with literature showing pain-evoked activity in this region (Bordi & LeDoux, 1994*b*; Lipshetz *et al.*, 2018). Overall, a higher proportion of CR+ PIL neurons were receptive to foot shock and associative stimuli than CR-negative cells.

However, SG units showed late aversive activation (50-500 ms) in a higher proportion, with no significant difference between the antidromically tagged CR+ and the non-tagged cohort. This can possibly be attributed to their rather visual (Hicks *et al.*, 1986; Linke *et al.*, 1999) than nociceptive processing features (**Figure 2.3.1.2./a**). In addition, c-Fos data in (Barsy & Kocsis *et al.*, 2020) showed that aversive cue delivery or association did not drive significant increase in SG activity compared to neutral cue delivery, which may be attributed to a different evoked firing mechanism at the population level.

Only a relatively few (N=5) sensory evoked inhibitory responses were found in the LT. This might be partially attributed to the low baseline firing rates of PIL and SG neurons (1.33 and 0.60 Hz on average, respectively) in urethane anesthesia, which compromises the detection of short-term decreases in spiking activity.

As the predominance of short-latency nociceptive responses were equally characteristic to the CR+ PIL and the amygdala-projecting (antidromically activated) CR+ PIL units, I further studied their overall part in associative sensory processing. Aversive uni- and multimodal response latencies of the CR+ PIL were shorter than the ones evoked by single tone presentations. Moreover, paired signals drove the strongest short-latency activation (~17 ms on average, **Figure 2.3.1.2./c-d**) in this population. Multisensory enhancement was also present in the majority of CR+ PIL cells, resulting in a larger short-latency activation to foot shock-coupled tone stimuli at the population level compared to unimodal tone or foot shock cues (**Figure 2.3.1.2./d-e**). The majority (83%) of the enhanced cells did not show a unimodal response to tone, suggesting that auditory stimulation may evoke subthreshold activation in CR+ neurons. Yet it could further potentiate foot shock signaling in these cells.

DOI:10.15774/PPKE.ITK.2022.002

These data provide evidence that association of tone and foot shock can take place at the level of the thalamus, prior to the amygdala, and this feature can be captured by studying the CR+ PIL population.

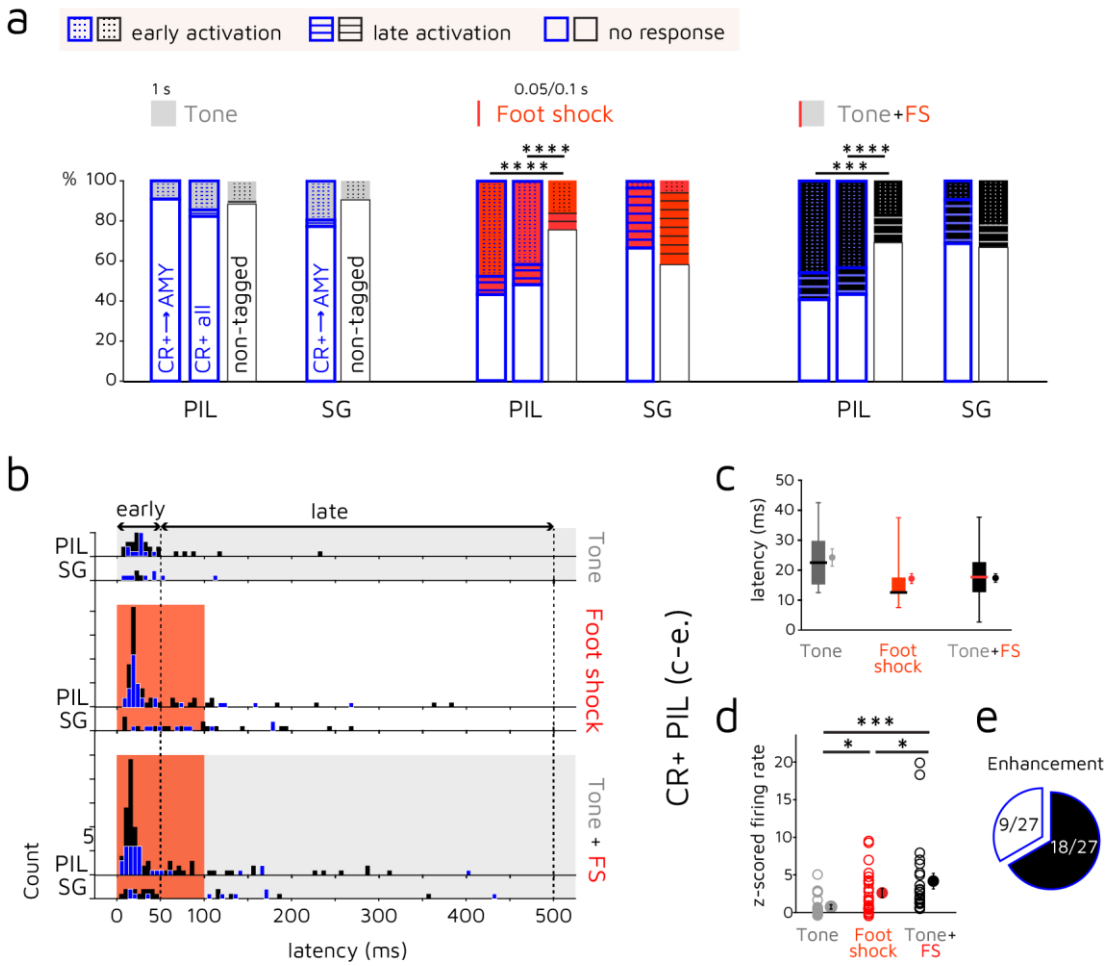

Figure 2.3.1.2. Selective and fast aversive sensory signaling by the CR+LT.

a/ Graphs showing the proportions of short-latency (<50 ms; dotted area) and long-latency (50-500 ms; striped area) tone- (gray), foot shock- (FS; red) and paired tone + foot shock-evoked (black) responses within the CR+LT→AMY, the total CR+LT (blue framed boxes) and the non-tagged LT cell populations (black framed boxes), all divided into PIL and SG units. Note that the CR+ PIL unit responses are mostly short-latency (<50 ms). *χ^2 test*. **b/** Histograms depicting the distribution of sensory response latencies calculated for PIL and SG cells separately; latencies of CR+ units are shown with blue bars. Note that the majority of early evoked activity takes place in the 10-30 ms time window after cue delivery (see also in **c**). Bin size is 5 ms. **c/** Boxplots showing the estimated latencies of early sensory activations in the CR+ PIL cells within a 50 ms poststimulus time window. Filled circles represent the mean ± SEM. **d/** Average z-scores of short-latency (<50 ms) unit firing rates upon sensory stimulations in the case of CR+ PIL neurons with short-latency associated responses (N = 27 cells). Mean ± SEM. *Friedman's ANOVA with Wilcoxon signed-rank test (two-sided)*. **e/** Proportion of multisensory enhancement (augmented tone + foot shock signaling) among the CR+ PIL cells in **d**.

Panels a, c-e published in (Barsy & Kocsis et al., 2020) Figure 2./d-g, data supplemented with two recording sites in SG/MGN from the same animals, and divided into PIL and SG.

DOI:10.15774/PPKE.ITK.2022.002

In the first set of experiments, only onset responses were studied. Offset responses to short (50-100 ms) aversive stimuli could interfere with longer latency evoked activities. Nevertheless, 'OFF' responses were selectively reported in the non-lemniscal MGN (e.g., in the MGM) of the guinea pig, which have long-duration selectivity (He, 2002; Yu *et al.*, 2004), showing increased offset responsivity to longer sound durations. Furthermore, cues used in conditioning (both US and CS) are usually an order of magnitude longer.

Here, in a complementary set of data from Calb2-Cre animals (n=6 mice) with AAV-DIO-ChR2-eYFP-transduced LT, I studied evoked LT responses to the sensory cues (30 s tone ending with 1 s foot shock) given in our associative behavioral paradigms (Barsy & Kocsis *et al.*, 2020), as well as to orthodromic optogenetic activation (**Figure 2.3.1.3./a-b**). Besides onset (ON) activities, aversive (FS and tone+FS) offset (OFF) response properties were examined to detect potential changes in evoked firing when the two sensory cues are overlapped.

In concordance with the previous dataset, LT neurons were significantly more driven by aversive stimuli than by unimodal acoustic stimulation. In this stimulation protocol, too, CR+ PIL neurons showed ON and OFF activation to single or tone-paired aversive cues in a significantly larger proportion than the non-tagged PIL population, with mainly early activation. With no significant difference between the tagged and non-tagged cohort, responses were again predominantly late in the dorsal (SG) population (**Figure 2.3.1.3./c**).

Short-latency activations typically started within the first 10-30 ms (**Figure 2.3.1.3./d**, see also median latencies in **Table 3.**), which is in concordance with my previous results shown in **Figure 2.3.1.2./b-c**. The phasic character and the activation restricted to cue delivery exclude that a change in general arousal level elicits the early nociceptive CR+ PIL responses (**Figure 2.3.1.3./e**). Their short-latency ON and OFF activation also exhibited multisensory enhancement in the majority of the recorded cells (**Figure 2.3.1.3./e-g**). This further indicates that tone stimulation, even long after cue onset when activations are less prominent or even subthreshold, can enhance aversive neuronal responses.

Altogether, these data further suggest that PIL neurons are more involved in fast nociceptive cue processing, marking the beginning and the end of innately aversive stimuli, and enhancing their activity when these cues co-occur with a neutral sound. These associated activations can then be conveyed to the amygdala in less than 20 ms, which is necessary to elicit fast responses to threats in awake behaving animals.

DOI:10.15774/PPKE.ITK.2022.002

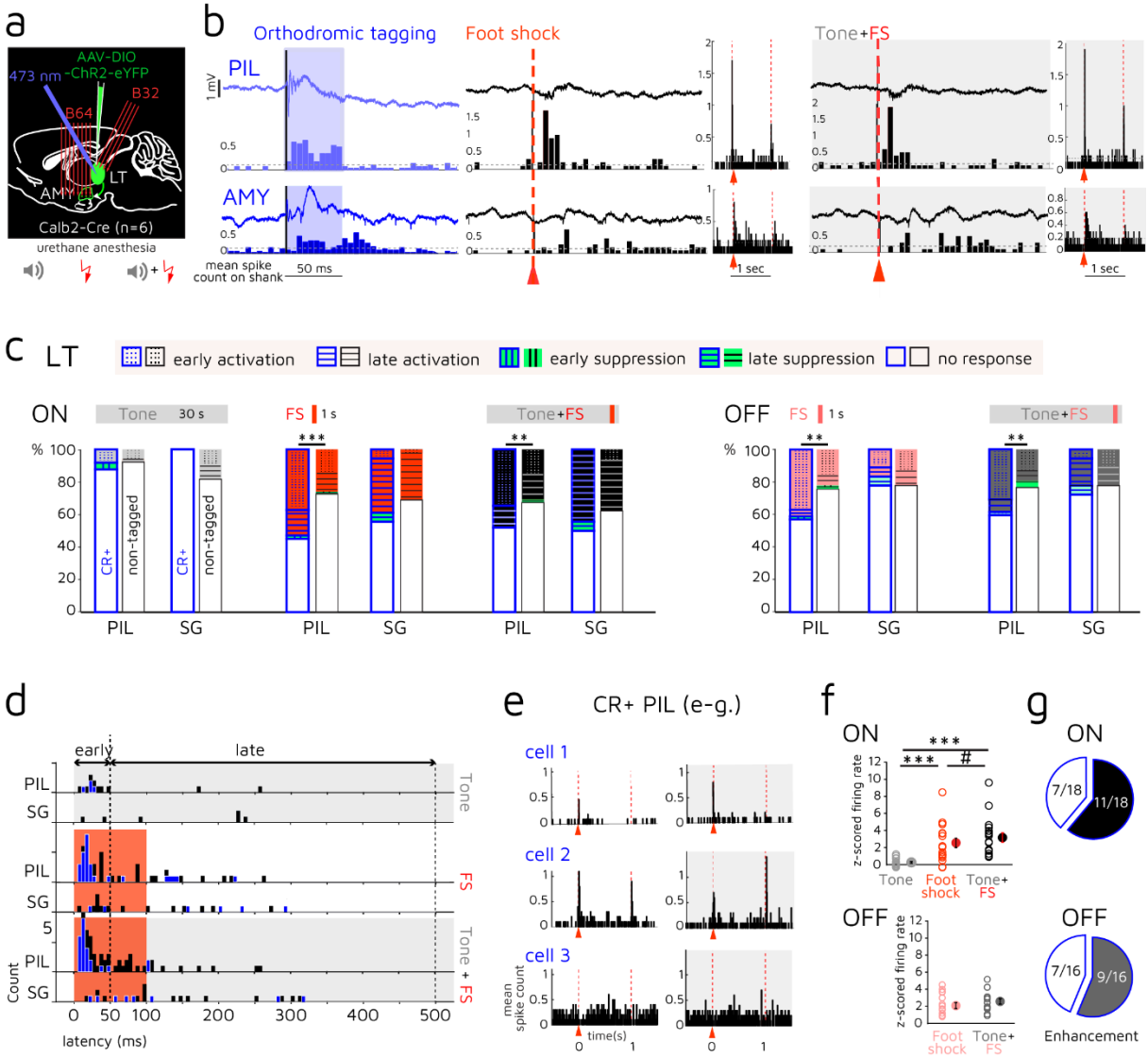

Figure 2.3.1.3. Aversive conditioning related sensory processes in the CR+LT.

a*/* Scheme for acute *in vivo* electrophysiological recordings with tone, foot shock and associated sensory stimulations alongside orthodromic CR+LT phototagging. Neural data were acquired from the LT (n=6 mice) with a 4-shank Buzsáki32 probe, in one case with an E128 probe. In 4 animals, recordings were done in parallel in the amygdala with an 8-shank Buzsáki64 probe. **b***/* Two sets of broadband signal epochs (upper trace) from an electrode channel located in the PIL and the amygdala (AMY) with sorted units (bottom PSTH) from the respective probe shank. The shown evoked onset activities were acquired upon foot shock (FS; red arrowhead and dashed line) and tone-coupled foot shock delivery. Insets show the entire length of the aversive cue responses. Note the early transient firing rate elevations and the enhancement of associated cue responses in both the PIL and the AMY. Bin size is 5 ms. Gray horizontal dashed line indicates 2 SD above the mean baseline spike rate. **c***/* Graphs showing the proportions of short- (dotted or vertically striped areas) and long-latency (horizontally striped area) onset (ON) and offset (OFF) sensory responses within the orthodomically tagged CR+LT (blue framed boxes) and non-tagged LT (black framed boxes) populations divided into PIL and SG. χ^2 *test*. **d***/* Histograms depicting the distribution of onset sensory latencies calculated for PIL and SG cells separately. The latencies of CR+ units are shown with blue bars. Bin size is 5 ms. **e***/* Aversive responses of three CR+ PIL cells showing enhancement of ON (cell 1), OFF (cell 2) activation as well as a release from suppression (cell 3) upon the associated cue. Bin size is 5 ms. **f***/* Average z-scores of short-latency (<50 ms) unit firing rates upon sensory stimulations in the case of CR+ PIL neurons with short-latency ON (up) and OFF (bottom) associated responses (N = 18 and 16 cells, respectively). Mean ± SEM. *Friedman's ANOVA with Wilcoxon signed-rank test (two-sided).* **g***/* Proportion of multisensory enhancement among the CR+ PIL cells in **f**.

In 4 out of 6 mice with LT recordings and long sensory stimulations (**Figure 2.3.1.3.**), I recorded from the amygdala in parallel, in order to study whether the hallmark aversive activation is also present in the CR+LT-recipient cells (**Figure 2.3.1.4./a**, see also later in **Figure 2.3.3.3.**). Amongst LT target regions, single units from only the lateral amygdala (LA) and amygdalostriatal transition area (AStr) were included since the central amygdala has been shown to receive nociceptive information from the parabrachial nucleus (Han *et al.*, 2015). Furthermore, it is not considered the first site of aversive associative memory processes but rather an executive output region of the amygdala (Fadok *et al.*, 2018). I conducted all further analyses (see section **2.3.2.**) with this consideration in mind.

Amygdala neurons were also more responsive to aversive cues than to sole auditory stimulation, with a less apparent and non-significant difference in non-recipient cells. CR+LT-target (mostly narrow-spiking) cells exhibited a higher proportion of aversive activation than non-recipient cells, which was significant in the case of OFF responses (**Figure 2.3.1.4./b-c**).

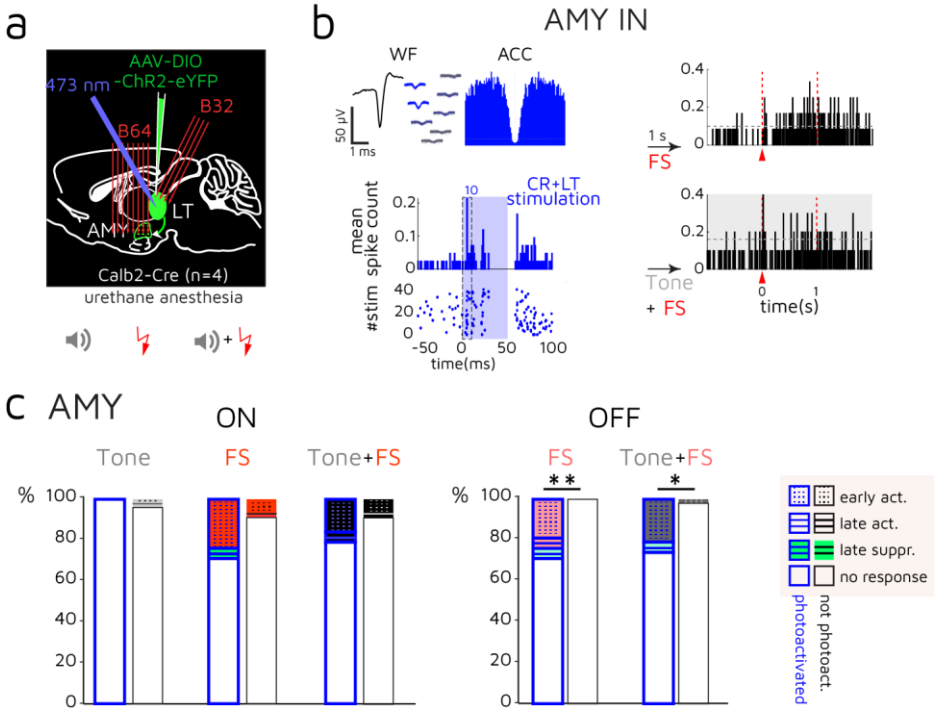

Figure 2.3.1.4. Aversive conditioning related sensory processes in the CR+LT target amygdala regions.

a/ Scheme for acute *in vivo* electrophysiological recordings (n=4 mice) with tone (gray), foot shock (FS; red arrowhead) and paired stimulations alongside somatic CR+LT optogenetic activation. Neural data were collected from the amygdala with an 8-shank Buzsáki64 probe in parallel with thalamic recordings shown in **Figure 2.3.1.3. b/** Optogenetic activation (left, blue trace, 1 ms bin size) as well as aversive shock and associated tone+shock responses (right, 5 ms bin size) of a CR+LT-recipient putative interneuron (see mean narrow spike waveform and characteristic autocorrelogram (Barthó *et al.*, 2004)) showing multisensory enhancement in its onset responsivity. Gray horizontal dashed line indicates 2 SD above the mean baseline spike rate. **c/** Graphs showing the proportions of short-latency (dotted area) and long-latency (horizontally striped area) onset (ON) and offset (OFF) sensory responses within the orthodomically activated CR+LT-recipient (blue framed boxes) and non-recipient (black framed boxes) cell populations. χ^2 *test*.

DOI:10.15774/PPKE.ITK.2022.002

These supplementary data also indicate that CR+LT neurons can target the lateral region of the amygdala with specifically short-latency aversive cues. In a set of experiments with freely moving mice, I studied whether the amygdala-connected CR+LT population can change its activity as a neutral acoustic signal becomes aversive through learning.

Thalamic cells spatially matching the CR+LT neurons have been shown to go through plasticity as a result of aversive conditioning (Han *et al.*, 2008; Weinberger, 2011). To clarify whether CR+LT cells show experience-dependent activity throughout aversive learning, I acquired extracellular electrophysiological data with tetrode implants in AAV-DIO-ChR2-eYFP injected Calb2-Cre mice (n=10) throughout a three-day long associative fear learning paradigm (**Figure 2.3.1.5./a-c**). CR+LT→AMY cells (N=18) were optogenetically identified (**Figure 2.3.1.5./d**), and their evoked responses to auditory stimuli (CS+: 7.5 kHz pure tone, CS-: Gaussian white noise) were monitored before aversive conditioning and during cued memory retrieval (**Figure 2.3.1.6./a-b**).

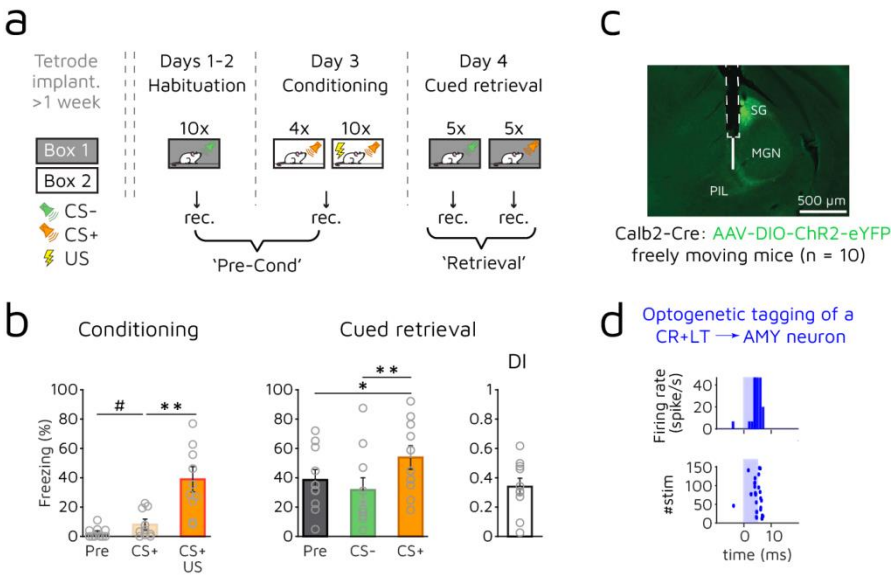

Figure 2.3.1.5. Study of CR+LT unit activity throughout discriminative aversive learning.

a/ Experimental design for tetrode recordings (rec.) of CR+LT→AMY neuronal activity in freely moving mice (n=10 mice) during discriminative aversive auditory conditioning (days 2–4). **b/** Freezing behavior during conditioning (left) and cued fear retrieval (middle) as well as discrimination indices (DI, right) are shown. Note the significant increase in CS+-elicited aversive behavior during and after conditioning, as well as the discrimination between the CS+ and CS- in cued fear retrieval. Mean ± SEM. *Friedman's ANOVA with Wilcoxon signed-rank test (two-sided).* **c/** A coronal section showing retrogradely labeled CR+LT→AMY cells (green) and the location of the ensemble of optic fiber and tetrodes (white scheme). **d/** Optogenetic tagging (blue) of a CR+PIL→AMY cell, also shown as Cell 1 in **Figure 2.3.1.6./a-b**. Bin size is 1 ms.

Panels a and c published in Figure 7./g-h, panels b and d in Supplementary Figure 8./a-c in (Barsy & Kocsis et al., 2020).

DOI:10.15774/PPKE.ITK.2022.002

At the population level, activity of 9/18 thalamic cells showed short-latency (<50 ms) modulation in parallel with the formation of the aversive memory (**Figure 2.3.1.6./c**). Threat learning recruited CR+LT→AMY neurons to respond to CS+ (before conditioning, Pre-Cond CS+, N=1 cell vs. after conditioning, Retr CS+, N=5 cells). In addition, 6 out of 18 cells showed 'discriminative' onset short-latency firing modulation during cued retrieval. This indicates that the CR+LT→AMY pathway can transfer associated signals in behaving animals, and its activity can change as an auditory cue becomes aversive.

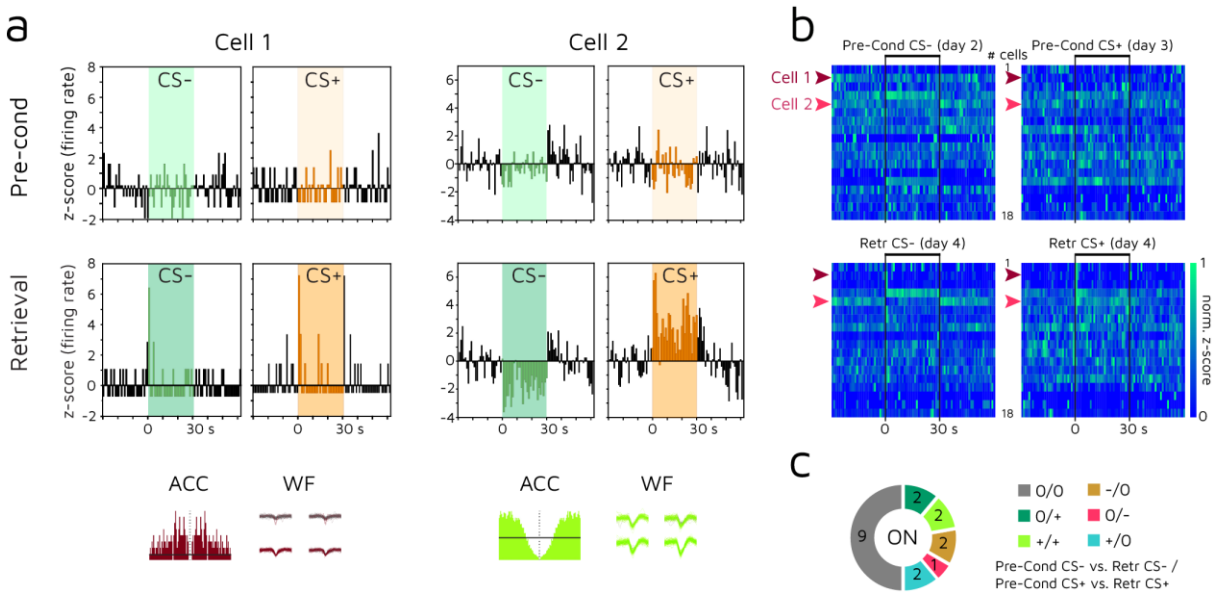

Figure 2.3.1.6. Discriminative auditory aversive learning induces changes in the activity pattern of CR+LT cells.

a/ Auditory evoked activities (CS-: green, CS+ orange shaded areas) of two CR+LT→AMY cells in the following experimental sessions: before conditioning (Pre-Cond) and during cued fear retrieval (Retr). Note the elevated onset (cell 1 and cell 2) and offset (cell 1) responses to CS+ upon threat learning. Autocorrelograms (ACC; left) and waveforms (WF; right) of the units from the respective tetrode channels are shown below. Horizontal line on the ACC indicates the asymptote line, vertical dotted line shows the center. Bin size is 1 s. **b/** Mean z-scored and normalized CR+LT→AMY unit activity changes (N = 18 cells from 6 mice) across the 3-day-long experiment. The order of neurons is identical across the four trials, and it was determined by the earliest response to Retrieval CS+. Arrowheads indicate the activity of the example cells in **a**. Bin size is 1 s. **c/** Population data for changes in early (<50 ms) poststimulus onset (ON) activities of the recorded CR+LT→AMY cells upon threat learning. Numbers within the charts indicate the number of cells showing a given change in response to CS-/CS+.

Panels a-b published in Figure 7./j-l, panels a and c in Supplementary Figure 8./d-f in (Barsy & Kocsis et al., 2020).

In an additional set of experiments (n=5 Calb2-Cre mice with AAV-DIO-ChR2-eYFP-transduced LT), I studied the response properties of CR+LT and CR+LT-recipient amygdala cells in non-discriminative threat conditioning (**Figure 2.3.1.7./a**). 7.5 kHz sine waves served as CS with varying (3, 10 and 30 s) lengths, which was aimed to gradually extend threat

DOI:10.15774/PPKE.ITK.2022.002

anticipation after cue onset due to the alternating timing of the foot shock at the end of the sounds. Repeated presentation of the CSs resulted in a decrease in cue-evoked freezing behavior indicating the extinction (Retr3) of a previously formed threat memory (**Figure 2.3.1.7./b**). During aversive conditioning and several cued memory retrievals on three consecutive days, I monitored sound-evoked LT and amygdala unit activity besides ortho- and antidromic optogenetic identification (**Figure 2.3.1.7./c-d** and **Figure 2.3.1.8./a, e**), in order to examine activity modulations driven by fear memory formation and extinction.

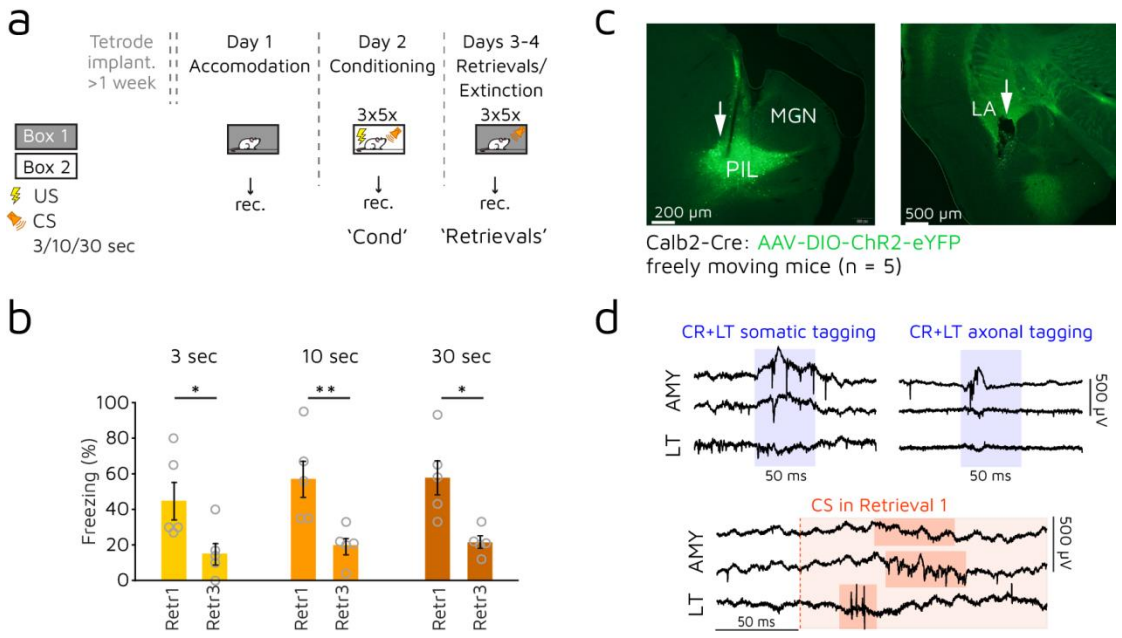

Figure 2.3.1.7. Additional study of CR+ PIL and CR+LT-recipient amygdala unit activity throughout aversive learning.

a/ Experimental design for tetrode recordings (rec.) of CR+LT and CR+LT-recipient amygdala neuronal activity in freely moving mice (n=5) throughout aversive learning (days 2–4). **b/** Freezing behavior of all mice in the first and last cued fear retrieval (Retr1 and Retr3) is shown for each (3, 10, 30 s long) stimulus. Mean ± SEM. *One-way repeated measures ANOVA with post hoc Fisher's LSD.* **c/** Two coronal brain sections from the AAV-DIO-ChR2-eYFP-transduced LT and amygdala showing anterogradely labeled CR+LT cells and axons (green), respectively, as well as the locations of the optic fiber coupled tetrodes (white arrows). **d/** Broadband extracellular neural traces from representative tetrode channels in the thalamus (LT) and the amygdala (AMY) of the same animal, showing CR+ somatic and axonal optogenetic activation (blue shade) as well as unit responses to the conditioned sound (CS, orange shade).

Heterogeneous sustained activities in the CR+LT exhibited experience-dependency (**Figure 2.3.1.8./b-d**), and at the population level (N=16 cells in 4 mice), showed the highest full-length firing elevation to the longest CS in conditioning (**Figure 2.3.1.8./c**). Simultaneous occurrence of CS-induced enhancement and suppression of neuronal activity in the CR+LT (**Figure 2.3.1.8./c-d**) can be due to the interplay of excitatory and inhibitory midbrain inputs (see later in **Figure 2.3.3.1.**).

DOI:10.15774/PPKE.ITK.2022.002

Population-level facilitation upon the entire CSs was the highest in threat conditioning among CR+LT-recipient amygdala neurons (**Figure 2.3.1.8./f-h**), 75% of which (N=12/16 units in 3 mice) had narrow spike width.

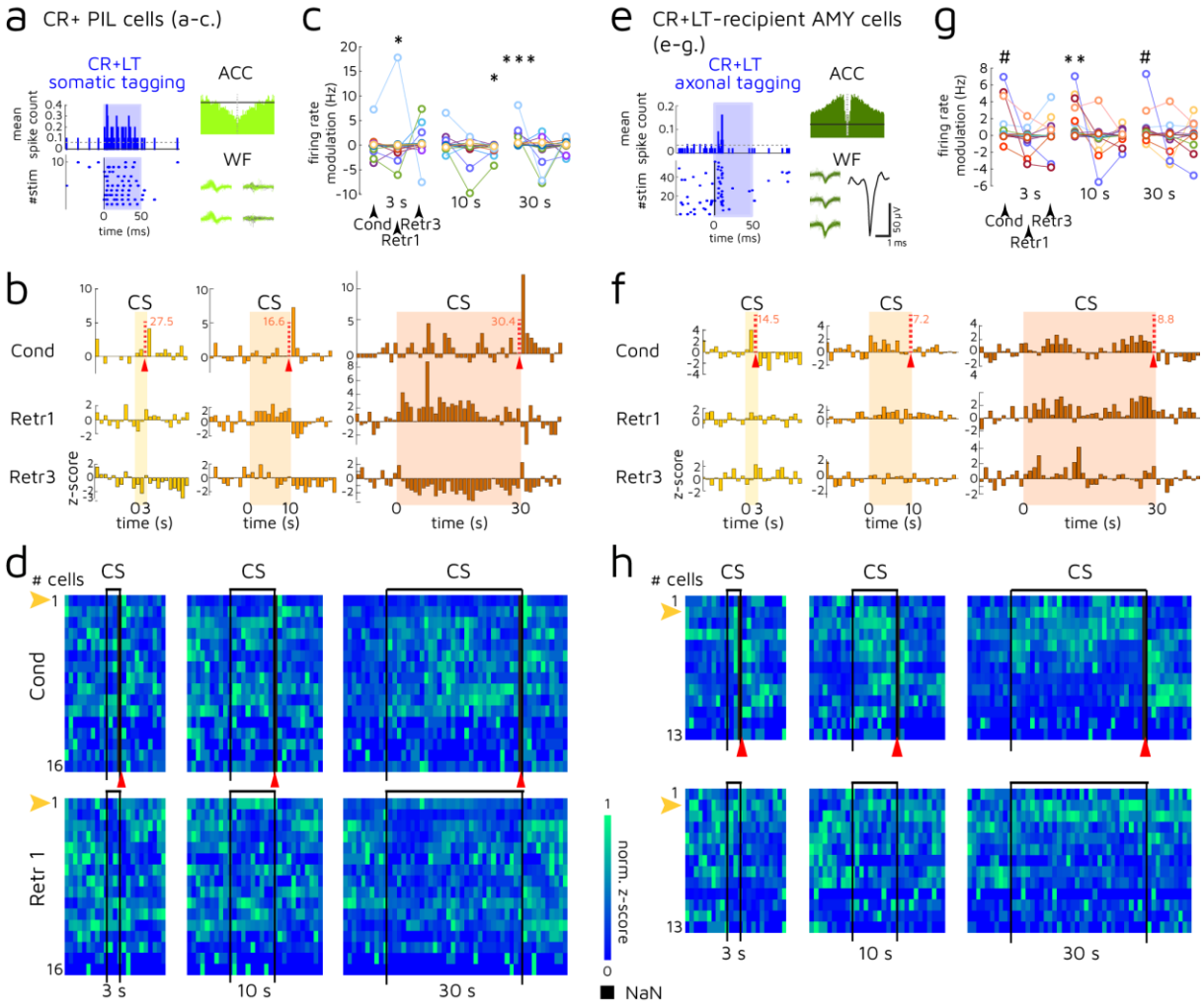

Figure 2.3.1.8. Activity changes in CR+ PIL and CR+LT-recipient amygdala cells upon the delivery of associated aversive auditory cues on subsequent days.

a/ Somatic optogenetic tagging (blue shade, 1 ms bin size) of a CR+LT neuron (left) with its autocorrelogram (ACC) and raw waveforms (WF) from the four respective tetrode channels (right). Horizontal line on the ACC corresponds to the asymptote, vertical dotted line shows the center. **b/** Mean z-scored spiking activity changes of the same CR+LT unit evoked by the different CS presentations (orange shaded areas, 1 s bin size) in three experimental sessions: during conditioning (Cond) as well as during early and late cued fear retrievals (Retr). z-score was calculated with a 10 s baseline in each case. Number beside the red dashed line indicates the z-score value in the time bin of the foot shock. **c/** Mean CR+LT (N=16 cells from 4 mice) firing rate modulation from 10 s baseline activity over the total length of the CSs, shown in neurons across the three days highlighted in **b**. *Wilcoxon signed-rank test (two-sided).* **d/** Mean z-scored (10 s baseline) and normalized CR+LT unit activity changes (from cells with calculable z-scores) during the different CSs delivered in conditioning and in the first retrieval. The order of neurons is identical across the three panels. Yellow arrowhead indicates the activity of the example cell shown in **a-b**. **e-h/** shows the same calculations as **a-d**, for CR-LT recipient amygdala neurons (N=16 cells from 3 mice), with a CR+ axonally photoactivated putative interneuron in **e-f**. The time bin with the foot shock is discarded from the calculation of the firing modulation and from the PSTH as well. It is the largest bin dominating the CS responses.

This goes in line with my data in anesthetized mice (see also later in **Figure 2.3.2.1./c** and **Figure 2.3.3.3./a**) showing that CR+LT preferentially target narrow-spiking amygdala neurons.

In both CR+ thalamic and CR+-recipient amygdala populations, unit activity showed modulations not only upon fear memory formation (Retr1), but also with extinction learning (Retr3), which further promotes the operative CR+LT role in aversive learning (**Figure 2.3.1.8./b-c, f-g**).

Overall, my results in freely moving animals show that CR+LT activity changes induced by aversive auditory cue association and learning can be responsible for the long-term modulation of amygdala circuits (Grewe *et al.*, 2017; Krabbe *et al.*, 2019). Response modulation of the CR+LT early in a threatening experience could provide animals with efficient aversive cue processing during subsequent exposures to danger, besides a memory trace being established in the amygdala. This is strongly supported by the behavioral data in (Barsy & Kocsis *et al.*, 2020) showing that suppressing the direct CR+LT→AMY route during CS+ presentation in conditioning or retrieval phases impairs aversive memory retrieval and cue discrimination, respectively.

DOI:10.15774/PPKE.ITK.2022.002

2.3.2. **Question IIb: Can sensory activations in the amygdala related to aversive auditory learning be directly derived from CR+ lateral thalamic neurons?**

The optimal and ultimate consequence of thalamo-amygdala activation under a new threatening experience is the formation of an aversive memory that can elicit defensive behavior upon subsequent exposure to the threat. In order to execute rapidly the necessary motor task and sustain the affective state, local networks in the amygdala need a mechanism to gate the incoming thalamic signals carrying aversive information. I aimed to acquire supporting data for such a mechanism.

Just as selective activation of the CR+LT was found during fear conditioning and retrieval, elevated c-Fos pattern was primarily observed in the CR+LT-innervated amygdala regions (Barsy & Kocsis *et al.*, 2020): the lateral (LA), centromedial (CeM), basomedial (BM) amygdala, the amygdalostriatal transition area (AStr) as well as a previously unspecified cluster of GABAergic neurons (named as supra-intercalated cluster of neurons, SIC) in the vicinity of the lateral and central amygdala.

(LeDoux *et al.*, 1990) originally marked the lateral amygdala (LA) and the adjacent amygdalostriatal transition area (AStr) as the ’sensory interface’ of the amygdala, as these two areas were found to receive ’acoustic’ projections from inferior colliculorecipient lateral thalamic regions. (Barsy & Kocsis *et al.*, 2020) also showed that in addition to the majority of LA-projecting thalamic neurons, AStr-targeting LT cells are predominantly (~92%) CR+, too, and 20-30% of CR+LT neurons innervate both regions. In concordance with this, c-Fos activation levels evoked by aversive conditioning and cued retrieval were comparable in the AStr and LA (Barsy & Kocsis *et al.*, 2020).

In the previous sections, I only indirectly assessed the CR+LT role in amygdala cue processing. To test the functional impact of the CR+LT innervation on the lateral amygdala region including the LA and AStr, the suggested interface areas in threat learning, CR+LT neurons were transduced with halorhodopsin (NpHR3.0) expressing AAV, and *in vivo* extracellular recordings (n=11) were performed from the amygdala (**Figure 2.3.2.1./a**). I investigated the contribution of the direct (subcortical) CR+LT projections to neutral sound as well as to aversive shock and paired tone+shock activation of neurons in the lateral region of the amygdala **Figure 2.3.2.1./b**).

Similarly to CR+LT neurons, CR+LT target amygdala regions exhibited stronger activation to foot shock and foot shock-associated tone than to tone alone (**Figure 2.3.2.1./c**, comparable to ~10% tone responses in (Grewe *et al.*, 2017)). Most of the cells had short-latency (<50 ms) responses, which predominantly started in the 15-35 ms poststimulus time window (**Figure 2.3.2.1./d**, see also median latencies in **Table 3.**). Aversive cues drove an earlier activation

DOI:10.15774/PPKE.ITK.2022.002

(~20 ms) than tones alone in the CR+LT target regions, too. The time course of aversive activation in the CR+ PIL and the amygdala (2-3 ms difference in latency on average) also suggests that aversive short-latency amygdala activation can be directly derived from the CR+LT.

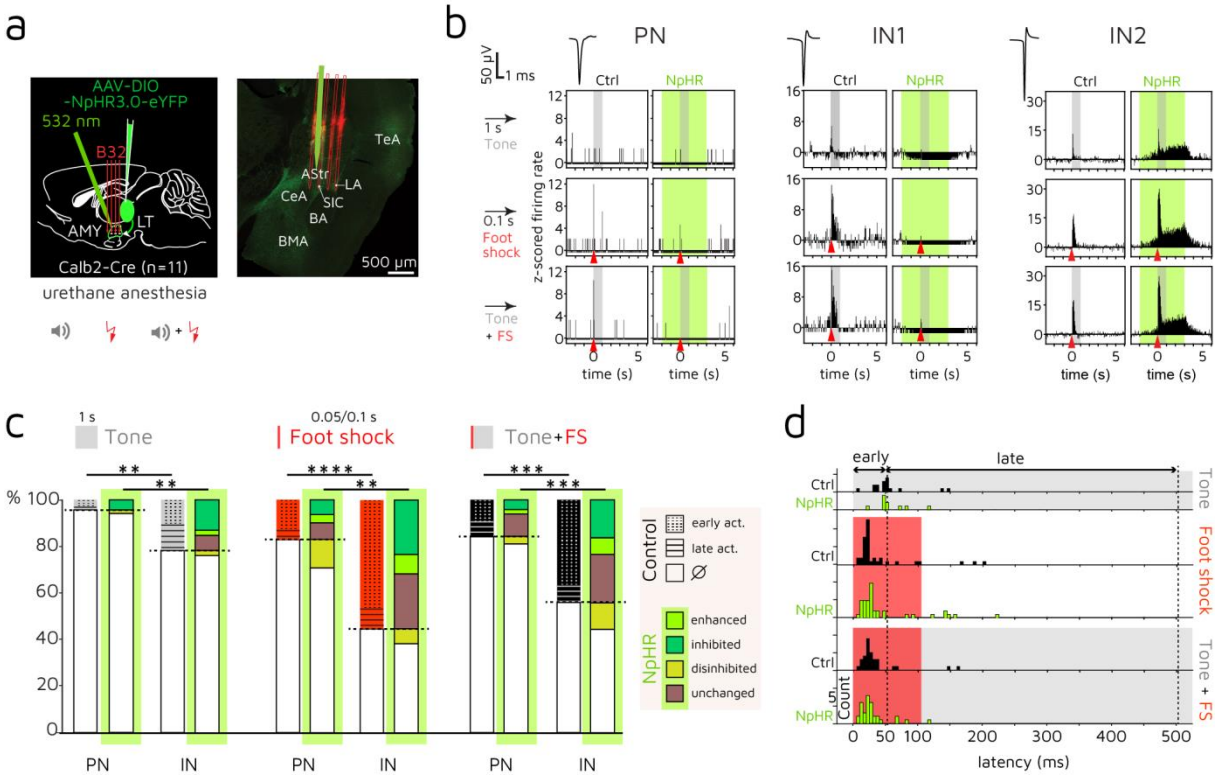

Figure 2.3.2.1. CR+LT neurons directly control the sensory activation of amygdala cells.

a/ Scheme (left) for acute *in vivo* electrophysiological recordings from the amygdala (n=11) with sensory stimulations and optogenetic inhibition of AAV-DIO-NpHR-eYFP-labeled CR+LT→AMY terminals. A representative coronal section (right) showing the insertion tracks of the optic fiber (green) and a four-shank DiI-stained Buzsáki32 probe (red) placed in the amygdala. **b/** Sensory responses of a broad-spiking putative principal cell (PN) and two narrow-spiking putative interneurons (IN) in control condition and during optogenetic inhibition (green) of CR+LT inputs. Gray shadings represent tone delivery, red arrowheads mark the delivery of foot shock (FS) stimuli. Bin size is 50 ms. Mean spike waveforms are shown above the PSTHs. **c/** Population data for tone-, foot shock- (FS) and tone+FS-evoked activities of amygdala neurons (LA/AStr/SIC in n=8 mice) divided into putative principal cells (PN) and interneurons (IN). Evoked responses in control conditions and response modulations during NpHR-mediated CR+LT→AMY axonal inhibition (graphs with green frame) are shown. *χ^2 test*. **d/** Histograms depicting the distribution of sensory response latencies calculated for amygdala cells separately for control evoked activities (black bars) and for responses upon CR+LT axonal inhibition (green bars). Note that the majority of early evoked activity takes place in the 15-35 ms time window after cue delivery. Bin size is 5 ms. *Wilcoxon rank-sum test (two-sided).*

Panels a-b published in Figure 5./a, b, d, and in Supplementary Figure 5./f in (Barsy & Kocsis et al., 2020).

Sensory stimuli most prominently activated putative interneurons, which can be drastically suppressed by CR+LT axonal inhibition (**Figure 2.3.2.1./b-c**). Overall, narrow-spiking cells were significantly more affected by the suppression of direct thalamic inputs than broad-spiking

DOI:10.15774/PPKE.ITK.2022.002

neurons. In addition to the suppressed responses, many neurons enhanced their evoked activation. Furthermore, some neurons only showed activation to sensory stimuli during CR+LT→AMY optogenetic silencing, indicating the presence of a thalamus-driven disinhibitory mechanism in the amygdala. Response latencies did not change significantly with CR+LT axonal inhibition, which can possibly be attributed to this disinhibitory mechanism (**Figure 2.3.2.1./d**).

Since neither immediate early gene expression (IEG; e.g., c-Fos) essays, nor optogenetic suppression can concisely infer which areas can receive firsthand short-latency aversive information from the CR+LT, I aimed to map direct thalamic and shock-evoked effects with a 256-channel probe that can cover the entire amygdala (**Figure 2.3.2.2./a**). To this end, I additionally recorded nociceptive foot shock responses from urethane-anesthetized mice (n=3), and I photoactivated AAV-DIO-ChR2-eYFP transduced CR+LT axons in the amygdala.

Both in the case of optogenetic and foot shock stimuli, local-field potential (LFP, **Figure 2.3.2.2./b-c**) and current source density (CSD) maps (**Figure 2.3.2.2./d**) placed the earliest amygdala activation in the AStr and the LA, which confirms that these areas together provide the sensory interface for the lateral thalamus (LeDoux *et al.*, 1990). Earlier negative LFP peak latencies in the AStr (5 and 15 ms vs. 10 and 20 ms in the LA) may stem from a temporally and spatially (dorsoventrally) more extended LA activation. (**Figure 2.3.2.2./e**).

Optogenetically evoked and nociceptive field responses in these areas are dominantly positive potentials similarly to the one observed by (Clugnet & LeDoux, 1990) upon electrical stimulation of the auditory thalamus. This phasic positivity (also shown in **Figure 2.3.1.3./b**, **Figure 2.3.1.7./d** and later in **Figure 2.3.3.2./c**) appears on the CSD map as a current source, which abruptly (in 5-10 ms) exchanges a sink in the LA-AStr region. Despite the limited value of the LFP in characterizing underlying network activities (Herreras, 2016), and the non-laminar structure of the amygdala, this spatiotemporal activation profile can potentially reflect a feedforward inhibitory mechanism at the LT inputs in the amygdala, as suggested by (Li *et al.*, 1996*a*) in their combined electrophysiological / modeling study. The inhibitory mechanism is also supported by my acute electrophysiological data (**Figure 2.3.2.1./c**, and later in **Figure 2.3.3.4./c-d**) highlighting a dominant interneuron function in aversive signaling.

In summary, the subcortical CR+LT route to the amygdala establishes a sensory interface by targeting both principal and interneurons, and its contribution to local inhibitory actions can mediate robust aversive encoding in the local circuit.

DOI:10.15774/PPKE.ITK.2022.002

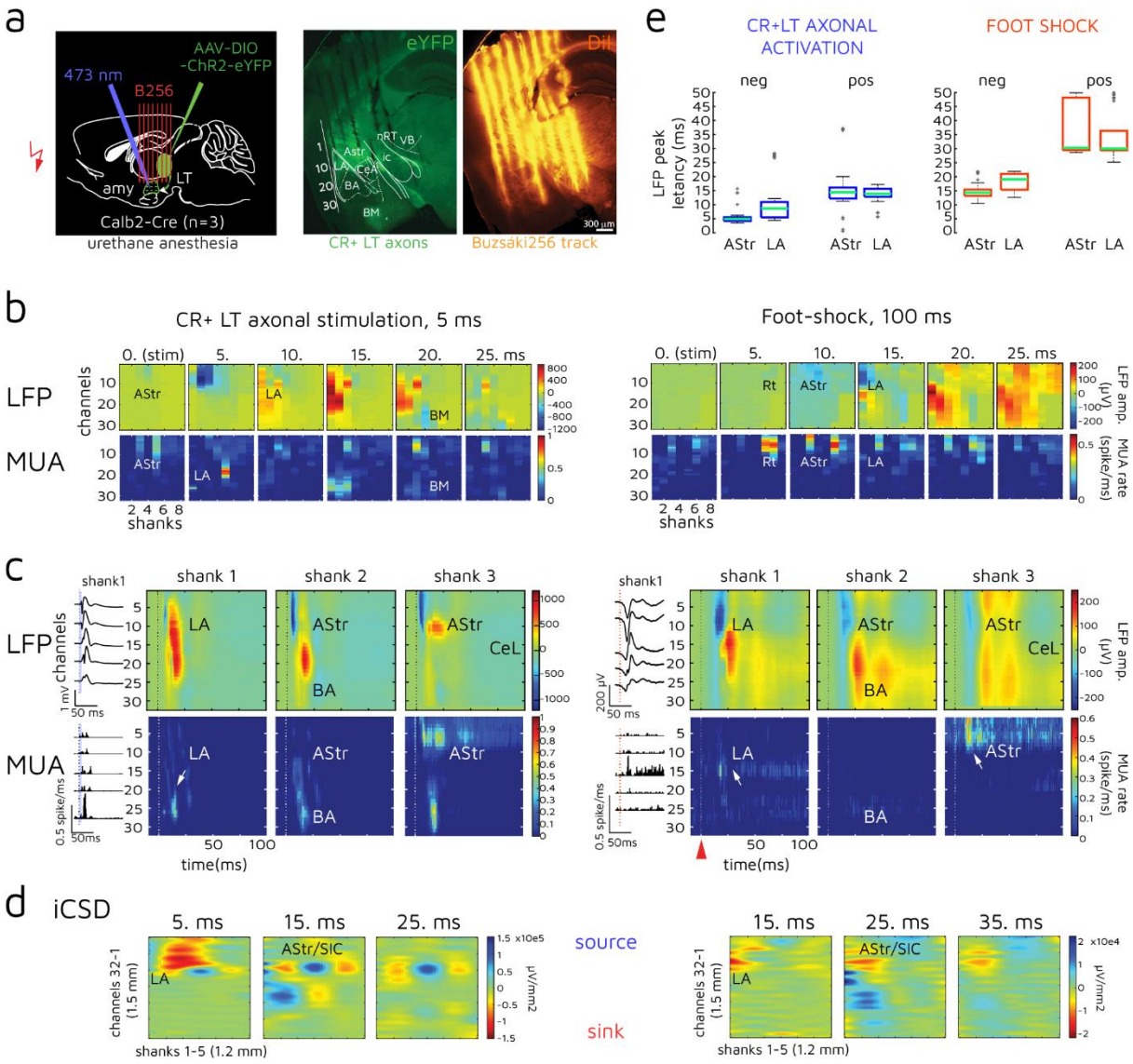

Figure 2.3.2.2. Spatiotemporal profiles of CR+LT axonal and aversive activation in the amygdala.

a/ Scheme (left) for acute *in vivo* electrophysiological recordings from the amygdala (n=3 mice) with foot shock stimulation and optogenetic excitation of AAV-DIO-ChR2-eYFP-transduced CR+LT→AMY inputs. A coronal section (middle) showing the incoming transduced CR+LT fibers (eYFP, green) with schematic internuclear borders and the DiI-stained (red) 8-shank Buzsáki256 probe track (right). Track analysis was supported by characteristic burst activity on the contacts covering the Rt. **b/** Representative snapshots (in ms) of the mean evoked responses in broadband (upper rows) and sorted multi-unit (bottom rows) activity across the 256 probe channels (32 channels on 8 shanks) covering the amygdala. Optogenetic (left) and shock-evoked (right) responses are shown in two columns. **c/** Mean evoked responses in broadband (upper rows) and sorted multi-unit (bottom rows) activity on the first three lateral probe shanks from **b**. **d/** Current source density maps calculated from the mean broadband evoked responses on the first five probe shanks from **b**. The representative snapshots were shifted with 10 ms (synaptic delay) for peripheral shock-evoked activation for comparative purposes. **e/** Peak latencies for the broadband mean evoked responses from the contacts in the AStr (N=55 contacts) and LA (N=53 contacts) regions in the case of optogenetic (left, blue) and nociceptive (right, red) evoked responses.

DOI:10.15774/PPKE.ITK.2022.002

2.3.3. **Question IIc: What are the possible upstream sources of multimodal cue processing along the direct thalamo-amygdala route?**

As previously described by electrophysiological, behavioral and anatomical (IEG) experiments from (Barsy & Kocsis *et al.*, 2020), the CR+LT is specifically activated by the aversive modalities in threat conditioning. Further mouse behavioral data, perfectly in line with this, show that even a brief optogenetic silencing of the CR+LT→AMY axons – covering only the last few seconds of CS+ presentation including the US –, results in similar behavioral changes as inhibiting during the entire sound. Thus, disrupting CR+LT processing of associative CS+US alone is sufficient to impair aversive memory establishment. Adding another line of evidence to the multisensory aspect of CR+LT cue processing, contextual memory retrieval was shown to be impaired by silencing the direct CR+LT→AMY route during cue association, but also only during contextual retrieval itself (Barsy & Kocsis *et al.*, 2020). These highlight the potential importance of collothalamic processing, which can reach beyond parallel sensory transmissions, and perform cue integration / discrimination before any amygdala computation. Here, I investigated whether the colliculo-thalamic routes can provide the amygdala with short-latency aversive and multimodal cues.

Anatomical exploration of upstream inputs on LT neurons predicts their responsiveness to auditory, visual and somatosensory signals, too (LeDoux *et al.*, 1987; Linke *et al.*, 1999; Smith *et al.*, 2007). First, I aimed to identify the distribution of collicular inputs in the CR+LT region with anterograde viral tracing. To test both glutamatergic (excitatory) and GABAergic (inhibitory) midbrain innervation of the CR+LT, I injected Cre-dependent enhanced Yellow Fluorescent Protein (eYFP) expressing AAV into the inferior (IC) and superior (SC) colliculus of vGluT2-Cre (n=3-3, **Figure 2.3.3.1./a-b** and **j-k**, respectively) and vGAT-Cre mice (n=2-2, **Figure 2.3.3.1./q-r** and **t-u**, respectively).

Transduced vGluT2+ IC neurons formed two types of synaptic connections in the ipsilateral LT (Bartlett *et al.*, 2000): whereas large-sized axon terminals (~3-5 μm in diameter) were distributed in the CR-negative MGN (**Figure 2.3.3.1./d-e**), small boutons (<1 μm) targeted the regions of CR+LT neurons (**Figure 2.3.3.1./f-h**). In contrast, transduced glutamatergic SC neurons sent axon terminals exclusively to CR+LT territories (**Figure 2.3.3.1./l-m**). Asymmetrical (excitatory) synaptic contacts between IC (N=43 boutons) / SC (N=51 boutons) inputs and the CR+LT were confirmed with electron microscopy (**Figure 2.3.3.1./i**, and **n-p**, respectively).

vGAT+ (inhibitory) IC and SC neurons had a similar projection pattern to excitatory ones (**Figure 2.3.3.1./s**, and **v**, respectively); GABAergic SC terminals only innervated the CR+LT region.

DOI:10.15774/PPKE.ITK.2022.002

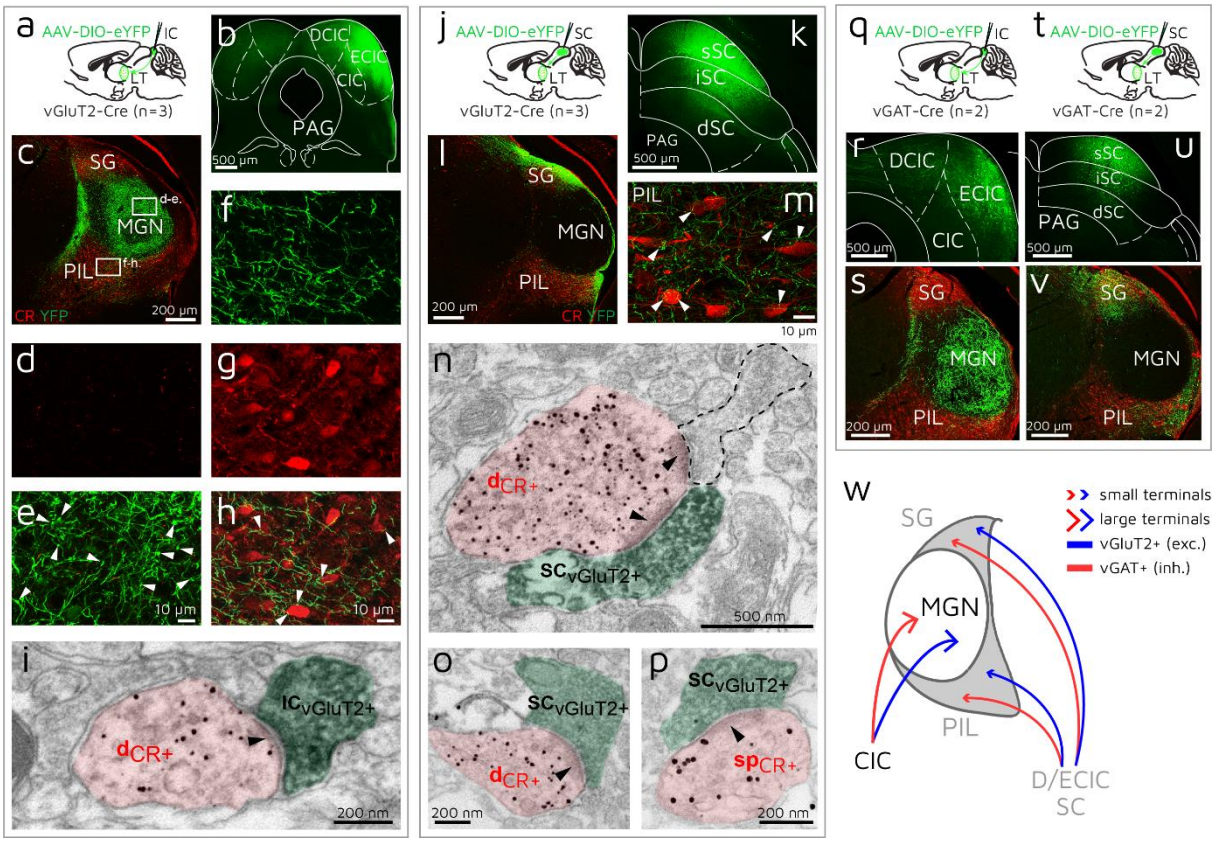

Figure 2.3.3.1. Collicular innervation of the CR+LT region is non-primary and multimodal.

a/ Scheme for AAV-DIO-eYFP injections into the inferior colliculus (IC) of vGluT2-Cre mice (n=3). **b/** Injection site in the IC. **c/** vGluT2+ IC inputs (eYFP, green) in the LT, which is co-stained for CR (red). White framed areas are enlarged in **d-e** and **f-h**. **d-e/** z-stack confocal image (7 µm total depth) from the MGN (CR- area in **d**) showing large-sized IC axon terminals (white arrowheads in **e**). **f-h/** z-stack confocal image (7 µm total depth) from the PIL (red CR staining in **g**) illustrating small-sized IC axon terminals (**f**; white arrowheads in **h**) in the vicinity of CR+ PIL cells. **i/** Electron micrograph showing an immunogold-labeled CR+ dendrite in the PIL (dCR+; covered by small black particles; shaded with pink) receiving an asymmetric synaptic contact (black arrowhead) formed by a DAB-labeled (diffuse black precipitate) vGluT2+ IC axon terminal (ICvGluT2+; shaded with green).

j/ Scheme for AAV-DIO-eYFP injections into the superior colliculus (SC) of vGluT2-Cre mice (n=3). **k/** Injection site in the SC. **l/** vGluT2+ SC inputs (eYFP, green) in the LT, which is co-stained for CR (red). **m/** z-stack confocal image (7 µm total depth) with vGluT2+ SC axon terminals (white arrowheads) in close proximity to CR+ PIL neurons (red). **n-p/** Electron micrographs showing immunogold-labeled CR+ dendrites (dCR+ in **n-o**) and a spine (spCR+; **p**) in the PIL receiving asymmetric synaptic contacts (black arrowheads) from DAB-labeled, vGluT2+ SC axon terminals (SCvGluT2+). A non-stained axon terminal with dashed outline (in **n**) also gives synaptic input onto the CR+ dendrite.

q/ Scheme for AAV-DIO-eYFP injections into the IC of vGAT-Cre mice (n=2). **r/** Injection site in the IC. **s/** vGAT+ IC inputs in the LT, which is co-stained for CR. **t/** Scheme for AAV-DIO-eYFP injections into the SC of vGAT-Cre mice (n=2). **u/** Injection site in the SC. **v/** vGAT+SC inputs (eYFP, green) in the LT, which is co-stained for CR (red). **w/** Schematic drawing for the collicular inputs of CR+LT territories (PIL/SG) in contrast to those of the primary auditory nucleus (MGN).

Panels a-p published in (Barsy & Kocsis et al., 2020) Figure 3./h-w.

DOI:10.15774/PPKE.ITK.2022.002

These results are in concordance with the study of (Smith *et al.*, 2007) who described typically small SC and IC terminals in related lateral thalamic nuclei in rats. These were shown to generate small excitatory postsynaptic potentials (EPSPs) but could be also summed to a large synaptic event with NMDA and AMPA components. They also described inhibitory projections from both colliculi. I also suppose that colliculorecipient CR+LT regions can overlap with the distinctive population of MGV tufted neurons and MGD stellate cells that (Bartlett *et al.*, 2000) characterized. This cohort receives small excitatory IC and inhibitory IC terminals, in contrast to the primary auditory thalamic regions innervated by mostly excitatory large IC boutons, which evoke the large collicular EPSPs.

This innervation pattern was further confirmed by monosynaptically restricted transsynaptic, Cre-dependent rabies tracing in (Barsy & Kocsis *et al.*, 2020). CR+LT neuron-targeting cells were found in the multimodal external and dorsal cortex of the IC (Coleman & Clerici, 1987), only sparsely distributed in primary auditory central locations. In the SC, visual ‘wide field’ neurons in the superficial as well as multisensory neurons of the intermediate and deep layers were equally transduced (King, 2004). In addition, lower densities of rabies-labeled cells were found in the PAG and in the principal sensory trigeminal nucleus (Pr5).

The revealed CR+LT-projecting brainstem regions have non-primary and multimodal sensory characteristics and may have the potential to transfer short-latency auditory (IC), visual (SC), nociceptive/tactile (SC, PAG and Pr5) as well as multimodal (SC/IC) cues (Hayashi *et al.*, 1984; Linke *et al.*, 1999). Moreover, as the mouse thalamus typically lacks local inhibitory control, the interplay between excitatory and inhibitory midbrain afferents can have a direct and powerful role, in addition to reticular inhibition, in increasing the signal-to-noise ratio of saliency processing in the CR+LT (**Figure 2.3.3.1./w**).

These anatomical data support that CR+LT cells receive and potentially integrate multiple sensory modalities of brainstem origin, which could provide a subcortical bypass from elaborated primary sensory processes under threat.

DOI:10.15774/PPKE.ITK.2022.002

In a rich literature, the superior colliculus (SC) has long been suggested to play prominent role in rapid extraction, integration and transmission of visual information to other subcortical structures, helping rodents orient as well as detect and avoid fast approaching raptors (see looming detection) (Sahibzada *et al.*, 1986; Liu *et al.*, 2011). Nevertheless, its role in providing cues for learned aversion has not been thoroughly investigated yet.

Since the hallmark of CR+LT neuronal activation was nociceptive, and the superior colliculus distinctively targets the CR+LT region, the question arises if these tectothalamic connections can functionally contribute to aversive amygdala cue processing. Furthermore, (Linke, 1999) showed with Miniruby injections that spread both antero-and retrogradely, that SC innervation of amygdala-projecting lateral thalamic nuclei appears to be more distinctive than the IC inputs: whereas the SG mostly receives inputs from the superficial *stratum opticum*, the MGM and the PIL are targeted by the intermediate and deep multimodal layers. Importantly, nociceptive unimodal or multimodal neurons are widely distributed in these layers in golden hamsters (Stein & Dixon, 1978), capable of mediating responses to harmful stimuli. These further suggest that aversive cue responses along the CR+ PIL→AMY can potentially stem from a tectal innervation.

To further tackle this problem, I studied the time-course of amygdala shock activation in a supplementary data set from anesthetized animals. For identification purposes, I optogenetically stimulated AAV-DIO-ChR2-eYFP-transduced vGluT2+ SC-axons in the LT (6 sites in n=3 vGluT2-Cre mice) as well as incoming AAV-DIO-ChR2-eYFP-expressing CR+LT axons locally (n=4 Calb2-Cre mice, **Figure 2.3.3.2./a**).

Optogenetic activation of excitatory SC fibers was done in the PIL for two reasons. On the one hand, PIL neurons showed higher short-latency responsivity for nociceptive signals. On the other hand, the SG is close to the SC, so in the ventral CR+LT region, I could avoid directing light onto somatically transduced SC neurons. Amongst LT target regions, single unit activations only from the lateral amygdala (LA) and amygdalostriatal transition area (AStr) were included just as described before.

Importantly, disynaptically activated colliculo-thalamorecipient amygdala cells showed an identical median shock response latency (20 ms) to that of directly activated CR+LT-recipient neurons (**Figure 2.3.3.2./b-c**), presumably, I recorded from similarly activated amygdala populations. CR+LT axonally evoked optogenetic and shock response latencies in the amygdala are also in concordance with the first LFP peak latencies shown earlier in **Figure 2.3.2.2./b** (see also median latencies in **Table 3.**).

Time lags between optogenetically elicited short-latency (<20 ms) responses in the CR+LT and the amygdala showed a sequential activation along the suggested colliculo-thalamo-amygdala route involving CR+ thalamic cells (**Figure 2.3.3.2./b-c**).

DOI:10.15774/PPKE.ITK.2022.002

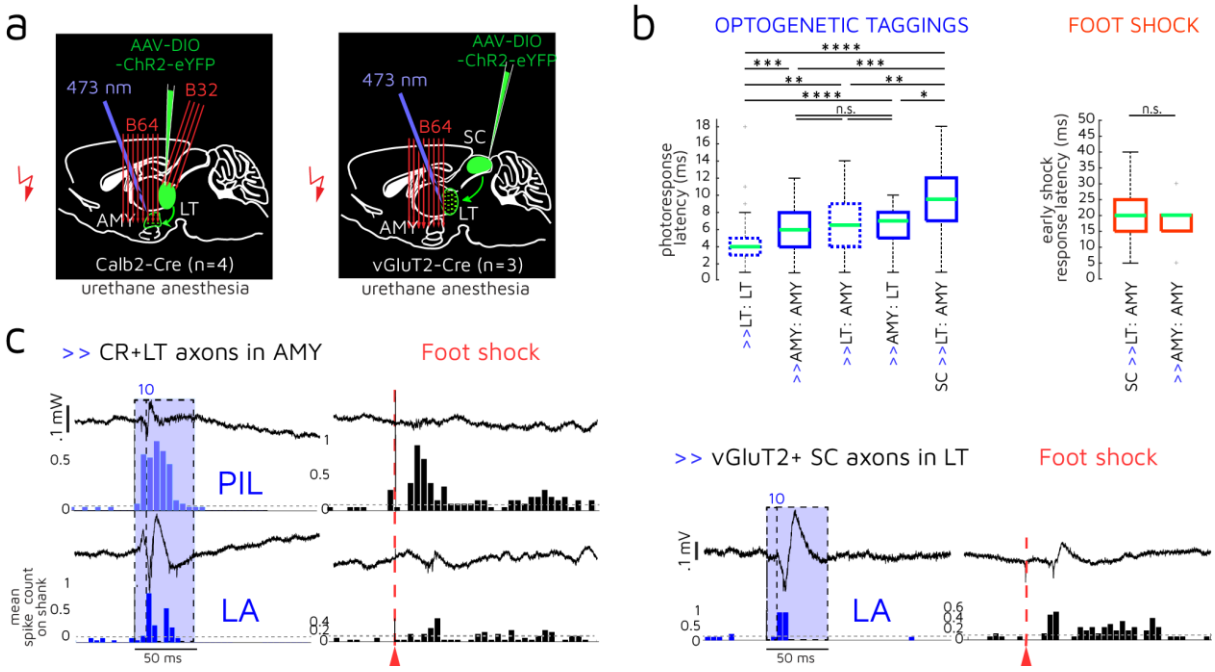

Figure 2.3.3.2. Probing the colliculo-thalamo-amygdala route in aversive cue processing.

a/ Scheme for two sets of acute *in vivo* electrophysiological recordings with aversive foot shock stimulations alongside CR+LT axonal (n=4 mice) or disynaptic vGluT2+ colliculo-thalamic (n=3 mice) activation of amygdala neurons. In the first set of experiments, I also recorded from the LT (n=3 mice). **b/** Comparison of short-latency optogenetic (<20 ms) and foot shock (<50 ms) response latencies of thalamic and amygdala (LA/AStr) neurons photoactivated from different locations. In two cases (dashed boxes), data were acquired in former experiments (**Figure 2.3.1.3./a**). Time lags between activations suggest a sequential activation from the superior colliculus to CR+LT neurons, then to the amygdala. Blue arrows indicate the location of photoactivation. In the case of vGluT2-Cre animals, the SC is indicated as the source of the activated fibers; in all other cases, CR+ somas or axons were stimulated. *Wilcoxon rank-sum test (two-sided), *p < 0.05; **p < 0.01; ***p < 0.001; ****p < 0.0001; n.s., not significant.* **c/** Two sets of broadband neural traces (upper trace) from a single electrode channel located in the PIL and/or amygdala (AMY) with sorted unit activity (bottom PSTH) from the respective electrode shank. Bin size is 5 ms. Gray horizontal dashed line indicates 2 SD above the mean baseline spike rate.

Disynaptic optogenetic activation revealed that excitatory superior colliculo-thalamo-recipient amygdala regions (LA/AStr) preferentially show early (<50 ms) onset responses to aversive stimulation, which is comparable to the effect amongst CR+LT axonally activated amygdala neurons. In both cases, shock-responsivity of non-activated cells were similar to the neighboring cortical (piriform, Pir and entorhinal, En) activation recorded on the lateral shanks, and significantly different from the photoactivated cohort. Putative interneurons were more likely to participate in both onset and offset responses, and their proportion amongst optogenetically activated neurons were significantly higher than in the non-activated cohorts (**Figure 2.3.3.3./a-b**).

DOI:10.15774/PPKE.ITK.2022.002

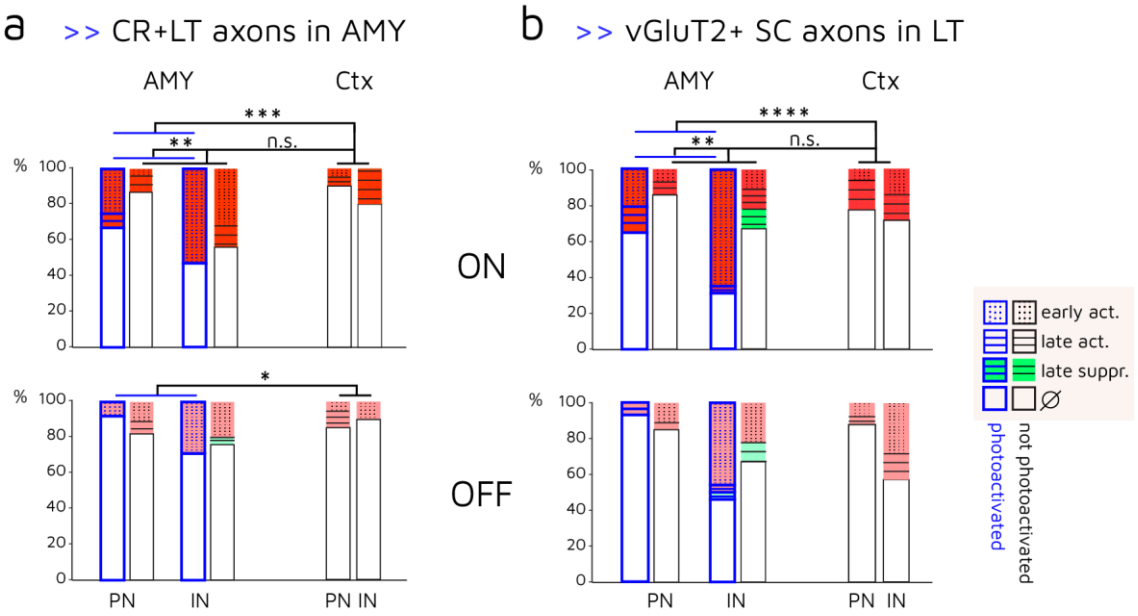

Figure 2.3.3.3. Nociceptive cue responses are prominent in CR+LT target and colliculo-thalamorecipient cells in the amygdala.

a-b/ Proportions of onset (ON, upper row) and offset (OFF, bottom row) shock responses in LT target (LA and AStr) regions as well as in the neighboring cortical (Pir and En) areas, separately shown in putative principal (PN) and interneurons (IN). CR+LT (in **a**) or vGluT2+ SC axonally (in **b**) photoactivated amygdala units (blue framed boxes), respectively, showed larger activation to the nociceptive stimulus than not activated amygdala and cortical neurons (black framed boxes). *χ^2 test. *p < 0.05; **p < 0.01; ***p < 0.001; ****p < 0.0001; n.s., not significant.*

Finally, shock-evoked responses of cells in the lateral thalamus and the lateral region of the amygdala were characterized by their local population firing activity. Population vector rotations, characteristic to phasic transient activities in various sensory systems and species (Mazor & Laurent, 2005; Bartho *et al.*, 2009), were present both along the direct thalamo-amygdala pathway (**Figure 2.3.3.4./a**) and amongst colliculo-thalamorecipient amygdala neurons (**Figure 2.3.3.4./b**), within the 50 ms poststimulus interval. Offset transients were present, but less prominent on the population level. Sustained responses reflected less dynamic activities close to the baseline. This infers to quickly evolving and coherent population activities marking the duration of the nociceptive cue. Again, the time-course of activation testifies that the aversive response properties along the direct thalamo-amygdala route do not simply arise from a state change-related firing rate elevation.

In the representative examples from both conditions, phototagged putative interneurons beared dominant loadings (coefficients) in principal components (PCs), showing strong phasic shock responses (**Figure 2.3.3.4./c-d**). This could be partially attributed to a relatively high firing rate in interneurons, but correction for the baseline firing rate did not change the trajectories and the dominant loadings of the PCs.

DOI:10.15774/PPKE.ITK.2022.002

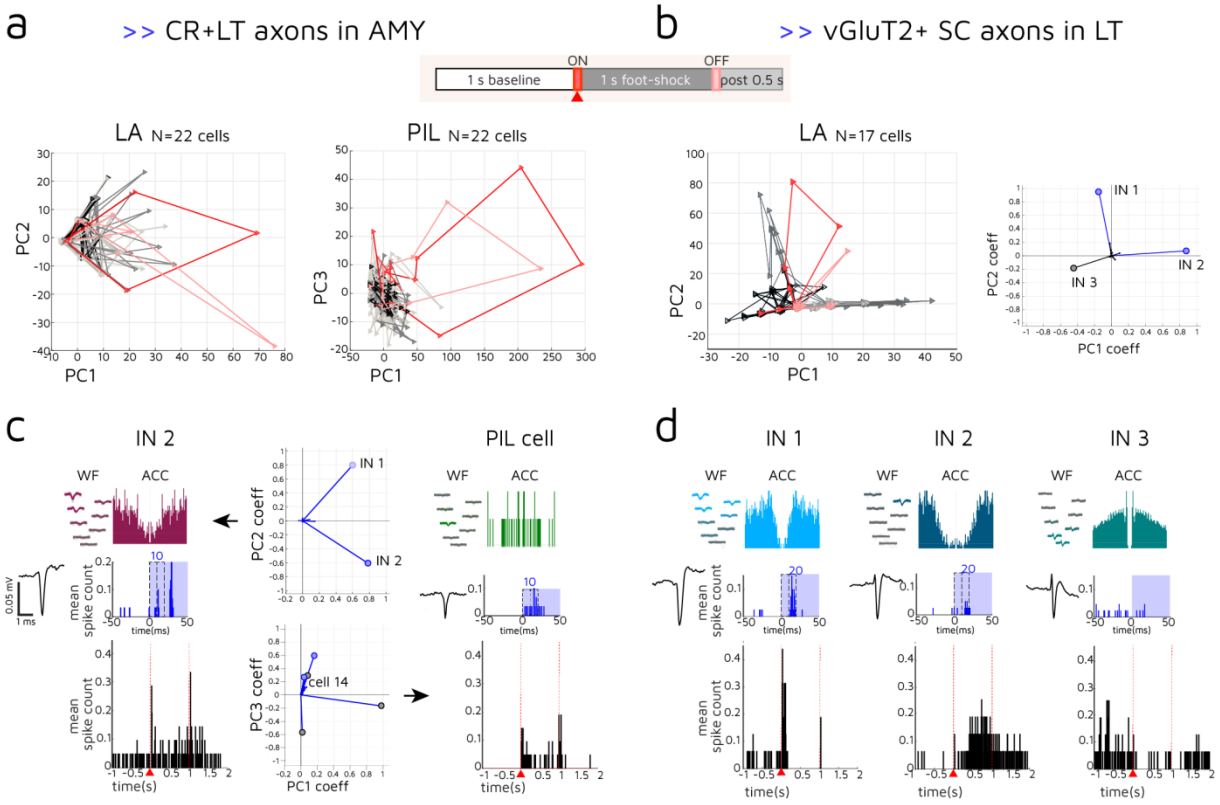

Figure 2.3.3.4. Time-course of nociceptive activation in LT and amygdala populations.

a-b/ Population rate vector trajectories, projected onto two principal components (PC), indicate phasic onset (ON, red) and offset (OFF, pink) transient responses as well as a less prominent sustained activity in LT and amygdala units. The trajectories are shown 1 s before (black), during (1 sec, dark gray) and 0.5 s after (light gray) shock stimulation. PIL and LA units in **a** were recorded in the same experiment. **c-d/** Example units selected based on their relatively large weight on the two PCs from **a-b**, respectively. Mean action potential waveforms, raw overlapping spikes (WF) mapped onto the shank's channel configurations, autocorrelograms (ACC), photoactivations (blue PSTHs) and foot shock responses (black PSTHs) are shown for each cell. Whereas CR+LT axonal phototagging results in elevated firing in the first 10 ms in the case of the thalamic and the amygdala cell (**c**), activation of vGLUT2+ collicular fibers in the LT elicits a rather disynaptic (>10 ms) response in the amygdala (**d**). All representative LA neurons are putative interneurons (IN). Notably, IN 3 in **d** is not a photoactivated unit and shows suppressed activity during shock stimulation.

Overall, this extended data further support the instrumental role of CR+LT-connected amygdala interneurons in the phasic and short-latency encoding of nociceptive events, which can be routed by colliculorecipient thalamic neurons with similar response characteristics. Though only limited conclusions can be drawn about the origin of nociceptive responses in the amygdala based on this complementary data, adding the evidence that the majority of amygdala-projecting LT neurons are CR+, and that CR+ cells are innervated by the SC, one can suggest a possible overlap between the colliculo-thalamorecipient and CR+LT-targeted amygdala population in aversive processing. Furthermore, mean response latency of nociceptive-specific neurons (~13 / 15 ms) in the hamster SC (Larson *et al.*, 1987) marks one synaptic delay from CR+LT shock-activation (~17 ms) shown in my study.

DOI:10.15774/PPKE.ITK.2022.002

2.4. Discussion

Based on our studies (Barsy & Kocsis *et al.*, 2020), the transgenic Calb2-Cre mouse line makes it possible to study the vast majority (94%) of lateral amygdala(LA)-projecting thalamic cells in the posterior intralaminar (PIL) and suprageniculate (SG) thalamic nuclei that express the calretinin (CR) calcium-binding protein. These neurons also target amygdala-projecting cortical areas, thus, calretinin is a valuable tool to functionally dissect both the subcortical ('low road') and cortical routes ('high road') (LeDoux, 1994) for aversive cue processing in learned threat-evoked behavior.

2.4.1. **Thesis IIa**

I showed with extracellular electrophysiological recordings in urethane-anesthetized and freely behaving mice that lateral thalamic calretinin-positive (CR+LT) neurons process both neutral auditory and aversive (nociceptive or threat-related auditory) cues. They exhibit multisensory and associative enhancement on a single neuronal level.

Related journal publication: Barsy, B.*, Kocsis, K.*, Magyar, A., Babiczky, Á., Szabó, M., Veres, J.M., Hillier, D., Ulbert, I., Yizhar, O., and Mátyás, F. (2020). Associative and plastic thalamic signaling to the lateral amygdala controls fear behavior. *Nature Neuroscience, 23(5)*, pp. 625–637.

I participated in the conception, design and methodological foundation of the electrophysiological and behavioral experiments. I carried out surgeries, viral injections and implantations, I carried out the behavioral tests. I performed the acquisition, analysis and interpretation of the acute and chronic electrophysiological data. I took part in the drafting and revision of the related section of the manuscript.

I have provided multiple lines of evidence that CR+LT neurons do not simply relay single sensory modalities (auditory CS/nociceptive US) in threat learning: they can compute associated information prior to the amygdala within a short time window (~17 ms) and show experience-dependent activity changes. This does not simply manifest in the recruitment of active neurons, but also on a single cellular level. These observations further challenge the widely accepted concept that the LA is the first site of CS-US association (**2.3.1.**).

The foot shock response was the hallmark activity with the shortest latency in the CR+LT. Early nociceptive responses were more characteristic to the posterior intralaminar (PIL) thalamic nucleus; their phasic activations underwent multisensory enhancement even in the absence of unimodal acoustic responses. As (Ryugo & Weinberger, 1978) found in cats, MGM neurons that showed conditionability (increased multiple unit activity), were active only during the US, contrary to neurons which lacked enhancement and continued firing even after paw

shock. They also pointed out that the observed thalamic response plasticity is attributed to the US response rather than to the properties of CS-evoked activity.

Moreover, the PIL, together with the suprageniculate (SG) nucleus, can provide longer latency or sustained activity changes, too. This latter was shown in both acute and chronic recording conditions with longer stimulations. Delayed activations can potentially be attributed to local axon collaterals, described in (Barsy & Kocsis *et al.*, 2020), and also proposed by (Smith *et al.*, 2007) showing a second, longer latency EPSP in the MGM and SG upon collicular (IC and SC) stimulation.

Taken together, my results suggest that the CR+LT is a good candidate for a functional delineation of the multimodal afferentation that supports the amygdala along aversive cue learning. It can also serve as a target population for studies on thalamic associative plasticity and activity changes during aversive cue processing. My findings have also been reviewed by (Gründemann, 2021), who, together with (Headley *et al.*, 2019), raises awareness to a distributed subcortical neuronal network function in defensive behavior. Although the computational capacities of non-canonical thalamic elements are limited, their investigation can further our understanding on behavioral plasticity.

2.4.2. **Thesis IIb**

I found in urethane-anesthetized mice with extracellular electrophysiological recordings that calretinin-positive lateral thalamic (CR+LT) neurons can directly convey aversive uni- and multimodal cues to the lateral region of the amygdala where their signaling recruits narrow-spiking neurons.

Related journal publication: (Barsy & Kocsis *et al.*, 2020)

I participated in the conception, design and the methodological foundation of the electrophysiological experiments. I carried out surgeries and viral injections, as well as the acquisition, analysis and interpretation of the acute electrophysiological data. I took part in the drafting and revision of the related section of the manuscript.

I confirmed that calretinin-positive (CR+) neurons in the lateral thalamus fulfill the prerequisites for the function of direct thalamo-amygdala pathways in auditory threat conditioning: besides auditory cues, they can directly convey short-latency nociceptive and integrated signals to the principal subcortical area of aversive learning, the lateral region of the amygdala (**2.3.2.**).

Nociceptive cue-evoked responses were the shortest latency and strongest activities in the recorded amygdala populations, similarly to CR+LT neurons. The majority of shock-responsive CR+LT-target cells exhibited phasic short-latency responses in the lateral amygdala (LA) and the neighboring amygdalostriatal transition area (AStr). I showed that aversive cue responsivity

was particularly abundant amongst narrow-spiking neurons in these regions. This is supported by the c-Fos data presented in (Barsy & Kocsis *et al.*, 2020), highlighting a previously undescribed population of inhibitory cells in the vicinity of the lateral (LA) and central (CeA) amygdala, named supra-intercalated cluster of neurons (SIC). Notably, direct optogenetic CR+LT-mediated modulations, be they excitatory or inhibitory, affected putative interneurons to a larger extent (see also in **2.3.3.**).

My results support the previous finding according to which amygdala-targeting lateral thalamic neurons connect to both principal and interneurons, suggesting a feed-forward inhibitory effector mechanism (Woodson *et al.*, 2000). Thalamic input-mediated inhibitory and disinhibitory mechanisms, also shown in my data, have been previously identified both in the neocortex and the amygdala complex during aversive cue processing, and play important role in sensory gating during threat learning (Woodson *et al.*, 2000; Letzkus *et al.*, 2011; Wolff *et al.*, 2014; Asede *et al.*, 2015; Krabbe *et al.*, 2019). There are multiple candidates for executing these actions in the amygdala. As SIC neurons send axon collaterals to other SIC as well as to LA cells (Barsy & Kocsis *et al.*, 2020), this population can be equally involved in feedforward inhibitory and disinhibitory thalamic effects similarly to the intercalated nuclei (ITC) and the local LA interneurons (Woodson *et al.*, 2000; Wolff *et al.*, 2014; Asede *et al.*, 2015; Krabbe *et al.*, 2019).

Thus, thalamic inputs, fulfilling an imminent need to prioritize threatening cues, may directly drive population selection by targeting amygdala interneurons: (1) establishing a window of phasic elevation in onset and offset firing rates (Pouille & Scanziani, 2001), as well as potential synchronization, (2) suppressing the cohort activities which do not serve saliency detection, making network output and ultimately behavior efficient, (3) regulating plasticity along the somatodendritic axis of principal neurons. Deficits in inhibitory functions have been associated with maladaptive affective behaviors and memory (Marín, 2012), and in fact, modulation of the direct CR+LT→AMY changes the efficiency of affective cue discrimination (Barsy & Kocsis *et al.*, 2020).

2.4.3. **Thesis IIc**

I confirmed with anterograde viral tracing in mice that the calretinin-positive lateral thalamic (CR+LT) population relies on a non-primary and multimodal midbrain innervation from the inferior (IC) and superior (SC) colliculi. The CR+LT region is exclusively targeted by the superior colliculus.

Related journal publication: (Barsy & Kocsis *et al.*, 2020)

I participated in the conception and design of the anatomical investigation. I carried out the surgeries and viral injections, I participated in the anatomical processing and the interpretation of the results. I took part in the drafting and revision of the related section of the manuscript.

DOI:10.15774/PPKE.ITK.2022.002

A potential functional anatomical basis for the previously declared theses is established by a midbrain innervation with non-primary and multimodal character, also distinct from the one in the adjacent primary auditory thalamus, the medial geniculate nucleus. I showed that CR+LT cells are targeted by sparse and small terminals from the inferior colliculus (IC); the superior colliculus (SC) exclusively targets the CR+ PIL/SG region (**2.3.3.**).

Such collicular innervation can promote CR+LT neurons to rapidly integrate cues upstream to the amygdala and the neocortex, potentially both from neutral sensory and ethologically relevant integrated information. Afferent IC/SC terminals in the CR+LT region can be both excitatory and inhibitory, which can further enhance the computational capacities of the thalamic population that lacks local inhibitory control. I propose that they may contribute to encoding temporal features, such as cue duration (see thalamic and amygdala offset responses in **2.3.1.**) in aversive cue processing. Notably, (Yu *et al.*, 2004) reported acoustically evoked IPSPs besides EPSPs only in the non-lemniscal MGN area, with a latency excluding an afterhypolarization effect; this dual excitatory-inhibitory drive can then possibly further potentiate rebound offset responses in these neurons. According to (Yu *et al.*, 2004), selective suppression of these multisensory thalamic cells can prepare the neocortex to receive subsequent auditory information.

Furthermore, the SC-targeted CR+LT→AMY route can contribute to hippocampus-independent contextual memory formation and retrieval (Zelikowsky *et al.*, 2012). Silencing this direct thalamo-amygdala pathway not only impaired auditory cued threat learning, but also the establishment and recall of contextual fear memory (Barsy & Kocsis *et al.*, 2020). In humans and macaque monkeys, a colliculo-pulvinar pathway has been found to have role in fearful visual signaling with the LA (Morris *et al.*, 1999; Rafal *et al.*, 2015). In mice, the caudal and medial parts of the pulvinar were placed in the LA-projecting thalamic region (Zhou *et al.*, 2017), identical with CR+LT territories, raising the possibility that the CR+LT→AMY route is responsible for affective visual processes in humans and primates, too.

2.4.4. A note on the direct and indirect CR+ thalamo-amygdala routes

Unlike CR-negative LT neurons, the CR+LT does not project to the primary auditory cortex (Au1), rather targets higher-order cortical regions such as the ventral secondary auditory cortex (AuV), the temporal association cortex (TeA) and the insular cortex, further demonstrating that these thalamic neurons are not directly involved in primary sensory processes. Sensory and higher-order cortical areas have been found to be crucial in long-term fear memory storage and retrieval (Sacco & Sacchetti, 2010) via a layer I-mediated disinhibitory process (Letzkus *et al.*, 2011). Since higher-order cortical regions are innervated

by CR+LT neurons, with layer I receiving the densest axonal arbor (Barsy & Kocsis *et al.*, 2020), this thalamic population is in ideal position to facilitate and maintain memory formation not only in the LA (recent and remote memory) but in the neocortex (remote memory) (Sacco & Sacchetti, 2010; Belén Pardi *et al.*, 2020), too.

Recalling LeDoux's theory about direct and indirect thalamic routes ('low road' and 'high road', respectively) to the amygdala (LeDoux, 1994), the CR+LT can be the cellular source of these parallel pathways. The direct CR+LT→AMY input can drive fast and robust evaluation and behavioral action in a dangerous situation, prior to any recognition. At the same time, sending collaterals to the AuV/TeA (which in turn provides cortical input to the LA), the CR+LT can provoke cortical processes that are slower but more precise and can involve conscious recognition.

Thus, the CR+LT population has a dual thalamic influence via the direct thalamo-amygdala and the indirect thalamo-cortico-amygdala route. Challenging the established idea of coincidence detection of separate CS and US inputs (Johnson *et al.*, 2009), we propose that CS+US-carrying CR+LT and cortical signals can spatially converge on amygdala neurons (Li *et al.*, 1996*b*). Summation of these inputs can then promote memory formation by driving NMDA-dependent plasticity at the LT input (Li *et al.*, 1996*b*; Weisskopf & LeDoux, 1999), gated by inhibitory processes (Wolff *et al.*, 2014; Asede *et al.*, 2015; Krabbe *et al.*, 2019). Moreover, considering that the lateral thalamo-amygdala pathway (dominantly formed by CR+LT cells) also potentiates reward learning via NMDA and/or AMPA-dependent changes (Tye *et al.*, 2008; Rich *et al.*, 2019), it is likely that these synaptic plasticity mechanisms are also present at the CR+LT→AMY inputs. Finally, this thalamic input can also interact with neuromodulatory pathways in the amygdala (Likhtik & Johansen, 2019).

Integrating all the above-noted cortical and subcortical signals, the amygdala can then quickly select the adaptive behavioral response to subsequent threat conditions (Headley *et al.*, 2019).

Furthermore, the CR+LT-targeted amygdalostriatal transition area (AStr), which has been previously suggested to participate in sensory processes during associative fear learning (LeDoux *et al.*, 1990), can also form a classical basal ganglia circuit with direct and indirect outputs through the *substantia nigra pars lateralis* and the lateral *globus pallidus*, respectively (Barsy & Kocsis *et al.*, 2020).

Taken together, the CR+LT population links, as a hub, sensory and motor events in affective behavioral actions through intra-amygdala, cortical and striatal circuits. Transferring associated signals, it in a unique position to develop and alter cue-evoked affective behavior.

2.5. Relevant publications of the author

2.5.1. **Peer-reviewed articles**

Publication supporting the theses

- Barsy, B.*, Kocsis, K.*, Magyar, A., Babiczky, Á., Szabó, M., Veres, M. J., Hillier, D., Ulbert, I., Yizhar, O., Mátyás, F. (2020): Associative and plastic thalamic signaling to the lateral amygdala controls fear behavior. *Nature Neuroscience*, *23(5):* pp. 625-637. https://doi.org/10.1038/s41593-020-0620-z

*shared first authorship

Other relevant publication

- Mátyás, F.*, Komlósi, G.*, Babiczky, Á., Kocsis, K., Barthó, P., Barsy, B., Dávid, C., Kanti, V., Porrero, C., Magyar, A., Szűcs, I., Clascá, F., Acsády, L. (2018): A highly collaterized thalamic cell type with arousal predicting activity serves as a key hub for graded state transitions in the forebrain. *Nature Neuroscience, 21(11):* pp. 1551-1562. https://doi.org/10.1038/s41593-018-0251-9

2.5.2. **Conference presentations**

2.5.2.1. **Selected first-author presentations**

- Kocsis, K., Magyar, A., Barsy, B., Babiczky, Á., Mátyás, F. (2019): Cell-type-specific interrogation of the mouse thalamus in aversive cue processing. Poster, Annual Meeting of the Hungarian Neuroscience Society, Debrecen, Hungary.
- Kocsis, K., Magyar, A., Barsy, B., Babiczky, Á., Jártó, F., Váncsodi, M., Berényi, A., Mátyás, F. (2019): The role of thalamic cells in amygdala-related processes. Poster, FENS-Hertie Winter School 2018 – Neural control of innate and instinctive behaviour, Obergurgl, Austria.
- Kocsis, K., Magyar, A., Barsy, B., Babiczky, Á., Kanti, V., Truka, L., Szabó, M., Jártó, F., Váncsodi, M., Berényi, A., Mátyás, F. (2018): Nucleus-specific interrogation of the mouse thalamus in aversive cue-processing. Poster, Annual meeting of the Society for Neuroscience (Neuroscience 2018), San Diego, CA, U.S.
- Kocsis, K., Magyar, A., Barsy, B., Babiczky, Á., Jártó, F., Váncsodi, M., Berényi, A., Mátyás, F. (2018) Calretinin-positive thalamic neurons convey distinct information in aversive learning. Poster, FENS Forum, Berlin, Germany.
- Kocsis, K., Barsy, B., Magyar, A., Babiczky, Á., Kanti, V., Horváth, M., Varga, K., Földes, T.A., Mátyás, F. (2017): Pathway-specific thalamic modulation of amygdalar circuits. Poster, Annual meeting of the Society for Neuroscience (Neuroscience 2017), Washington DC, U.S.
- Kocsis, K.*, Magyar, A.*, Barsy, B., Kanti, V., Babiczky, Á., Varga, K., Földes, T.A., Mátyás, F. (2017): Functional investigation of thalamoamygdalar circuits in freely behaving mice. Poster, FENS Regional Meeting, Pécs, Hungary.
- Kocsis, K., Barsy, B., Ulbert, I., Mátyás, F. (2016): Cell-type specific investigation of the thalamo-amygdala network in associative learning. Poster, FENS Forum, Copenhagen, Denmark.

2.5.2.2. **Selected co-author presentations**

- Kocsis, K.*, Barsy, B.*, Babiczky, Á., Szabó, M., Magyar., A., Váncsodi, M., Jártó, F., Berczik, J., Fehér, A, Hillier, D, Yizhar, O, Berényi, A, Mátyás F (2019): Thalamic control over amygdala function. Talk, Gordon Research Conference, 2019, Easton, MA, U.S.
- Barsy, B.*, Kocsis, K.*, Magyar, A., Babiczky, Á., Kanti, V., Varga, K., Hillier, D., Yizhar, O., Acsády, L., Mátyás, F. (2017): Anatomical and functional dissection of the thalamic amygdalar networks. Poster, Amygdala Function in Emotion, Cognition & Disease Gordon Research Conference, Easton, MA, U.S.

DOI:10.15774/PPKE.ITK.2022.002

The infrastructural basis of my second study was funded by the Hungarian Brain Research Program (2017-1.2.1-NKP-2017-00002 to Dr. Ferenc Mátyás and Prof. Dr. István Ulbert, KTIA-NAP-13-2-2015-0010 to F.M.) and by the National Research, Development and Innovation Office (FK124434 to F.M.). Dr. Ferenc Mátyás is a János Bolyai Research Fellow. My research was further supported by the New National Excellence Program of the Ministry for Innovation and Technology (ÚNKP-19-3-III-PPKE-68) as well as by the Széchenyi 2020 Human Resource Development Operational Program (EFOP-3.6.2-16-2017-00013 and 3.6.3-VEKOP-16-2017-00002).

DOI:10.15774/PPKE.ITK.2022.002

2.6. Outlook: future directions and potential for the study

2.6.1. CR+LT effect on intra-amygdala rhythmic activity

A fruitful follow-up on this study could be an exploration of how CR+ lateral thalamic inputs orchestrate the amygdala network so they can provide a robust processing of ethologically relevant signals and an efficient network output by recruiting and/or synchronizing transient or permanent cell ensembles. The CR+LT strongly shapes the activity of interneurons that are able to determine the configuration of the functional cellular network, and select the principal cells involved in coding. Fast-spiker interneurons are also bound (Wang & Buzsáki, 1996; Cardin *et al.*, 2009) to the synchronous and rhythmic cell firing underlying gamma activity (30-90 Hz, (Buzsáki & Wang, 2012)). Relatedly, electric stimulation of lateral thalamic cells (in PIL) induces gamma waves in the auditory cortex (Barth & MacDonald, 1996). With its period time, gamma provides an optimal time window for the potentiation of neuronal connections, thus serving the formation of memory traces (Buzsáki & Wang, 2012).

(Baso)lateral structures of the amygdala also generate fast rhythmic and synchronized activity (Pagano & Gault, 1964), which has prominent role in guiding affective behaviors necessary for survival. Salient sensory events and vigilance that increase efficiency in cue processing (Yerkes & Dodson, 1908), result in increased amygdala gamma activity (Headley & Paré, 2013; Courtin *et al.*, 2014; Feng *et al.*, 2019). Short-latency (20–30 ms) gamma-band synchronization in the human amygdala can be induced by threatening faces. This occurs after thalamic (10-20 ms) and prior to visual cortex (40-50 ms) activation (Luo *et al.*, 2007), suggesting an instrumental role for the direct thalamo-amygdala route.

Models have shown that gamma mediates competition between neuronal ensembles in stimulus selection (Borgers & Kopell, 2008), out of which only the ones with the strongest afferent drive involve local fast-spiking interneurons during each gamma cycle (De Almeida *et al.*, 2009). A tight connection of CR+LT to oscillation generating amygdala networks might heavily contribute to the selection of competing amygdala cell ensembles which can be further potentiated in affective learning and behavior (Courtin *et al.*, 2014; Amir *et al.*, 2018), both directly and through the interaction of the direct and indirect thalamo-amygdala routes.

2.6.2. Interaction of CR+LT aversive cue processing with hormonal activity

The lateral thalamic population has also got a unique connection to neuroendocrine networks, as (Barsy & Kocsis *et al.*, 2020) also showed that the CR+LT projects to the ventromedial hypothalamus. Furthermore, (Cservenak *et al.*, 2017) described a pathway from the PIL to the paraventricular hypothalamic nucleus (PVN) in mice, which is suggested to

trigger oxytocin release in lactating mothers by processing somatosensory information during pup exposure. This is in accordance with the study of (Tasaka *et al.*, 2020) showing that the temporal associative cortex (TeA) – a CR+LT target area (Barsy & Kocsis *et al.*, 2020) – plays a key role in discriminating ultrasonic pup vocalizations by mothers. These observations imply that behaviorally relevant cue processing of the CR+LT can potentially drive hormonal changes that can further enhance stimulus selection in its target regions.

2.6.3. CR+LT role in the subcortical processing of conspecific vocalizations

Another possible continuation of this research is the investigation of the CR+LT role in processing vocalizations and human language since these neurons potentially detect salient features in the acoustic stream. (Winer, 1984) showed that non-primary auditory thalamic regions, including the MGM, are relatively larger in humans, suggesting a role in speech processing. Moreover, as these 'belt' regions also integrate visual and reward cues (Komura *et al.*, 2005), thus behavioral context, they could also contribute to interpreting/ discriminating affective content from movements (e.g., gestures) related to vocal behavior (Bartlett, 2013).

I also propose that CR+LT neurons could enhance multisensory temporal binding on the neocortical level. First, they principally target layer I in higher-order cortices (Barsy & Kocsis *et al.*, 2020), where the apical dendrites of pyramidal neurons are located. (Jones, 2001) speculated that layer I-projecting thalamic 'matrix' neurons can involve multiple cortical regions to bind modalities into a coherent percept by coincidence detection with 'core' thalamic inputs in middle cortical layers. This can provoke oscillatory activity which is reinforced through corticothalamic projections. In addition, the PIL was shown to enhance ~40Hz cortical high-frequency synchronization (Barth & MacDonald, 1996), which was proposed as a binding mechanism in cortico-thalamo-cortico interactions (Llinás & Paré, 1991).

Overall, I pointed towards investigations with a focus on the CR+LT role in non-conscious affective cue processing. This population can be a potential target of modulation or molecular genetic characterization in affective disorders which involve enhanced or attenuated affective cue processing (Lake *et al.*, 2011; Eom *et al.*, 2017), impaired amygdala network activity (McFadyen *et al.*, 2020), and ultimately maladaptive behavioral responses. Therapeutic strategies aimed at treating implicit associative processes in affective disorders might consider altering the cue integration of this neuronal group.

References

Aboitiz F, Montiel J, Morales D & Concha M (2002). Evolutionary divergence of the reptilian and the mammalian brains: Considerations on connectivity and development. *Brain Res Rev* **39,** 141–153.

Alam MN, McGinty D & Szymusiak R (1996). Preoptic/anterior hypothalamic neurons: Thermosensitivity in wakefulness and non rapid eye movement sleep. *Brain Res* **718,** 76–82.

Alföldi P, Rubicsek G, Cserni G & Obál F (1990). Brain and core temperatures and peripheral vasomotion during sleep and wakefulness at various ambient temperatures in the rat. *Pflugers Arch* **417,** 336–341.

Almeida I, Soares SC & Castelo-Branco M (2015). The distinct role of the amygdala, superior colliculus and pulvinar in processing of central and peripheral snakes. *PLoS One* **10,** 1–21.

De Almeida L, Idiart M & Lisman JE (2009). A second function of gamma frequency oscillations: An E%-max winner-take-all mechanism selects which cells fire. *J Neurosci* **29,** 7497–7503.

Amir A, Headley DB, Lee S-C, Haufler D & Paré D (2018). Vigilance-Associated Gamma Oscillations Coordinate the Ensemble Activity of Basolateral Amygdala Neurons. *Neuron* **97,** 656-669.e7.

Andersen P, Andersson SA & Lomo T (1967). Some factors involved in the thalamic control of spontaneous barbiturate spindles. *J Physiol* **192,** 257–281.

Arenkiel BR, Peca J, Davison IG, Feliciano C, Deisseroth K, Augustine GJJ, Ehlers MD & Feng G (2007). In Vivo Light-Induced Activation of Neural Circuitry in Transgenic Mice Expressing Channelrhodopsin-2. *Neuron* **54,** 205–218.

Arrhenius S (1889). On the Reaction Velocity of the Inversion of Cane Sugar by Acids. *Zeitschrift für Phys Chemie*226–248.

Asede D, Bosch D, Lüthi A, Ferraguti F & Ehrlich I (2015). Sensory inputs to intercalated cells provide fear-learning modulated inhibition to the basolateral amygdala. *Neuron* **86,** 541–554.

B Katz RM (1965). The effect of temperature on the synaptic delay at the neuromuscular junction. *J Physiol* **181,** 656.

Baker MA & Hayward JN (1967). Autonomic Basis for the Rise in Brain Temperature during Paradoxical Sleep. *Science (80-)* **157,** 1586–1588.

Barsy B, Kocsis K, Magyar A, Babiczky Á, Szabó M, Veres JM, Hillier D, Ulbert I, Yizhar O & Mátyás F (2020). Associative and plastic thalamic signaling to the lateral amygdala controls fear behavior. *Nat Neurosci* **23,** 625–637.

Barth DS & MacDonald KD (1996). Thalamic modulation of high-frequency oscillating potentials in auditory cortex. *Nature* **383,** 78–81.

Bartho P, Curto C, Luczak A, Marguet SL & Harris KD (2009). Population coding of tone stimuli in auditory cortex: Dynamic rate vector analysis. *Eur J Neurosci* **30,** 1767–1778.

Barthó P, Hirase H, Monconduit L, Zugaro M, Harris KD & Buzsáki G (2004). Characterization of neocortical principal cells and interneurons by network interactions and extracellular features. *J Neurophysiol* **92,** 600–608.

Barthó P, Slézia A, Mátyás F, Faradzs-Zade L, Ulbert I, Harris KD & Acsády L (2014). Ongoing network state controls the length of sleep spindles via inhibitory activity. *Neuron* **82,** 1367–1379.

Bartlett EL (2013). The organization and physiology of the auditory thalamus and its role in processing acoustic features important for speech perception. *Brain Lang* **126,** 29–48.

Bartlett EL, Stark JM, Guillery RW & Smith PH (2000). Comparison of the fine structure of cortical and collicular terminals in the rat medial geniculate body. *Neuroscience* **100,** 811–828.

Belén Pardi M, Vogenstahl J, Dalmay T, Spanò T, Pu DL, Naumann LB, Kretschmer F, Sprekeler H & Letzkus JJ (2020). A thalamocortical top-down circuit for associative memory. *Science (80-)* **370,** 844–848.

Bickford ME (2015). Thalamic circuit diversity: Modulation of the driver/modulator framework. *Front Neural Circuits* **9,** 1–8.

Blair HT, Schafe GE, Bauer EP, Rodrigues SM & LeDoux JE (2001). Synaptic plasticity in the lateral amygdala: a cellular hypothesis of fear conditioning. *Learn Mem* **8,** 229–242.

Blasiak T, Zawadzki A & Lewandowski MH (2013). Infra-Slow Oscillation (ISO) of the Pupil Size of Urethane-Anaesthetised Rats ed. Dickson CT. *PLoS One* **8,** e62430.

Bódizs R, Gombos F, Ujma PP & Kovács I (2014). Sleep spindling and fluid intelligence across adolescent development: sex matters. *Front Hum Neurosci* **8,** 952.

Bordi F & LeDoux JE (1994*a*). Response properties of single units in areas of rat auditory thalamus that project to the amygdala - II. Cells receiving convergent auditory and somatosensory inputs and cells antidromically activated by amygdala stimulation. *Exp Brain Res* **98,** 275–286.

Bordi F & LeDoux JE (1994*b*). Response properties of single units in areas of rat auditory thalamus that

project to the amygdala - I. Acoustic discharge patterns and frequency receptive fields. *Exp Brain Res* **98,** 261–274.
Borgers C & Kopell NJ (2008). Gamma oscillations and stimulus selection. *Neural Comput* **20,** 383–414.
Brooks VB (1983). Study of brain function by local, reversible cooling. **95,** 1–109.
Butler AB (1994). The evolution of the dorsal thalamus of jawed vertebrates, including mammals: Cladistic analysis and a new hypothesis. *Brain Res Rev* **19,** 29–65.
Buzsáki G & Wang X-J (2012). Mechanisms of Gamma Oscillations. *Annu Rev Neurosci* **35,** 203–225.
Campeau S & Davis M (1995). Involvement of subcortical and cortical afferents to the lateral nucleus of the amygdala in fear conditioning measured with fear-potentiated startle in rats trained concurrently with auditory and visual conditioned stimuli. *J Neurosci* **15,** 2312–2327.
Cannon WB (1929). *Bodily Changes in Pain, Hunger, Fear and Rage; An Account of Recent Researches into the Function of Emotional Excitement*, 2nd edn. New York; London: D. Appleton and Company.
Cardin JA, Carlén M, Meletis K, Knoblich U, Zhang F, Deisseroth K, Tsai L-H & Moore CI (2009). Driving fast-spiking cells induces gamma rhythm and controls sensory responses. *Nature* **459,** 663–667.
Clascá F, Rubio-Garrido P & Jabaudon D (2012). Unveiling the diversity of thalamocortical neuron subtypes. *Eur J Neurosci* **35,** 1524–1532.
Clement EA, Richard A, Thwaites M, Ailon J, Peters S & Dickson CT (2008). Cyclic and sleep-like spontaneous alternations of brain state under urethane anaesthesia. *PLoS One* **3,** e2004.
Clugnet MC & LeDoux JE (1990). Synaptic plasticity in fear conditioning circuits: Induction of LTP in the lateral nucleus of the amygdala by stimulation of the medial geniculate body. *J Neurosci* **10,** 2818–2824.
Coleman JR & Clerici WJ (1987). Sources of projections to subdivisions of the inferior colliculus in the rat. *J Comp Neurol* **262,** 215–226.
Coleshaw SR, Van Someren RN, Wolff AH, Davis HM & Keatinge WR (1983). Impaired memory registration and speed of reasoning caused by low body temperature. *J Appl Physiol* **55,** 27–31.
Collins KJ, Exton-Smith AN & Dore C (1981). Urban hypothermia: preferred temperature and thermal perception in old age. *BMJ* **282,** 175–177.
Courtin J, Karalis N, Gonzalez-Campo C, Wurtz H & Herry C (2014). Persistence of amygdala gamma oscillations during extinction learning predicts spontaneous fear recovery. *Neurobiol Learn Mem* **113,** 82–89.
Cruikshank SJ, Edeline J & Weinberger NM (1992). Stimulation at a Site of Auditory- Somatosensory Convergence in the Medial Geniculate Nucleus Is an Effective Unconditioned Stimulation at a Site of Auditory-Somatosensory Convergence in the Medial Geniculate Nucleus Is an Effective Unconditioned Stim. **106,** 471–483.
Crunelli V, Larincz ML, Connelly WM, David F, Hughes SW, Lambert RC, Leresche N & Errington AC (2018). Dual function of thalamic low-vigilance state oscillations: Rhythm-regulation and plasticity. *Nat Rev Neurosci* **19,** 107–118.
Csernai M, Borbély S, Kocsis K, Burka D, Fekete Z, Balogh V, Káli S, Emri Z & Barthó P (2019). Dynamics of sleep oscillations is coupled to brain temperature on multiple scales. *J Physiol* **597,** 4069–4086.
Cservenak M, Keller D, Kis V, Fazekas EA, Ollos H, Leko AH, Szabo ER, Renner E, Usdin TB, Palkovits M & Dobolyi A (2017). A thalamo-hypothalamic pathway that activates oxytocin neurons in social contexts in female rats. *Endocrinology* **158,** 335–348.
Darwin C (1872). *The expression of the emotions in man and animals.* John Murray, London. Available at: http://content.apa.org/books/10001-000.
Deboer T (1998). Brain temperature dependent changes in the electroencephalogram power spectrum of humans and animals. *J Sleep Res* **7,** 254–262.
Deboer T & Tobler I (1995). Temperature dependence of EEG frequencies during natural hypothermia. *Brain Res* **670,** 153–156.
Delgado JM & Hanai T (1966). Intracerebral temperatures in free-moving cats. *Am J Physiol* **211,** 755–769.
Demirhan A, Kaymaz M, AhIska R & Güler I (2010). A survey on application of quantitative methods on analysis of brain parameters changing with temperature. *J Med Syst* **34,** 1059–1071.
Dijk DJ & Czeisler C a (1995). Contribution of the circadian pacemaker and the sleep homeostat to sleep propensity, sleep structure, electroencephalographic slow waves, and sleep spindle activity in humans. *J Neurosci* **15,** 3526–3538.
Do-Monte FH, Quiñones-Laracuente K & Quirk GJ (2015). A temporal shift in the circuits mediating retrieval of fear memory. *Nature* **519,** 460–463.
Driver HS, Dijk DJ, Werth E, Biedermann K & Borbely AA (1996). Sleep and the sleep

electroencephalogram across the menstrual cycle in young healthy women. *J Clin Endocrinol Metab* **81,** 728–735.
Edeline J-M & Weinberger NM (1992). Associative retuning in the thalamic source of input to the amygdala and auditory cortex: Receptive field plasticity in the medial division of the medial geniculate body. *Behav Neurosci* **106,** 81–105.
Eom TY, Bayazitov IT, Anderson K, Yu J & Zakharenko SS (2017). Schizophrenia-Related Microdeletion Impairs Emotional Memory through MicroRNA-Dependent Disruption of Thalamic Inputs to the Amygdala. *Cell Rep* **19,** 1532–1544.
Fadok JP, Markovic M, Tovote P & Lüthi A (2018). New perspectives on central amygdala function. *Curr Opin Neurobiol* **49,** 141–147.
Fanselow MS & Lester LS (1988). A functional behavioristic approach to aversely motivated behavior: predatory imminence as a determinate of the topology of defensive behavior. In *Evolution and learning*, pp. 185–211. Hillsdale, NJ: Erlbaum.
Fekete Z, Csernai M, Kocsis K, Horváth ÁC, Pongrácz A & Barthó P (2017). Simultaneous in vivo recording of local brain temperature and electrophysiological signals with a novel neural probe. *J Neural Eng* **14,** 034001.
Feld GB & Born J (2017). Sculpting memory during sleep: concurrent consolidation and forgetting. *Curr Opin Neurobiol* **44,** 20–27.
Feng F, Headley DB, Amir A, Kanta V, Chen Z, Paré D & Nair SS (2019). Gamma Oscillations in the Basolateral Amygdala: Biophysical Mechanisms and Computational Consequences. *eneuro* **6,** ENEURO.0388-18.2018.
Fernandez LMJ & Lüthi A (2020). Sleep spindles: Mechanisms and functions. *Physiol Rev* **100,** 805–868.
Fogel SM, Smith CT & Cote KA (2007). Dissociable learning-dependent changes in REM and non-REM sleep in declarative and procedural memory systems. *Behav Brain Res* **180,** 48–61.
Fregly MJ, Iampietro PF & Otis AB (1961). Effect of hypothyroidism on heat production and loss during acute exposure to cold. *J Appl Physiol* **16,** 127–132.
Gauriau C & Bernard J-F (2004). A comparative reappraisal of projections from the superficial laminae of the dorsal horn in the rat: The forebrain. *J Comp Neurol* **468,** 24–56.
Gaynor KM, Brown JS, Middleton AD, Power ME & Brashares JS (2019). Landscapes of Fear: Spatial Patterns of Risk Perception and Response. *Trends Ecol Evol* **34,** 355–368.
Grewe BF, Gründemann J, Kitch LJ, Lecoq JA, Parker JG, Marshall JD, Larkin MC, Jercog PE, Grenier F, Li JZ, Lüthi A & Schnitzer MJ (2017). Neural ensemble dynamics underlying a long-term associative memory. *Nature* **543,** 670–675.
Gründemann J (2021). Distributed coding in auditory thalamus and basolateral amygdala upon associative fear learning. *Curr Opin Neurobiol* **67,** 183–189.
Guyton A & Hall J (2005). *Textbook of Medical Physiology*, 11th edn. Saunders.
Halverson HE & Freeman JH (2006). Medial Auditory Thalamic Nuclei Are Necessary for Eyeblink Conditioning. *Behav Neurosci* **120,** 880–887.
Hamilton CL (1963). Hypothalamic temperature records of a monkey. *Proc Soc Exp Biol Med* **112,** 55–57.
Han J-H, Yiu AP, Cole CJ, Hsiang H-L, Neve RL & Josselyn SA (2008). Increasing CREB in the auditory thalamus enhances memory and generalization of auditory conditioned fear. *Learn Mem* **15,** 443–453.
Han S, Soleiman MT, Soden ME, Zweifel LS & Palmiter RD (2015). Elucidating an Affective Pain Circuit that Creates a Threat Memory. *Cell* **162,** 363–374.
Hayashi H, Sumino R & Sessle BJ (1984). Functional organization of trigeminal subnucleus interpolaris: nociceptive and innocuous afferent inputs, projections to thalamus, cerebellum, and spinal cord, and descending modulation from periaqueductal gray. *J Neurophysiol* **51,** 890–905.
Hayward J & Baker M (1969). A comparative study of the role of the cerebral arterial blood in the regulation of brain temperature in five mammals. *Brain Res* **16,** 417–440.
He J (2002). OFF responses in the auditory thalamus of the guinea pig. *J Neurophysiol* **88,** 2377–2386.
Headley DB, Kanta V, Kyriazi P & Paré D (2019). Embracing Complexity in Defensive Networks. *Neuron* **103,** 189–201.
Headley DB & Paré D (2013). In sync: gamma oscillations and emotional memory. *Front Behav Neurosci* **7,** 170.
Hebert J, Lust A, Fuller A, Maloney SK, Mitchell D & Mitchell G (2008). Thermoregulation in pronghorn antelope (Antilocapra americana, Ord) in winter. *J Exp Biol* **211,** 749–756.
Herreras O (2016). Local field potentials: Myths and misunderstandings. *Front Neural Circuits* **10,** 1–16.
Hicks TP, Stark CA & Fletcher WA (1986). Origins of afferents to visual suprageniculate nucleus of the

cat. *J Comp Neurol* **246,** 544–554.
Hoagland H (1936). Temperature Characteristics of the “Berger Rhythm” in Man. *Science (80-)* **83,** 84–85.
James WO (1953). *Plant Respiration*. Clarendon Press, Oxford, U. K.
Johansen JP, Tarpley JW, LeDoux JE & Blair HT (2010). Neural substrates for expectation-modulated fear learning in the amygdala and periaqueductal gray. *Nat Neurosci* **13,** 979–986.
Johnson LR, Ledoux JE & Doyère V (2009). Hebbian reverberations in emotional memory micro circuits. *Front Neurosci* **3,** 198–205.
Jones EG (1998). A new view of specific and nonspecific thalamocortical connections. *Adv Neurol* **77,** 49–71; discussion 72-3.
Jones EG (2001). The thalamic matrix and thalamocortical synchrony. *Trends Neurosci* **24,** 595-601.
Kawamura H & Sawyer CH (1965). Elevation in brain temperature during paradoxical sleep. *Science* **150,** 912–913.
Kim EJ, Horovitz O, Pellman BA, Tan LM, Li Q, Richter-Levin G & Kim JJ (2013). Dorsal periaqueductal gray-amygdala pathway conveys both innate and learned fear responses in rats. *Proc Natl Acad Sci U S A* **110,** 14795–14800.
King AJ (2004). The superior colliculus. *Curr Biol* **14,** R335–R338.
Kiyatkin E a (2010). Brain temperature homeostasis: physiological fluctuations and pathological shifts. *Front Biosci* **15,** 73–92.
Kiyatkin EA, Brown PL & Wise RA (2002). Brain temperature fluctuation: A reflection of functional neural activation. *Eur J Neurosci* **16,** 164–168.
Komura Y, Tamura R, Uwano T, Nishijo H & Ono T (2005). Auditory thalamus integrates visual inputs into behavioral gains. *Nat Neurosci* **8,** 1203–1209.
Kovalzon VM (1973). Brain temperature variations during natural sleep and arousal in white rats. *Physiol Behav* **10,** 667–670.
Kovalzon VM & Mukhametov LM (1983). Temperature fluctuations of the dolphin brain corresponding to unihemispheric slow-wave sleep. *J Evol Biochem Physiol* **18,** 222–224.
Krabbe S, Paradiso E, D’Aquin S, Bitterman Y, Courtin J, Xu C, Yonehara K, Markovic M, Müller C, Eichlisberger T, Gründemann J, Ferraguti F & Lüthi A (2019). Adaptive disinhibitory gating by VIP interneurons permits associative learning. *Nat Neurosci* **22,** 1834–1843.
Krauchi K & Deboer T (2010). The interrelationship between sleep regulation and thermoregulation. *Front Biosci (Landmark Ed* **15,** 604–625.
Krosigk M Von, Bal T & Mccormick DA (1993). Cellular Mechanisms of a Synchronized Oscillation in the Thalamus. *Science (80-)* **261,** 361–364.
Lake AJ, Baskin-Sommers AR, Li W, Curtin JJ & Newman JP (2011). Evidence for unique threat-processing mechanisms in psychopathic and anxious individuals. *Cogn Affect Behav Neurosci* **11,** 451–462.
LaManna JC, McCracken KA, Patil M & Prohaska OJ (1989). Stimulus-activated changes in brain tissue temperature in the anesthetized rat. *Metab Brain Dis* **4,** 225–237.
Lanuza E, Moncho-Bogani J & LeDoux JE (2008). Unconditioned stimulus pathways to the amygdala: Effects of lesions of the posterior intralaminar thalamus on foot-shock-induced c-Fos expression in the subdivisions of the lateral amygdala. *Neuroscience* **155,** 959–968.
Lanuza E, Nader K & LeDoux JE (2004). Unconditioned stimulus pathways to the amygdala: effects of posterior thalamic and cortical lesions on fear conditioning. *Neuroscience* **125,** 305–315.
Larson MA, McHaffie JG & Stein BE (1987). Response properties of nociceptive and low-threshold mechanoreceptive neurons in the hamster superior colliculus. *J Neurosci* **7,** 547–564.
Lecci S, Fernandez LMJ, Weber FD, Cardis R, Chatton J-Y, Born J & Lüthi A (2017). Coordinated infraslow neural and cardiac oscillations mark fragility and offline periods in mammalian sleep. *Sci Adv* **3,** e1602026.
LeDoux JE (1994). Emotion, Memory and the Brain. *Sci Am* **270,** 50–57.
LeDoux JE, Farb C & Ruggiero D a (1990). Topographic organization of neurons in the acoustic thalamus that project to the amygdala. *J Neurosci* **10,** 1043–1054.
LeDoux JE, Ruggiero DA, Forest R, Stornetta R & Reis DJ (1987). Topographic organization of convergent projections to the thalamus from the inferior colliculus and spinal cord in the rat. *J Comp Neurol* **264,** 123–146.
LeDoux JE, Sakaguchi A & Reis DJ (1984). Subcortical efferent projections of the medial geniculate nucleus mediate emotional responses conditioned to acoustic stimuli. *J Neurosci* **4,** 683–698.
Lee JCF, Callaway JC & Foehring RC (2005). Effects of Temperature on Calcium Transients and Ca 2+ -Dependent Afterhyperpolarizaions in Neocortical Pyramidal Neurons. *J Neurophysiol* **93,** 2012–2020.

Łęski S, Pettersen KH, Tunstall B, Einevoll GT, Gigg J & Wójcik DK (2011). Inverse current source density method in two dimensions: Inferring neural activation from multielectrode recordings. *Neuroinformatics* **9,** 401–425.

Letzkus JJ, Wolff SBE, Meyer EMM, Tovote P, Courtin J, Herry C & Lüthi A (2011). A disinhibitory microcircuit for associative fear learning in the auditory cortex. *Nature* **480,** 331–335.

Li XF, Armony JL & LeDoux JE (1996*a*). GABAA and GABAB receptors differentially regulate synaptic transmission in the auditory thalamo-amygdala pathway: an in vivo microiontophoretic study and a model. *Synapse* **24,** 115–124.

Li XF, Stutzmann GE & LeDoux JE (1996*b*). Convergent but temporally separated inputs to lateral amygdala neurons from the auditory thalamus and auditory cortex use different postsynaptic receptors: in vivo intracellular and extracellular recordings in fear conditioning pathways. *Learn Mem* **3,** 229–242.

Likhtik E & Johansen JP (2019). Neuromodulation in circuits of aversive emotional learning. *Nat Neurosci* **22,** 1586–1597.

Linke R (1999). Differential projection patterns of superior and inferior collicular neurons onto posterior paralaminar nuclei of the thalamus surrounding the medial geniculate body in the rat. *Eur J Neurosci* **11,** 187–203.

Linke R, De Lima AD, Schwegler H & Pape HC (1999). Direct synaptic connections of axons from superior colliculus with identified thalamo-amygdaloid projection neurons in the rat: possible substrates of a subcortical visual pathway to the amygdala. *J Comp Neurol* **403,** 158–170.

Linke R & Schwegler H (2000). Convergent and complementary projections of the caudal paralaminar thalamic nuclei to rat temporal and insular cortex. *Cereb Cortex* **10,** 753–771.

Lipshetz B, Khasabov SG, Truong H, Netoff TI, Simone DA & Giesler GJ (2018). Responses of thalamic neurons to itch- and pain-producing stimuli in rats. *J Neurophysiol* **120,** 1119–1134.

Liu YJ, Wang Q & Li B (2011). Neuronal responses to looming objects in the superior colliculus of the cat. *Brain Behav Evol* **77,** 193–205.

Llinás RR & Paré D (1991). Of dreaming and wakefulness. *Neuroscience* **44,** 521–535.

Lopes G, Bonacchi N, Frazão J, Neto JP, Atallah B V., Soares S, Moreira L, Matias S, Itskov PM, Correia PA, Medina RE, Calcaterra L, Dreosti E, Paton JJ & Kampff AR (2015). Bonsai: an event-based framework for processing and controlling data streams. *Front Neuroinform* **9,** 7.

Lőrincz ML, Geall F, Bao Y, Crunelli V & Hughes SW (2009). ATP-dependent infra-slow (<0.1 Hz) oscillations in thalamic networks. *PloS One* **4,** e4447.

Lu E, Llano DA & Sherman SM (2009). Different distributions of calbindin and calretinin immunostaining across the medial and dorsal divisions of the mouse medial geniculate body. *Hear Res* **257,** 16–23.

Luo Q, Holroyd T, Jones M, Hendler T & Blair J (2007). Neural dynamics for facial threat processing as revealed by gamma band synchronization using MEG. *Neuroimage* **34,** 839–847.

Lyamin OI, Kosenko PO, Korneva SM, Vyssotski AL, Mukhametov LM & Siegel JM (2018). Fur Seals Suppress REM Sleep for Very Long Periods without Subsequent Rebound. *Curr Biol*1–6.

Lyamin OI, Manger PR, Ridgway SH, Mukhametov LM & Siegel JM (2008). Cetacean sleep: An unusual form of mammalian sleep. *Neurosci Biobehav Rev* **32,** 1451–1484.

Mahn M, Prigge M, Ron S, Levy R & Yizhar O (2016). Biophysical constraints of optogenetic inhibition at presynaptic terminals. *Nat Neurosci* **19,** 554–556.

Malkinson TJ, Cooper KE & Veale WL (1988). Physiological changes during thermoregulation and fever in urethan-anesthetized rats. *Am J Physiol Integr Comp Physiol* **255,** R73–R81.

Manoach DS, Pan JQ, Purcell SM & Stickgold R (2016). Reduced Sleep Spindles in Schizophrenia: A Treatable Endophenotype That Links Risk Genes to Impaired Cognition? *Biol Psychiatry* **80,** 599–608.

Mantini D, Perrucci MG, Del Gratta C, Romani GL & Corbetta M (2007). Electrophysiological signatures of resting state networks in the human brain. *Proc Natl Acad Sci* **104,** 13170–13175.

Marín O (2012). Interneuron dysfunction in psychiatric disorders. *Nat Rev Neurosci* **13,** 107–120.

Marshall L (2004). Transcranial Direct Current Stimulation during Sleep Improves Declarative Memory. *J Neurosci* **24,** 9985–9992.

Massopust LC, Wolin LR & Meder J (1965). Spontaneous electrical activity of the brain in hibernators and nonhibernators during hypothermia. *Exp Neurol* **12,** 25–32.

Mátyás F, Komlósi G, Babiczky Á, Kocsis K, Barthó P, Barsy B, Dávid C, Kanti V, Porrero C, Magyar A, Szűcs I, Clasca F & Acsády L (2018). A highly collateralized thalamic cell type with arousal-predicting activity serves as a key hub for graded state transitions in the forebrain. *Nat Neurosci* **21,** 1551–1562.

Mazor O & Laurent G (2005). Transient dynamics versus fixed points in odor representations by locust

antennal lobe projection neurons. *Neuron* **48,** 661–673.
McEchron MD, McCabe PM, Green EJ, Llabre MM & Schneiderman N (1995). Simultaneous single unit recording in the medial nucleus of the medial geniculate nucleus and amygdaloid central nucleus throughout habituation, acquisition, and extinction of the rabbit's classically conditioned heart rate. *Brain Res* **682,** 157–166.
McElligott JG & Melzack R (1967). Localized Thermal Changes Evoked in the Brain by Visual and Auditory Stimulation. *Exp Neurol* **17,** 293–312.
McFadyen J, Dolan RJ & Garrido MI (2020). The influence of subcortical shortcuts on disordered sensory and cognitive processing. *Nat Rev Neurosci* **21,** 264–276.
Mellergård P (1995). Intracerebral temperature in neurosurgical patients: intracerebral temperature gradients and relationships to consciousness level. *Surg Neurol* **43,** 91–95.
Michenfelder JD & Milde JH (1991). The relationship among canine brain temperature, metabolism, and function during hypothermia. *Anesthesiology* **75,** 130–136.
Mikics É, Barsy B, Barsvári B & Haller J (2005). Behavioral specificity of non-genomic glucocorticoid effects in rats: Effects on risk assessment in the elevated plus-maze and the open-field. *Horm Behav* **48,** 152–162.
Mitchell G, Fuller A, Maloney SK, Rump N & Mitchell D (2006). Guttural pouches, brain temperature and exercise in horses. *Biol Lett* **2,** 475–477.
Morin A, Doyon J, Dostie V, Barakat M, Hadj Tahar A, Korman M, Benali H, Karni A, Ungerleider LG & Carrier J (2008). Motor sequence learning increases sleep spindles and fast frequencies in post-training sleep. *Sleep* **31,** 1149–1156.
Morris JS, Ohman A & Dolan RJ (1999). A subcortical pathway to the right amygdala mediating "unseen" fear. *Proc Natl Acad Sci U S A* **96,** 1680–1685.
Nabavi S, Fox R, Proulx CD, Lin JY, Tsien RY & Malinow R (2014). Engineering a memory with LTD and LTP. *Nature* **511,** 348–352.
Ngo HV V, Martinetz T, Born J & Mölle M (2013). Auditory closed-loop stimulation of the sleep slow oscillation enhances memory. *Neuron* **78,** 545–553.
Nikolić D, Fries P & Singer W (2013). Gamma oscillations: precise temporal coordination without a metronome. *Trends Cogn Sci* **17,** 54–55.
Obál F, Rubicsek G, Alföldi P & Sáry G (1985). Changes in the brain and core temperatures in relation to the various arousal states in rats in the light and dark periods of the day. *Pflügers Arch Eur J Physiol* **404,** 73–79.
Obradovich N, Migliorini R, Mednick SC & Fowler JH (2017). Nighttime temperature and human sleep loss in a changing climate. *Sci Adv* **3,** 1–7.
Pagano RR & Gault FP (1964). Amygdala activity: A central measure of arousal. *Electroencephalogr Clin Neurophysiol* **17,** 255–260.
Pagliardini S, Gosgnach S & Dickson CT (2013). Spontaneous Sleep-Like Brain State Alternations and Breathing Characteristics in Urethane Anesthetized Mice ed. Foffani G. *PLoS One* **8,** e70411.
Pape H-C & Pare D (2010). Plastic Synaptic Networks of the Amygdala for the Acquisition, Expression, and Extinction of Conditioned Fear. *Physiol Rev* **90,** 419–463.
Parmeggiani PL (1977). Thermoregulation during sleep. *Riv Neurol* **47,** 485–491.
Parri HR & Crunelli V (2001). Pacemaker calcium oscillations in thalamic astrocytes *in situ*. *Neuroreport* **12,** 3897–3900.
Partridge LD & Connor JA (1978). A mechanism for minimizing temperature effects on repetitive firing frequency. *Am J Physiol* **234,** C155-61.
Paxinos G & Franklin KBJ (2003). *The Mouse Brain in Stereotaxic Coordinates*. Academic Press.
Penzo MA, Robert V, Tucciarone J, De Bundel D, Wang M, Van Aelst L, Darvas M, Parada LF, Palmiter RD, He M, Huang ZJ & Li B (2015). The paraventricular thalamus controls a central amygdala fear circuit. *Nature* **519,** 455–459.
Peterfi Z, Makara GB, Obál F & Krueger JM (2009). The anterolateral projections of the medial basal hypothalamus affect sleep. *Am J Physiol Integr Comp Physiol* **296,** R1228–R1238.
Pettersen KH, Devor A, Ulbert I, Dale AM & Einevoll GT (2006). Current-source density estimation based on inversion of electrostatic forward solution: Effects of finite extent of neuronal activity and conductivity discontinuities. *J Neurosci Methods* **154,** 116–133.
Pouille F & Scanziani M (2001). Enforcement of temporal fidelity in pyramidal cells by somatic feed-forward inhibition. *Science (80-)* **293,** 1159–1163.
Quirk GJ, Armony JL & LeDoux JE (1997). Fear Conditioning Enhances Different Temporal Components of Tone-Evoked Spike Trains in Auditory Cortex and Lateral Amygdala. *Neuron* **19,** 613–624.
Quirk GJ, Repa C & LeDoux JE (1995). Fear conditioning enhances short-latency auditory responses of lateral amygdala neurons: parallel recordings in the freely behaving rat. *Neuron* **15,** 1029–1039.

Rafal RD, Koller K, Bultitude JH, Mullins P, Ward R, Mitchell AS & Bell AH (2015). Connectivity between the superior colliculus and the amygdala in humans and macaque monkeys: virtual dissection with probabilistic DTI tractography. *J Neurophysiol* **114,** 1947–1962.

Raymann RJEM, Swaab DF & Van Someren EJW (2008). Skin deep: Enhanced sleep depth by cutaneous temperature manipulation. *Brain* **131,** 500–513.

Reite ML & Pegram G V (1968). Cortical temperature during paradoxical sleep in the monkey. *Electroencephalogr Clin Neurophysiol* **25,** 36–41.

Rich MT, Huang YH & Torregrossa MM (2019). Plasticity at Thalamo-amygdala Synapses Regulates Cocaine-Cue Memory Formation and Extinction. *Cell Rep* **26,** 1010-1020.e5.

Romanski LM & LeDoux JE (1992). Equipotentiality of thalamo-amygdala and thalamo-cortico-amygdala circuits in auditory fear conditioning. *J Neurosci* **12,** 4501–4509.

Rosanova M & Ulrich D (2005). Pattern-specific associative long-term potentiation induced by a sleep spindle-related spike train. *J Neurosci* **25,** 9398–9405.

Rossant C, Kadir SN, Goodman DFM, Schulman J, Hunter MLD, Saleem AB, Grosmark A, Belluscio M, Denfield GH, Ecker AS, Tolias AS, Solomon S, Buzsáki G, Carandini M & Harris KD (2016). Spike sorting for large, dense electrode arrays. *Nat Neurosci* **19,** 634–641.

Rossi S (2001). Brain temperature, body core temperature, and intracranial pressure in acute cerebral damage. *J Neurol Neurosurg Psychiatry* **71,** 448–454.

Ryugo DK & Weinberger NM (1978). Differential plasticity of morphologically distinct neuron populations in the medial geniculate body of the cat during classical conditioning. *Behav Biol* **22,** 275–301.

Sacco T & Sacchetti B (2010). Role of secondary sensory cortices in emotional memory storage and retrieval in rats. *Science (80-)* **329,** 649–656.

Sahibzada N, Dean P & Redgrave P (1986). Movements resembling orientation or avoidance elicited by electrical stimulation of the superior colliculus in rats. *J Neurosci* **6,** 723–733.

Satoh T (1968). Brain temperature of the cat during sleep. *Arch Ital Biol* **106,** 73–82.

Schmitt B, Jenni OG, Bauersfeld U, Schüpbach R & Schmid ER (2002). Spindle activity in children during cardiac surgery and hypothermic cardiopulmonary bypass. *J Clin Neurophysiol* **19,** 547–552.

Schwaller B, Meyer M & Schiffmann S (2002). “New” functions for “old” proteins: The role of the calcium-binding proteins calbindin D-28k, calretinin and parvalbumin, in cerebellar physiology. Studies with knockout mice. *Cerebellum* **1,** 241–258.

Serota HM & Gerard RW (1938). Localized thermal changes in the cat’s brain. *J Neurophysiol* **1,** 115–124.

Sherman SM & Guillery RW (1998). On the actions that one nerve cell can have on another: Distinguishing “drivers” from “modulators.” *Proc Natl Acad Sci U S A* **95,** 7121–7126.

Shi C & Davis M (1999). Pain Pathways Involved in Fear Conditioning Measured with Fear-Potentiated Startle: Lesion Studies. *J Neurosci* **19,** 420–430.

Siegelbaum SA & Kandel ER (1991). Learning-related synaptic plasticity: LTP and LTD. *Curr Opin Neurobiol* **1,** 113–120.

Smith PH, Bartlett EL & Kowalkowski A (2006). Unique combination of anatomy and physiology in cells of the rat paralaminar thalamic nuclei adjacent to the medial geniculate body. *J Comp Neurol* **496,** 314–334.

Smith PH, Bartlett EL & Kowalkowski A (2007). Cortical and collicular inputs to cells in the rat paralaminar thalamic nuclei adjacent to the medial geniculate body. *J Neurophysiol* **98,** 681–695.

Van Someren EJW (2000). More Than a Marker: Interaction Between the Circadian Regulation of Temperature and Sleep, Age-Related Changes, and Treatment Possibilities. *Chronobiol Int* **17,** 313–354.

Van Someren EJW (2004). Sleep propensity is modulated by circadian and behavior-induced changes in cutaneous temperature. *J Therm Biol* **29,** 437–444.

Stein BE & Dixon JP (1978). Superior colliculus cells respond to noxious stimuli. *Brain Res* **158,** 65–73.

Steriade M, Deschenes M, Domich L & Mulle C (1985). Abolition of spindle oscillations in thalamic neurons disconnected from nucleus reticularis thalami. *J Neurophysiol* **54,** 1473–1497.

Steriade M, McCormick DA & Sejnowski TJ (1993). Thalamocortical oscillations in the sleeping and aroused brain. *Science* **262,** 679–685.

Sund-Levander M, Forsberg C & Wahren LK (2002). Normal oral, rectal, tympanic and axillary body temperature in adult men and women: a systematic literature review. *Scand J Caring Sci* **16,** 122–128.

Tamietto M & De Gelder B (2010). Neural bases of the non-conscious perception of emotional signals. *Nat Rev Neurosci* **11,** 697–709.

Tang LS, Taylor AL, Rinberg A & Marder E (2012). Robustness of a Rhythmic Circuit to Short- and

Long-Term Temperature Changes. *J Neurosci* **32,** 10075–10085.
Tasaka G ichi, Feigin L, Maor I, Groysman M, DeNardo LA, Schiavo JK, Froemke RC, Luo L & Mizrahi A (2020). The Temporal Association Cortex Plays a Key Role in Auditory-Driven Maternal Plasticity. *Neuron* **107,** 566-579.e7.
Taylor JA, Hasegawa M, Benoit CM, Freire JA, Theodore M, Ganea DA, Innocenti SM, Lu T & Gründemann J (2021). Single cell plasticity and population coding stability in auditory thalamus upon associative learning. *Nat Commun* **12,** 1–14.
Thompson SM, Masukawa LM & Prince DA (1985). Temperature dependence of intrinsic membrane properties and synaptic potentials in hippocampal CA1 neurons in vitro. *J Neurosci* **5,** 817–824.
Trübel HK, Sacolick LI & Hyder F (2006). Regional Temperature Changes in the Brain during Somatosensory Stimulation. *J Cereb Blood Flow Metab* **26,** 68–78.
Tryba AK & Ramirez J-M (2004). Hyperthermia modulates respiratory pacemaker bursting properties. *J Neurophysiol* **92,** 2844–2852.
Tye KM, Stuber GD, de Ridder B, Bonci A & Janak PH (2008). Rapid strengthening of thalamo-amygdala synapses mediates cue–reward learning. *Nature* **453,** 1253–1257.
van't Hoff MJH (1884). Etudes de dynamique chimique. *Recl des Trav Chim des Pays-Bas* **3,** 333–336.
De Vera L, González J & Rial R V. (1994). Reptilian waking EEG: slow waves, spindles and evoked potentials. *Electroencephalogr Clin Neurophysiol* **90,** 298–303.
Volgushev M, Vidyasagar TR, Chistiakova M & Eysel UT (2000). Synaptic transmission in the neocortex during reversible cooling. *Neuroscience* **98,** 9–22.
Wang H, Wang B, Normoyle KP, Jackson K, Spitler K, Sharrock M, Miller CM, Best C, Llano D & Du R (2014). Brain temperature and its fundamental properties: A review for clinical neuroscientists. *Front Neurosci* **8,** 1–17.
Wang XJ & Buzsáki G (1996). Gamma oscillation by synaptic inhibition in a hippocampal interneuronal network model. *J Neurosci* **16,** 6402–6413.
Wei P, Liu N, Zhang Z, Liu X, Tang Y, He X, Wu B, Zhou Z, Liu Y, Li J, Zhang Y, Zhou X, Xu L, Chen L, Bi G, Hu X, Xu F & Wang L (2015). Processing of visually evoked innate fear by a non-canonical thalamic pathway. *Nat Commun* **6,** 6756.
Weinberger NM (2011). The medial geniculate, not the amygdala, as the root of auditory fear conditioning. *Hear Res* **274,** 61–74.
Weisskopf MG & LeDoux JE (1999). Distinct Populations of NMDA Receptors at Subcortical and Cortical Inputs to Principal Cells of the Lateral Amygdala. *J Neurophysiol* **81,** 930–934.
Whitten T a, Martz LJ, Guico A, Gervais N & Dickson CT (2009). Heat synch: inter- and independence of body-temperature fluctuations and brain-state alternations in urethane-anesthetized rats. *J Neurophysiol* **102,** 1647–1656.
Winer JA (1984). The human medial geniculate body. *Hear Res* **15,** 225–247.
Wolff SBE, Gründemann J, Tovote P, Krabbe S, Jacobson GA, Müller C, Herry C, Ehrlich I, Friedrich RW, Letzkus JJ & Lüthi A (2014). Amygdala interneuron subtypes control fear learning through disinhibition. *Nature* **509,** 453–458.
Woodson W, Farb CR & LeDoux JE (2000). Afferents from the auditory thalamus synapse on inhibitory interneurons in the lateral nucleus of the amygdala. *Synapse* **38,** 124–137.
Yerkes RM & Dodson JD (1908). The relation of strength of stimulus to rapidity of habit-formation. *J Comp Neurol Psychol* **18,** 459–482.
Yu YQ, Xiong Y, Chan YS & He J (2004). In vivo intracellular responses of the medial geniculate neurones to acoustic stimuli in anaesthetized guinea pigs. *J Physiol* **560,** 191–205.
Zelikowsky M, Bissiere S & Fanselow MS (2012). Contextual Fear Memories Formed in the Absence of the Dorsal Hippocampus Decay Across Time. *J Neurosci* **32,** 3393–3397.
Zhou NA, Maire PS, Masterson SP & Bickford ME (2017). The mouse pulvinar nucleus: Organization of the tectorecipient zones. *Vis Neurosci* **34,** E011.
Zhu Y, Nachtrab G, Keyes PC, Allen WE, Luo L & Chen X (2018). Dynamic salience processing in paraventricular thalamus gates associative learning. *Science (80-)* **362,** 423–429.

DOI:10.15774/PPKE.ITK.2022.002

Tables

Table 1. Parameters of baseline brain temperature fluctuations under urethane anesthesia.

Number of animals	**3**
Total recording time	14.6 hours
Large (Type I.) fluctuations	
Number of fluctuations	19
Amplitude	0.22 +/- 0.014 °C
Length	155.2 +/- 12.8 s
Period length	963.1 +/- 119 s
Small (Type II.) fluctuations	
Number of fluct. epochs	22
Length of fluct. epochs	667.7 +/- 88.6 s
Number of fluct. cycles	309
Cycle amplitude	0.019 +/- 0.0008 °C
Cycle period length	44.8 +/- 1.1 s
Number of cycles in an epoch	14 +/- 2

DOI:10.15774/PPKE.ITK.2022.002

Table 2. Immunofluorescent staining protocols for fluorescent and electron microscopy. Steps were performed at room temperature where degree is not indicated.

Aim	Blocking	Primary antibodies	Amplification	Fluorescent secondary IgGs
GFAP staining for thermoprobe tracks	**1.** 1% H_2O_2 (Carl Roth) against endogenous peroxidase, ~10 min **2.** 2% normal horse serum (NHS, Vector Laboratories), ~30 min	**3.** mouse anti-GFAP (EMD Millipore clone GA5), 1:2000 overnight, 4ºC	**4.** biotinylated anti-mouse IgG, 1:250 (Vector Laboratories), 1.5 h **5.** avidin-biotin horseradish peroxidase complex (ABC HRP, Vector Laboratories), 1:250, 1.5 h **6.** DAB (Sigma-Aldrich) in Tris buffer (pH 7.6), ~20 min & H_2O_2, 10-15 min	-
eYFP amplification on transduced calretinin-positive (CR+) neurons **Figure 2.3.1.1./a** **Figure 2.3.1.5./c** **Figure 2.3.2.1./a**	**1.** 10% normal donkey serum (NDS, Abcam) in 0.1 M PB, 30 min	**2.** chicken or rabbit anti-GFP (ThermoFisher Scientific), 1:3000 or 1:5000	-	**5**. Alexa 488-conjugated donkey anti-rabbit or goat anti-chicken (DAR-A488 or GaCh, Jackson Immuno-Research),1:500, 2 h
eYFP amplification on transduced midbrain inputs in the LT, with CR-staining **Figure 2.3.3.1./ b-f, k-m, r-v**	**1.** 10% NDS and 0.5 % Triton-X (Sigma-Aldrich) in 0.1 M PB, 30 min	**2.** rabbit anti-GFP, 1:10000 & mouse anti-CR (Swant), 1:2000	**3.** biotinylated horse anti-mouse IgG (bHAM, Vector Laboratories), 1:300, 1.5 h **4.** eABC, 1:300, 1.5 h	**5.** DAR-A488, 1:500, & SA-Cy3 (Jackson ImmunoResearch) 1:2000 2 h
Immunogold-immunoperoxidase double staining for electron microscopic identification of eYFP-labelled midbrain synapses in the CR+LT **Figure 2.3.3.1./ l, n-p**	**1.** 3% bovine serum albumin (Sigma-Aldrich), 45 min **6.** 0.5% H_2O_2, 10 min **7.** 0.5% human serum albumin (Sigma-Aldrich) and 0.1% cold water fish skin gelatin (Aurion), 1h	**2.** rabbit anti-GFP & mouse anti-CR 1:3000	**3.** bHAM, 1:300, 2 h **4.** eABC HRP, 1:300, 1.5h **5.**Tyramide (Invitrogen),1:50, 15 min **8.** 0.8 nm gold conjugated SA (Aurion), 1:50 in **7.**, 4 ºC, overnight **9.** silver intensification with Aurion R-Gent SE-EM kit, 60 min **10.** postfixation in 2% glutaraldehyde, 15 min **11.** anti-rabbit ImmPRESS, (Vector Laboratories), 2 h **12.** 0.025% DAB, 20 min, & 0.5% H_2O_2, 10-15 min **13.** osmication with 0.5% OsO_4, 20 min, 4 °C & **14.** dehydration by 40 min treatment with 1% uranyl acetate diluted in 70% ethanol	-

DOI:10.15774/PPKE.ITK.2022.002

Table 3. Summary of statistical analyses.

Figure	Sample size	Statistical test	Results
2.3.1.2./a	n = 10 mice* PIL CR+LT Tone / FS / Tone+FS N = 61 / 60 / 62 cells CR+LT→AMY Tone / FS / Tone+FS N = 44 / 44 / 44 cells CR- Tone / FS / Tone+FS N = 278 / 252 / 278 cells SG CR+LT→AMY Tone / FS / Tone+FS N = 31 / 30 / 32 cells CR- Tone / FS / Tone+FS N = 53 / 50 / 54 cells *LT data in (Barsy & Kocsis et al., 2020) completed with 34 tagged and 86 non-tagged cells	*χ^2 test*	Comparison of cue-evoked responsivity (early / late / no activation) PIL CR+, Tone vs FS, χ^2=15.1045, p= 5.2494*10^{-4}; CR+, Tone vs. Tone+FS, χ^2 = 19.4633, p = 5.9375*10^{-5}; CR+LT→AMY, Tone vs FS, χ^2=23.0346, p= 9.9565*10^{-6}; CR+LT→AMY, Tone vs. Tone+FS, χ^2 = 25.0115, p = 3.7053*10$^{-6;}$ CR-, Tone vs. FS, χ^2 = 22.1619, p = 1.5403*10^{-5}; CR-, Tone vs. Tone+FS, χ^2 = 40.5342, p = 1.5780*10^{-9}; Tone, CR+ vs. CR-, χ^2 = 2.9160, p = 0.2327; Tone, CR+LT→AMY vs. CR-, χ^2 = 0.7673, p = 0.5297; FS, CR+ vs. CR-, χ^2 = 19.9887,p= 4.5658*10^{-5}; FS, CR+LT→AMY vs. CR-, χ^2 = 23.2286, p= 9.0358*10^{-6}; Tone+FS, CR+ vs. CR-, χ^2 = 19.1643, p = 6.8947*10^{-5}; Tone+FS, CR+LT→AMY vs. CR-, χ^2=19.7179, p = 1.7414*10^{-4}; SG CR+LT→AMY, Tone vs. FS, χ^2 = 10.3214, p= 0.0057; CR+LT→AMY, Tone vs. Tone+FS, χ^2=5.5725, p = 0.0617; CR-, Tone vs FS, χ^2 = 23.1205,p = 9.5376*10^{-6}; CR-, Tone vs. Tone+FS, χ^2 = 10.5882, p = 0.0050; Tone, CR+LT→AMY vs CR-, χ^2 = 3.5742, p = 0.1674; FS, CR+LT→AMY vs CR-, χ^2 = 0.6966, p = 0.7059; Tone+FS, CR+LT→AMY vs CR-, χ^2 = 3.4544, p = 0.1778;
2.3.1.2./b	PIL CR+LT CR+LT→AMY CR- SG CR+LT→AMY CR-		Median latency of all sensory evoked responses in 5 ms bins (Tone / FS / Tone+FS) 25 / 15 / 20 ms 23 / 20 / 20 ms 25 / 15 / 20 ms 35 / 70 / 113 ms 20 / 83 / 35 ms
2.3.1.2./d	PIL CR+, N = 27 cells	*Friedman's ANOVA with Wilcoxon signed-rank test, two-sided*	$X^2_{25, 2}$ = 13.76, p = 0.00103; Tone vs. FS, Z = -2.5429, p = 0.011; Tone vs. Tone+FS, Z = -3.4857, p = 0.00049; FS vs. Tone+FS, Z = -2.2286; p = 0.0258;

2.3.1.3./c	n = 6 mice <u>PIL</u> CR+LT Tone / FS / Tone+FS N = 49 / 51 / 52 cells CR- Tone / FS / Tone+FS N =167 / 177 / 175 cells <u>SG</u> CR+LT Tone / FS / Tone+FS N = 18 / 18 / 18 cells CR- Tone / FS / Tone+FS N = 49 / 45 / 45 cells	*χ2 test*	<u>Comparison of onset responsivity (early / late / no activation)</u> <u>PIL</u> CR+, Tone vs FS, χ^2=24.1436, p= 5.7186*10^{-6}; CR+, Tone vs. Tone+FS, χ^2 = 20.3379, p = 3.8342*10^{-5}; CR-, Tone vs. FS, χ^2 = 15.3749, p = 4.5855*10^{-4}; CR-, Tone vs. Tone+FS, χ^2 = 30.8005, p = 2.0500*10^{-7}; Tone, CR+ vs. CR-, χ^2 = 1.1574, p = 0.5606; FS, CR+ vs. CR-, χ^2 = 17.9566, p=1.2612*10^{-4}; Tone+FS, CR+ vs. CR-, χ^2 = 9.3712, p = 0.0092; <u>SG</u> CR+, Tone vs. FS, χ^2 = 8.6897, p=0.0130; CR+, Tone vs. Tone+FS, χ^2 = 10.2857, p = 0.0013; CR-, Tone vs FS, χ^2 = 8.4172, p = 0.0149; CR-, Tone vs. Tone+FS, χ^2 = 8.0175, p = 0.0182; Tone, CR+ vs CR-, χ^2 = 3.8191, p = 0.1481; FS, CR+ vs CR-, χ^2 = 0.6509, p = 0.7222; Tone+FS, CR+ vs CR-, χ^2 = 1.9493, p =0.3773; <u>Comparison of offset responsivity (early / late / no activation)</u> <u>PIL</u> FS, CR+ vs. CR-, χ^2 = 12.7650, p = 0.0017; Tone+FS, CR+ vs. CR-, χ^2 = 9.2749, p = 0.0097; <u>SG</u> FS, CR+ vs CR-, χ^2 = 0.2800, p = 0.8694; Tone+FS, CR+ vs CR-, χ^2 = 0.7292, p = 0.6945;
2.3.1.3./d	<u>PIL</u> CR+LT CR- <u>SG</u> CR+LT CR- <u>PIL</u> CR+LT CR- <u>SG</u> CR+LT CR-		<u>Median latency of all sensory evoked onset responses in 5 ms bins (Tone / FS / Tone+FS)</u> 20 / 15 / 10 ms 25 / 35 / 33 ms n/a / 175 / 75 ms 225 / 55 / 105 ms <u>Median latency of all sensory evoked offset responses in 5 ms bins (FS / Tone+FS)</u> 17.5 / 12.5 ms 25 / 25 ms 15 / 17.5 ms 20 / 30 ms

2.3.1.3./f	PIL CR+, onset N = 17 cells PIL CR+, offset N = 15 cells	*Friedman's ANOVA with Wilcoxon signed-rank test, two-sided*	$X^2 = 21.29$, $p = 2.37 \times 10^{-5}$; Tone vs FS, Z = -3.4320, $p = 5.99 \times 10^{-4}$; Tone vs. Tone+FS, Z =-3.6214, $p=2.93 \times 10^{-4}$; FS vs. Tone+FS, Z = -1.8938, $p = 0.0583$; FS vs. Tone+FS, $p = 0.2078$;
2.3.1.4./c	n = 4 mice CR+LT-recipient (rec.) Tone / FS / Tone+FS N = 21 / 21 / 19 cells non-recipient (non-rec.) Tone / FS / Tone+FS N = 45 / 43 / 42 cells	*χ2 test*	<u>Comparison of cue-evoked onset responsivity (early / late / no activation)</u> rec., Tone vs. FS, $\chi^2 = 5.6757$, $p = 0.0172$; rec, Tone vs. Tone+FS, $\chi^2 = 4.9123$, $p = 0.0858$; non-rec., Tone vs FS, $\chi^2 = 1.1503$, $p = 0.5626$; non-rec., Tone vs. Tone+FS , $\chi^2 = 1.2066$, $p = 0.5470$; Tone, rec. vs. non-rec., $\chi^2 = 0.9625$, $p= 0.6180$; FS, rec. vs. non-rec., $\chi^2 = 4.0321$, $p = 0.1332$; Tone + FS, rec. vs. non-rec., $\chi^2 = 1.5259$, $p = 0.4663$; <u>Comparison of cue-evoked offset responsivity (early / late / no activation)</u> FS, rec. vs. non-rec., $\chi^2 = 11.1057$, $p = 0.0039$; Tone+FS, rec. vs. non-rec., $\chi^2 = 6.0610$, $p = 0.0138$;
2.3.1.5./b	n = 10 mice	*Friedman's ANOVA with Wilcoxon signed-rank test*	Cond freezing, $\chi^2_{10,2} = 17.6842$, $p = 0.0001$; Pre vs. CS+, Z = -1.8204, $p = 0.0687$; CS+ vs. CS+US, Z = -2.8031, $p = 0.0051$; Cued Retr freezing, $X^2_{10,2} = 13.4$, $p = 0.0012$; Pre vs. CS+, Z = -2.0896, $p = 0.0367$; CS- vs. CS+, Z = -2.8031, $p = 0.0051$;
2.3.1.7./b	n = 5 mice 3 s 10 s 30 s	*One-way repeated measures ANOVA with post hoc Fisher's LSD*	Cue-evoked freezing, $p = 0.0132$; Retr1 vs. Retr4, $p = 0.0295$; Retr1 vs. Retr4, $p = 0.0094$; Retr1 vs. Retr4, $p = 0.0106$;
2.3.1.8./c	N = 16 CR+LT cells 3 s 10 s 30 s	*Wilcoxon signed-rank test (two-sided)*	Cond, Z = - -0.4829, $p = 0.6292$; Retr1, Z = -2.0949, $p = 0.0362$; Retr3, Z = 1.0358, $p = 0.3003$; Cond, Z = 0.2272, $p = 0.8202$; Retr1, Z = -1.0349, $p = 0.3007$; Retr3, Z = -2.5589, $p = 0.0105$; Cond, Z = 3.3611, $p = 7.7641 \times 10^{-4}$; Retr1, Z = -1.2412, $p = 0.2145$; Retr3, Z = -0.0628, $p = 0.9499$;

2.3.1.8./g	N = 16 CR+LT-recipient cells 3 s 10 s 30 s	*Wilcoxon signed-rank test (two-sided)*	Cond, Z = 1.9318, p = 0.0534; Retr1, Z = -1.1077, p = 0.2680; Retr3, Z = 0.1571, p = 0.8752; Cond, Z = 2.9191, p = 0.0035; Retr1, Z = -1.3818, p = 0.1670; Retr3, Z = -0.1138, p = 0.9094; Cond, Z = 1.9311, p = 0.0535; Retr1, Z = -0.3977, p = 0.6909; Retr3, Z = 0.5964, p = 0.5509;
2.3.2.1./c	n = 8 mice <u>PN</u> Tone / FS / Tone+FS 137 / 82 / 95 cells <u>IN</u> Tone / FS / Tone+FS 46 / 47 / 43 cells *AMY data completed with 4 AStr narrow-spiking cells not shown in (Barsy & Kocsis et al., 2020)	$\chi 2$ test	<u>Comparison of cue-evoked responsivity (early / late / no activation)</u> PN, Tone vs FS, χ^2 = 10.2448, p = 0.0060; PN, Tone vs. Tone+FS, χ^2 = 8.9396,p =0.0114; IN, Tone vs FS, χ^2 = 9.4844, p = 6.2574**10^{-4}; IN, Tone vs. Tone+FS , χ^2 = 8.5705, p =0.0138; Tone, PN vs. IN, χ^2 = 13.5340, p = 0.0012 FS, PN vs. IN, χ^2 = 20.6540, p = 3.2737*10^{-5}; Tone+FS, PN vs. IN, χ^2 = 15.7569, p = 3.7882*10^{-4}; <u>Comparison of effects of CR+LT axonal inhibition</u> (early exc. / suppression / none; long exc. / supp. / none; disinhibition / none) Tone, PN vs. IN, χ^2 = 17.6730, p = 0.0071; FS, PN vs. IN, χ^2 = 23.1943, p = 0.0016; Tone+FS, PN vs. IN, χ^2 = 28.9982, p = 1.4480*10^{-4};
2.3.2.1./d	<u>PN</u> Tone / Tone+inh. N = 6 / 2 cells FS / FS+inh. N = 13 / 19 cells Tone+FS/ Tone+FS+inh. N = 15 / 14 cells <u>IN</u> Tone / Tone+inh. N = 10 / 8 cells FS / FS+inh. N = 26 / 21 cells Tone+FS/Tone+FS+inh. N = 19 / 17 cells	*Wilcoxon rank-sum test, two-sided*	<u>Median latency of all sensory evoked onset responses in 5 ms bins (Tone / FS / Tone+FS)</u> 33 / 33 ms 20 / 30 ms 33 / 45 ms 50 / 48 ms 18 / 15 ms 18 / 25 ms Tone vs.Tone+inh., Z =-0.4286, p = 0.6682; FS vs. FS+inh., Z = -1.6068, p = 0.1081; Tone+FS vs. Tone+FS+inh., Z = 0.5644; p = 0.5725;

2.3.3.2./b	SC>>LT: AMY N = 55 cells >> LT: AMY N = 26 cells >> LT: LT N = 70 cells >>AMY: AMY N = 33 cells >>AMY: LT N = 18 cells SC>>LT: AMY FS, N = 23 cells >>AMY: AMY FS, N = 11 cells	*Wilcoxon rank-sum test, two-sided*	<u>Median latency of all optogenetically evoked onset responses in 1 ms bins</u> 9.5 ms 6.5 ms 4 ms 6 ms 7 ms SC>>LT: AMY vs. >>LT: AMY, Z = 3.0717, p = 0.0021; SC>>LT: AMY vs. >> LT: LT, Z = 6.7994, p = 1.0505 x10^{-11}; SC>>LT: AMY vs. >>AMY: AMY, Z = 3.6271, p = 2.8667x10^{-4}; SC>>LT: AMY vs. >>AMY: LT, Z = 2.5614, p = 0.0104; >>AMY: LT vs. >>AMY: AMY, Z = 0.9283, p = 0.3532; >>LT: AMY vs. >>AMY: AMY, Z = 0.2532, p = 0.8001; >>LT: LT vs. >>AMY: AMY, Z = -3.3044, p = 9.5173x10^{-4}; >>LT: AMY vs. >>AMY: LT, Z = -0.4876, p = 0.6258; >>LT: AMY vs. >>LT: LT, Z = 3.1607, p = 0.0016; >>LT: LT vs. >>AMY: LT, Z = -3.9229, p = 8.7484x10^{-5}; <u>Median latency of early shock-evoked onset responses in 5 ms bins</u> FS, SC>>LT: AMY vs. >>LT: AMY, Z = 1.3801, p = 0.1676;
2.3.3.3./a	n = 4 mice <u>AMY</u> <u>PN</u> CR+LT-recipient (rec.), N=12 cells non-recipient, N=55 cells	*χ^2 test*	<u>Comparison of cue-evoked onset responsivity (early / late / no activation)</u> rec. vs. non-rec., FS, χ^2 =11.3844, p =0.0034; rec. vs. Ctx, FS, χ^2 = 18.4127, p = 1.0040*10^{-4}; non-rec. vs. Ctx, FS, χ^2 = 3.2436, p = 0.1975; PN vs. IN, χ^2 = 17.5555, p = 1.5412x10^{-4};

	IN
	CR+LT-recipient,
	N = 17 cells
	
	non-recipient,
	N = 25 cells
	
	Ctx
	PN, N = 42 cells
	IN, N = 10 cells
			Comparison of cue-evoked offset responsivity (early / late / no activation)
			
			rec vs. non-rec., FS, χ^2 = 2.1171, p = 0.3470;
			rec. vs. Ctx, FS, χ^2 = 6.0767, p = 0.0479;
			non-rec. vs. Ctx, FS, χ^2 = 2.3753, p = 0.3049;
			PN vs. IN, χ^2 = 5.6375, p = 0.0597;
			
			Comparison of PN: IN ratios
			
			rec. vs. non-rec., χ^2 = 6.7323, p = 0.0095;
			rec. vs. Ctx., χ^2 = 12.9987, p = 3.1171x10^{-4};
			non-rec. vs. Ctx., χ^2 = 2.3366, p = 0.1264;

2.3.3.3./b	n = 3 mice
	
	PN
	SC-activated (act.)
	N = 28 cells
	
	not SC-activated (non-act.)
	N = 27 cells
	
	IN
	SC-activated
	N = 26 cells
	
	not SC-activated
	N = 9 cells
	
	Ctx
	PN, N = 66 cells
	IN, N = 7 cells
		χ2 test	Comparison of cue-evoked onset responsivity (early / late / no activation)
			
			act. vs. non-act., FS, χ^2 = 13.0941, p = 0.0014;
			act. vs. Ctx, FS, χ^2 =23.1040, p =9.6169*10^{-6};
			non-act. vs. Ctx, FS, χ^2 = 1.3572, p = 0.5073;
			PN vs. IN, χ^2 = 14.1730, p = 8.3630x10^{-4};
			
			Comparison of cue-evoked offset responsivity (early / late / no activation)
			
			act. vs. non-act., FS, χ^2 = 1.5169, p = 0.4684;
			act. vs. Ctx, FS, χ^2 = 3.9420, p = 0.1393;
			non-act. vs. Ctx, FS, χ^2 = 0.7958, p = 0.6717;
			PN vs. IN, χ^2 = 17.1745, p = 1.8647x10^{-4};
			
			Comparison of PN: IN ratios
			
			rec. vs. non-rec., χ^2 = 4.8701, p = 0.0273;
			rec. vs. Ctx., χ^2 = 23.9956, p = 9.6554x10^{-7};
			non-rec. vs. Ctx., χ^2 = 4.5720, p = 0.0325;